Analysis of the Optical Coupling of Wavelength-Shifting Fibers to Organic Liquid Scintillator Filled Fluoropolymer Tubes for Industrial and Nuclear Security Applications

by

CHAD C. SCHOOLS

B.S. Physics, Worcester Polytechnic Institute, 1994
M.S. Engineering Management, University of Missouri-Rolla, 1999
M.S. Nuclear Engineering, Air Force Institute of Technology, 2005

SUBMITTED TO THE DEPARTMENT OF NUCLEAR SCIENCE AND ENGINEERING
IN PARTIAL FULFILLMENT OF THE REQUIREMENTS FOR THE DEGREE OF

DOCTOR OF PHILOSOPHY IN NUCLEAR SCIENCE AND ENGINEERING
AT THE
MASSACHUSETTS INSTITUTE OF TECHNOLOGY

JUNE 2014

Signature of Author: Signature redacted
Department of Nuclear Science and Engineering, May 2014

Certified By: Signature redacted
Richard Lanza
Senior Research Scientist
Thesis Supervisor

Certified By: Signature redacted
R. Scott Kemp
Assistant Professor of Nuclear Science and Engineering
Thesis Reader

Certified By: Signature redacted
Gordon Kohse
Principal Research Engineer
Thesis Reader

Certified By: Signature redacted
Tancredi Botto
Principal Research Scientist, Schlumberger-Doll Research
Thesis Reader

Accepted By: Signature redacted
Mujid S. Kazimi
TEPCO Professor of Nuclear Engineering
Chairman, Department Committee on Graduate Students

-Blank Page-

Analysis of the Optical Coupling of Wavelength-Shifting Fibers to Organic Liquid Scintillator Filled Fluoropolymer Tubes for Industrial and Nuclear Security Applications

by

CHAD C. SCHOOLS

Submitted to the Department of Nuclear Science and Engineering
On May 16, 2014
in Partial Fulfillment of the Requirements for
the Degree of Doctor of Philosophy in Nuclear Science and Engineering

Abstract

Industrial and nuclear security applications continue to push radiation detection development into new and exciting frontiers. In this work, an innovative detection module is developed and tested for use in a cosmic ray imaging (CRI) system designed for oil field characterization and is evaluated for its potential use in a fast neutron detection system for nuclear security applications. By measuring density changes in the reservoir, the CRI system will provide real-time information about steam chamber development during the enhanced oil field recovery process known as steam assisted gravity drainage (SAGD). The ability to monitor the development of the steam chamber region has the potential to provide important information, which could be used to optimize the growth and uniformity of the underground steam chamber and minimize costs. The organic liquid scintillator based detection modules also detect fast neutrons. During the initial characterization of an unidentified radioactive source, it is important to have the capability to determine if special nuclear material (SNM) is present and if it is configured to produce a nuclear yield. The emission of multiple neutrons during a single fission makes it possible to use this unique timing characteristic to identify SNM. The number of specialists trained to handle nuclear devices is limited making this determination a critical step in properly responding to the situation.

The detector module consists of a 5 mm diameter by 2-meter long fluoropolymer tube filled with organic liquid scintillator (OLS), optically read-out using wavelength shifting (WLS) fibers. The 1:400 ratio of diameter to length makes light collection from the organic scintillator very challenging. Over ten configurations of OLS, fluoropolymer tubes, and WLS fibers were tested. The final configuration consisted of two 2mm BCF-91A WLS fibers optically coupled to the outside of an optically transparent fluorinated ethylene propylene (FEP) tube filled with a commercial OLS (EJ-309). Cosmic ray muons produce large light pulses in the OLS of which a portion reaches the external WLS fibers. The WLS fibers re-emits the light at longer wavelengths and acts as a multi-mode light guide channeling the signal to photomultiplier tubes located at each end of the WLS fibers. This module demonstrated excellent detection efficiency with less than 5% signal reduction, at any point along the module, due to optical attenuation. Timing analysis of the WLS fiber signals also provided coarse position determination, ±40 cm, which opens design options not previously available.

An important characteristic required of neutron detectors for nuclear security applications is the ability to discriminate fast neutron and gamma ray events. Initial tests have demonstrated the capability of our module to discriminate neutron and gamma rays by applying the rise time pulse shape discrimination (PSD) method to the WLS fiber signals. EJ-309 is

well known for its PSD capabilities. Coupling this desirable characteristic with loss free, low attenuation optical read-out through a WLS fiber has the potential to broaden significantly liquid scintillator applications.

Thesis Supervisor: Richard Lanza
Title: Senior Research Scientist

Acknowledgments

I would like to thank my thesis committee members, Dr. Richard Lanza, Dr. R. Scott Kemp, Dr. Gordon Kohse, and Dr. Tancredi Botto for all of their guidance and mentorship. I am very thankful to the Schlumberger nuclear research team, Brad Roscoe, Tancredi Botto, Angel Manzur and Jim Haug. Their unlimited support made this possible. I would also like to thank my truly amazing family, Kerri, Jacob, Luke, Jared, and Isaac for their love, support, and sacrifice.

This work was supported by the Schlumberger-Doll Research Center.

Table of Contents

-Blank Page-

List of Figures

List of Tables

1. Introduction

A wide range of industrial and government applications continue to push radiation detection development into new and exciting frontiers. Advanced detection systems require innovative solutions to meet technical specifications such as efficiency, angular resolution, energy resolution, and timing resolution while performing under demanding operational constraints such as a wide range of temperatures, varying background radiation, mechanical shock, dimensions, and weight. Technology advancements in the areas of signal processing, optical light read-out, detection materials, equipment miniaturization, and computer model simulations enable these concepts to become a reality.[1,2] In this work, an innovative detection module is developed and tested for use in a cosmic ray imaging system designed for oil field characterization and is evaluated for its potential use in a fast neutron detection system for nuclear security applications.

1.1. Motivation

1.1.1. Cosmic Ray Imaging for SAGD

Canada's heavy-oil reserve, one of the largest in the world, has an estimated 175 billion barrels of which 80% are too deep for open pit mining.[3] Research on in-situ methods using steam to extract the heavy oil from the sand began in the 1970s but it wasn't until 2002 that the first production from a commercial steam assisted gravity drainage (SAGD) project was realized.[4] Now (2014), over 50% of the oil Canada produces is from in-situ methods like SAGD, with continued growth expected. The SAGD method uses two horizontal wells separated by approximately 5 meters. Steam, pumped at high pressures into the top well (aka the injector well), penetrates the reservoir. In doing so, it heats up the local bitumen until its viscosity is low enough to allow it to flow by gravity into the lower well (aka the producer

well). The mobilized oil or bitumen is then pumped from the production well to the surface for processing. Natural gas consumption for steam production accounts for 60% to 70% of the total operation costs for SAGD plants, making steam management an important aspect of SAGD operations.[3] The ability to monitor the development of the steam chamber region has the potential to provide important information to the operator, which could be used to optimize the growth and uniformity of the underground steam chamber and minimize costs.

As part of this thesis, a cosmic ray imaging (CRI) system has been developed at Schlumberger-Doll-Research (SDR) Center with the goal of providing in-situ and near-real-time information about steam chamber development in a SAGD field.

Cosmic ray muons continually penetrate the earth's surface and their flux is attenuated as they travel underground. As a SAGD steam chamber develops, the bitumen is replaced with steam, decreasing the density in the reservoir. Muons passing through this lower density region are attenuated less, resulting in an increased muon flux in that direction. The density across the field can be monitored in real time by measuring the muon intensity and direction.

This technique of muon imaging has been used in several other applications including studies of the interior of volcanos.[5, 6] SDR has developed a prototype device that was tested with Suncor Energy Inc. in a SAGD observation well at MacKay River, in the Ft. McMurray region of northern Alberta, Canada.[7] The intent of the field test was to demonstrate the deployment capability, verify the stability of the system in an operational environment, and establish constant remote data monitoring. Based on the data collected and Monte-Carlo modelling, improved muon detection rates, i.e., increased area, is required to identify density changes more rapidly and accurately.

The operational constraints of downhole monitoring and the required geometries for a CRI borehole detector limits the available options to improve the muon detection rate or the angular resolution of the density mapping. The CRI design requires many long-thin detection

modules as shown in Figure 1.1. The crossed helical pattern allows the position along the axis of the tool to be determined by observing coincident events in adjacent rings. Adjacent ring fibers cross only once in the length of the tool. When a coincident event occurs, the interaction position is localized at the crossing point of the two coincident fibers as shown in Figure 1.2. The blue parallelogram defines the uncertainty in the position determination and depends on the active length of the tool, L, the diameter of the fiber rings, D, and the diameter of the individual fibers, d. When there is at least two pairs of coincident fibers the muon trajectory is reconstructed using their crossing points. The angular resolution of the density mapping worsens with position uncertainty. There is a tradeoff between an increase in the muon detection rate, that is proportional to the active area D x L, and the degradation in angular resolution as L is increased. It is important to recognize that a valid muon event can be easily discriminated from background gamma ray and neutron events since we require a hit in at least four fibers.

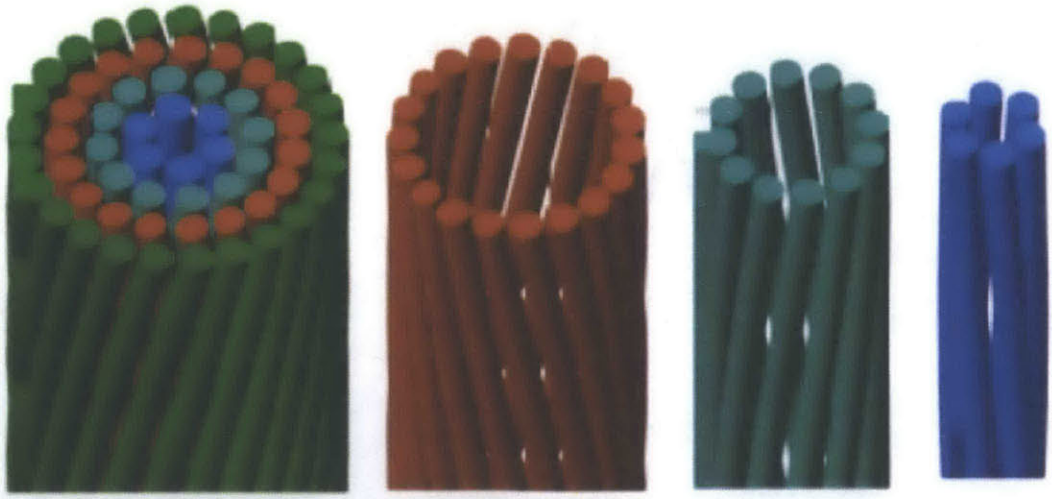

Figure 1.1. Crossed-helical design of SDR cosmic ray imaging (CRI) system. No fibers cross more than once in the 1-meter length of the system. Coincident muon hits in adjacent rings determine the muon path. Reproduced with the permission of Schlumberger.

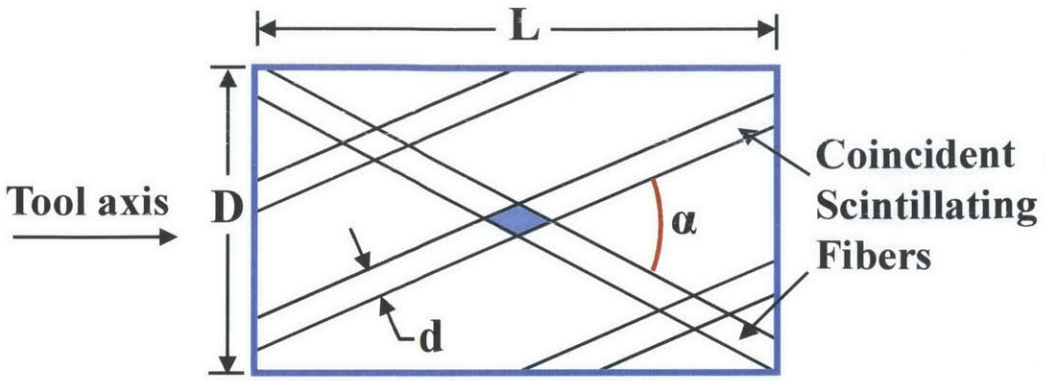

Figure 1.2. The muon interaction position is localized at the crossing point of adjacent fibers that experience a coincident event. The blue parallelogram determines the uncertainty in the position determination. The active length of the tool is L, the diameter of a ring of fibers is D, the individual fiber diameter is d, and the angle between fibers in adjacent rings is α. Reproduced with the permission of Schlumberger.

The initial CRI design used a fluoropolymer tubing, PTFE (polytetrafluoroethylene), filled with organic liquid scintillator (OLS) with the concept that the design would provide a large optical signal with flexible dimensions. However, the OLS filled PTFE tubes demonstrated a very poor attenuation length making them impossible to use. With the pressing need for an operational prototype, a system with an outer diameter of 3.5 inches was constructed using 5-millimeter diameter by 1-meter long plastic scintillating fibers. This system was suitable for initial testing but future designs require the muon count rate to be maximized to reduce statistical uncertainties of the density mapping. Although plastic scintillators provide a large signal and good attenuation, they do not readily provide the flexibility to increase the length of the system since as the length of the plastic fiber increase, they are more susceptible to damage and the cost of manufacturing increases. In turn, the use of multiple one-meter systems requires each system to have its own light collection and electronics, which is cost prohibitive. Therefore, a practical system for SDR required an efficient muon detection module that provided a measurable signal at lengths of 2-meters or greater.

1.1.2. Fast Neutron Detection for Nuclear Security

While developing the detection module for the cosmic ray imager, its potential as a fast neutron detector for nuclear security also became apparent. With so many diverse commercial applications using radioactive sources and a complex and varying background radiation, it is difficult to distinguish between benign sources of radiation and a nuclear device that could produce an explosive yield of 10 kilotons (kt) or greater. The number of specialist trained to handle nuclear devices is limited, making the characterization of a neutron source as special nuclear material (SNM) as early as possible a critical step in properly responding to the incident. As one would expect, this is not a trivial matter considering the vast configurations of nuclear weapons and radioactive materials.

In general, the primary fissile isotopes of concern are uranium-235 (^{235}U) and plutonium-239 (^{239}Pu). In practical scenarios, the neutron signature from a ^{235}U-based weapon is undetectable.[8] Therefore, we focus on the detection of neutrons from ^{239}Pu-based weapon. Weapons grade plutonium (WgPu) is produced by irradiating uranium-238 (^{238}U) in a nuclear reactor and consists primarily of ^{239}Pu. WgPu will also have small amounts of other isotopes including plutonium-240 (^{240}Pu). Given the typical amount of ^{240}Pu present and its relatively high spontaneous fission rate, this is the primary source of neutrons from WgPu. Although the fission neutrons will have a unique energy spectrum, this will be difficult to measure since portable neutron spectrometers are difficult to make.

Current systems primarily rely on multiplicity counting, a technique that relies on the unique coincidence signature that arises from multiple neutrons being produced in each spontaneous or induced fission. These systems, notably the NPOD[9, 10] developed at Los Alamos National Laboratory (LANL) and the Fission Meter[11] developed by Livermore National Laboratory (LLNL) and commercialized by ORTEC, use large quantities of helium-

3 (^{3}He) detectors and rely on moderation to thermalize the fast fission neutrons before capturing them. The time required to moderate the neutrons significantly degrades the coincidence timing capabilities requiring longer collection times. In addition, the existing ^{3}He shortage makes wide deployment of the NPOD or Fission Meter impossible. Developing a fast neutron detector, such as the one shown in Figure 1.3, that is low cost non-^{3}He based and that can deploy with local first responders, has the potential to provide new rapid characterization capabilities that will guide the intelligent deployment of our limited personnel trained to respond to and render-safe nuclear weapons.

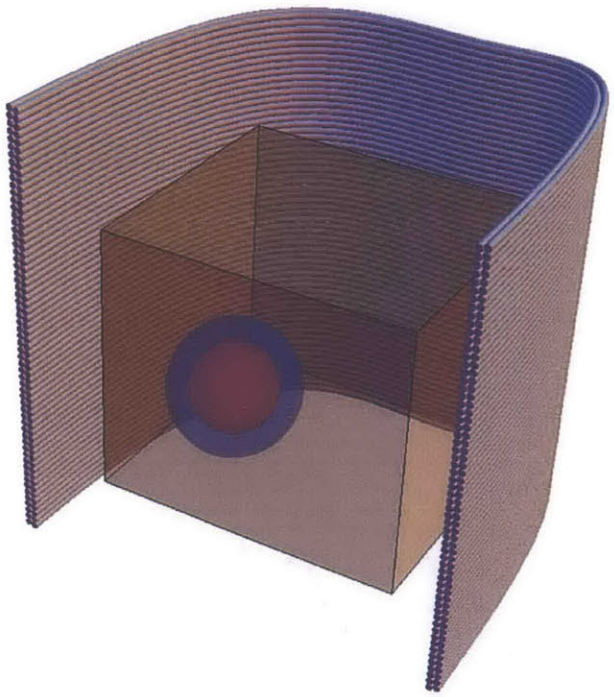

Figure 1.3. When an unknown neutron source has been identified, it is necessary to determine rapidly if special nuclear material is present and if it is in a configuration to produce a nuclear yield. A flexible OLS based detection system could provide a low cost alternative to expensive systems based on scarce ^{3}He.

1.2. Problem Statement

The primary goals of this work are to develop an alternative detection module for cosmic ray imaging with the following characteristics:

- Operate at a continuous length of at least two meters with comparable muon detection efficiency to conventional plastic fibers,
- Have enough flexibility to conform to the helical CRI geometry,
- Have the potential to survive multi-year deployment without maintenance, and
- The ability to provide interaction position along module would be an additional (but not required) benefit.

Additional requirements for fast neutron detection are secondary to the CRI requirements. This portion of my research will evaluate the CRI detection module for use in a fast neutron detector with the following criteria:

- Maximize fast neutron detection efficiency to minimize data collection times,
- Have the potential to discriminate between neutron and gamma ray events, and
- Have a scalable form factor able to conform to operational scenarios.

1.3. Importance of this Work

Scintillation light collection in long-thin geometries has always been a challenge. In the development of a detection module for cosmic ray imaging, a simple, cost effective, and scalable solution was built and tested. This not only provides the building blocks for a scalable cosmic ray imager, it also opens a wide range of detection designs that may not have been considered without this capability. The potential to discriminate neutron and gamma ray events based on the WLS fiber read-out further expands its possibilities. Current nuclear security

multiplicity counters rely on large quantities of scarce ^{3}He. The ability to detect fast neutrons and discriminate gamma ray background makes these organic liquid scintillator filled fluoropolymer tubes a viable alternative to the current ^{3}He systems.

1.4. Organization of this Thesis

This thesis is organized into seven chapters. The first chapter discusses the motivation to seek a detection module that meets requirements for a cosmic ray imaging system and a fast neutron detector. The second chapter provides the technical background of detecting muons, neutrons, and gamma rays with an organic liquid scintillator. An estimate of the scintillation light from each source is also calculated. In Chapter 3, a model of light propagation in fluoropolymer tubes and of light collection in wavelength shifting fibers is used to estimate expected signals. Chapter 4 outlines the construction and initial testing of the detection modules. Chapter 5 analyzes the detection modules performance detecting muons for the CRI application. Chapter 6 analyzes the detection modules performance detecting neutrons for the fast neutron detector application. Finally, the conclusions from this work and recommendations for future research are provided in Chapter 7.

2. Radiation Detection Using Organic Liquid Scintillators

The advantages of organic liquid scintillators (OLS) over other options, such as plastics or high-pressure gases, are many. First, viable OLS options produce more scintillation light (characteristic visible and ultraviolet light) than the plastic fibers while having a faster decay time resulting in more accurate timing measurements. Second, the liquid scintillator can also be held in almost any size or shape container that allows the scintillation light to be collected directly or through a wavelength shifter. Next, the bulk costs of OLS makes it the most inexpensive option available. Finally, OLS have the added benefit of being an efficient fast neutron detector and some OLS have neutron-gamma ray discrimination capabilities.

There are, of course, some disadvantages of using liquid scintillators that need to be considered and compensated for. First, creating a leak-proof system can present some challenges and some liquid scintillators have flashpoints as low as 26°C/79°F. For long-term applications, airtight systems are required to prevent dissolved oxygen from degrading the light output over time. Some liquid scintillators are also toxic, which may limit their application where the potential for human contact is more likely. With the wide range of commercially available OLS and the many systems currently employing them, these disadvantages can be mitigated.

Generally, OLS are benzene-based compounds with valence electrons occupying σ- and π-molecular orbitals. The σ-orbitals are strongly centered with the molecule but the π-orbitals can be delocalized. When the π-electron spins are fully paired the molecule is in a singlet state and when they are unpaired it is in a triplet state. Energy deposited by incident radiation results in electrons jumping to higher energy singlet and triplet states through different processes that will be described later. Transitions between these π-electronic states produce the scintillation light that is converted through a photomultiplier to the electrical

signals measured.[12] There are two principle types of liquid scintillators, binary and ternary systems. In both systems, there is a solvent, such as toluene or p-xylene, which is the primary constituent of the system and where the incident radiation deposits its energy. In a binary system, the solvent dissolves a small concentration of solute, such as p-terphenyl. This primary solute produces the fluorescence after the deposited energy is transferred from the solvent. In a ternary system, a secondary solute, such as POPOP (1,4-Bis-(2-(5-phenyloxazoly))-benzene), acts as a wavelength shifter absorbing the primary solute's fluorescence and re-emitting at longer wavelengths.[12]

In this chapter, we review the scintillation light from the interactions of muons, neutrons, and gamma rays inside an OLS. First, we describe the population of various singlet and triplet π-electronic states of a ternary system and the associated radiative and non-radiative processes. Next, the effect of excitation density, i.e., the spatial distribution of excitation and ionization, on the population of excited singlet and triplet states and their subsequent de-excitation is discussed. Then, we present descriptions of the muon, neutron, and gamma ray sources of importance to this work and finally the expected scintillation light from each.

2.1. The Scintillation Process in Organic Liquid Scintillators

As described earlier, a ternary system consists primarily of solvent molecules [X], with small quantities of primary solute molecules [Y], and secondary solute molecules [Z]. The scintillation process starts with a charged particle exciting and ionizing X. Figure 2.1 shows a general energy level diagram for X, Y, and Z and the main transitions that can occur. Transitions from higher states to lower states are radiative if they emit light, shown as solid blue arrows, or non-radiative if they do not emit light, shown as dashed red arrows. Excitations, shown as solid green arrows, result in the population of excited singlet states of S_{1X}, S_{2X}, and S_{3X}. The fine structure of the levels are due to molecular vibrations. The time scale of these

molecular vibrations is on the order of picoseconds resulting in the rapid non-radiative transitions from higher energy states, called internal degradation, to S_{1X}. The X and Y combination is chosen to maximize non-radiative transitions from S_{1X} to excited states of Y, shown with a horizontal red arrow. Similarly, the internal degradation to S_{1Y} from higher states happens rapidly. Unlike the X and Y combination, the Y and Z combination is chosen to maximize radiative transitions from S_{1Y} to the excited states of Z, shown with a solid blue arrow connecting S_{0Y} and S_{0Z}. After the rapid internal degradation from higher states to S_{1Z}, the secondary solute produces prompt fluorescence, which is the largest contribution to the total scintillation light. The fluorescence is at longer wavelengths reducing re-absorption in X or Y. These radiative transitions also decay to higher energy vibrational states S_{0nZ} emitting longer wavelength photons and further reducing the potential for self-absorption in Z. Figure 2.2 shows the absorption and emission spectra of the common secondary solute bis-MSB.

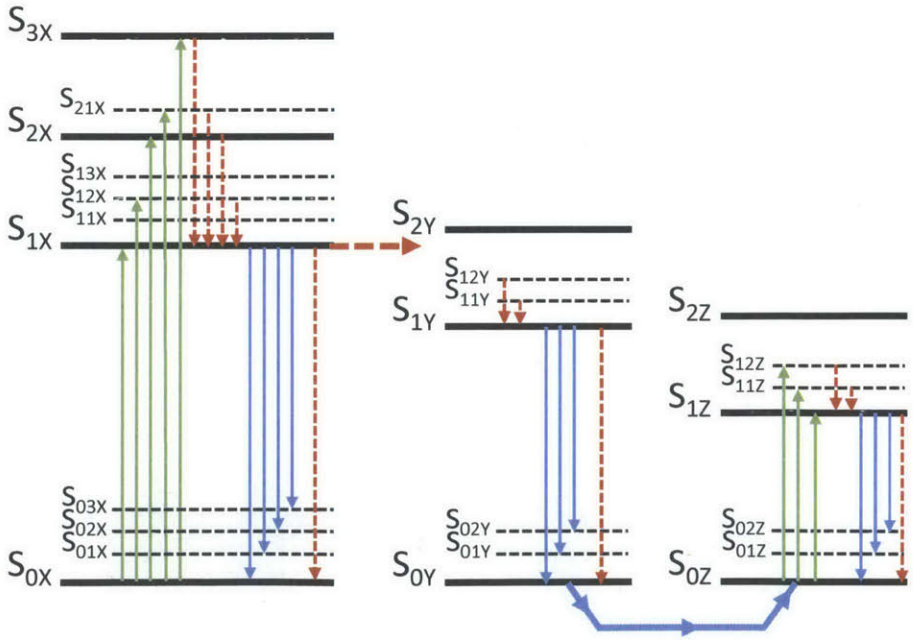

Figure 2.1. Energy diagram for an organic liquid scintillator. A ternary system consists primarily of solvent molecules [X], with small quantities of primary solute molecules [Y], and secondary solute molecules [Z]. Solid green lines are excitations to higher states. Solid blue arrows are radiative transitions, fluorescence. Red dashed arrows are non-radiative transitions.

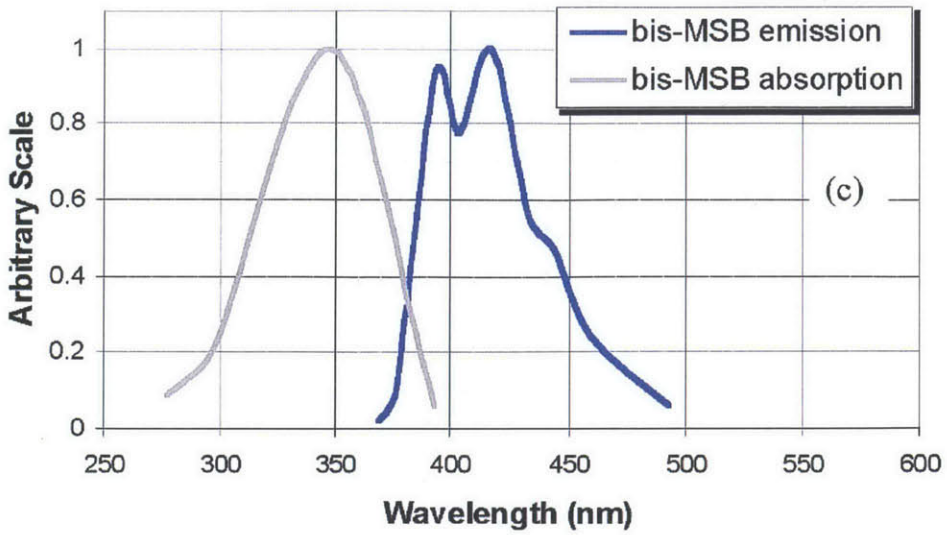

Figure 2.2. Absorption and emission spectra for bis-MSB, a common secondary solute. The small region of overlap are the wavelengths where self-absorption can occur. Image is taken from Viren.[13]

In addition to excited singlet states, inter-system crossing and ion recombination populate excited triplet states, which are not shown. The inter-system crossing is a low probability process in which S_{1X} relaxes to lower energy excited triplet state. Ion recombination preferentially populates excited triplet states over excited singlet states three to one. Higher excited triplet states also undergo internal degradation rapidly transitioning to T_{1X}. Radiative transitions from T_{1X} to S_{0X}, called phosphorescence, are forbidden with lifetimes from microsecond to seconds and its contributions are considered insignificant relative to fluorescence. Another possible transition is the annihilation of two triplet states,

$$T_{1X} + T_{1X} \rightarrow S_{0X} + S_{1X} \tag{2.1}$$

producing additional excited singlet states. These S_{1X} states decay with the same rate and spectrum as the prompt fluorescence but is delayed by the migration time of the triplet states and considered the main contributor to delayed fluorescence. The density of ionization and excitation affects the internal degradation and triplet annihilation processes.

2.2. The Effects of Excitation Density – Pulse Shape Discrimination

In 1968, Laustriat described the spatial distribution of the energy deposition as shown in Figure 2.3. Particles with high specific energy loss, dE/dx, in the solvent will produce regions of high activation along its track and in "spurs" and "blobs" outside the track. Particles with low dE/dx in the solvent will not create a region of high activation along its track. The extent of these high activation regions produce two effects, ionization quenching and increased triplet annihilation, that change the scintillation light profile and can be used to discriminate incident radiation based on its specific energy loss. The specific energy loss for muons, protons, and electrons are shown in Figure 2.4. Although the exact mechanism that suppresses the prompt fluorescence is still disputed, the quenching appears to occur before the lowest excited state S_{1Z} is populated.[12] The high density of ionization appears to provide alternate paths for the higher singlet states that do not lead to the lowest excited state S_{1Z}.

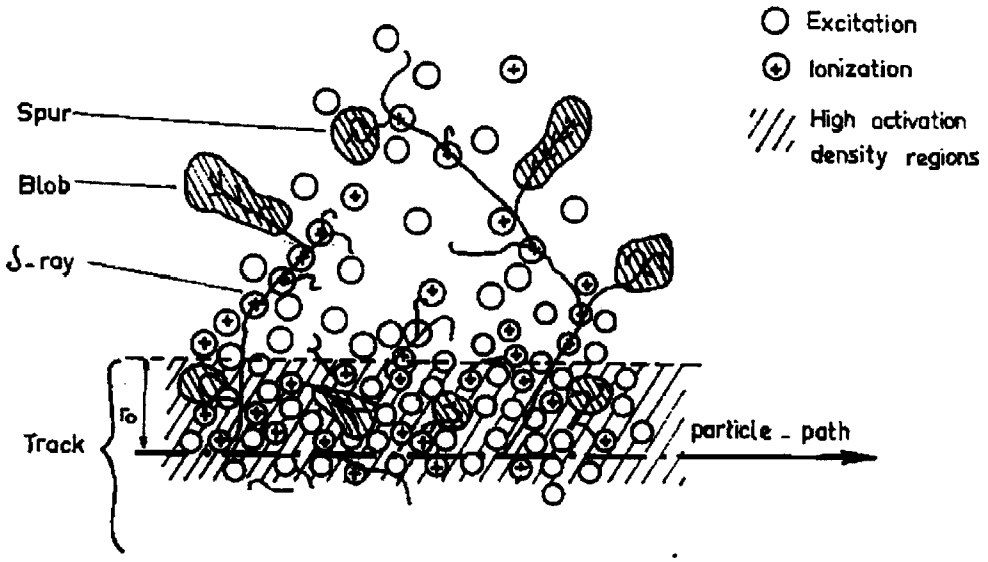

Figure 2.3. Spatial distribution of excitations and ionizations in organic scintillator. Particles with high specific energy loss create a track of high activation density along its path and secondary regions called blobs and spurs. Particles with low specific energy loss only create the blobs and spurs. Image is taken from Laustriat.[14]

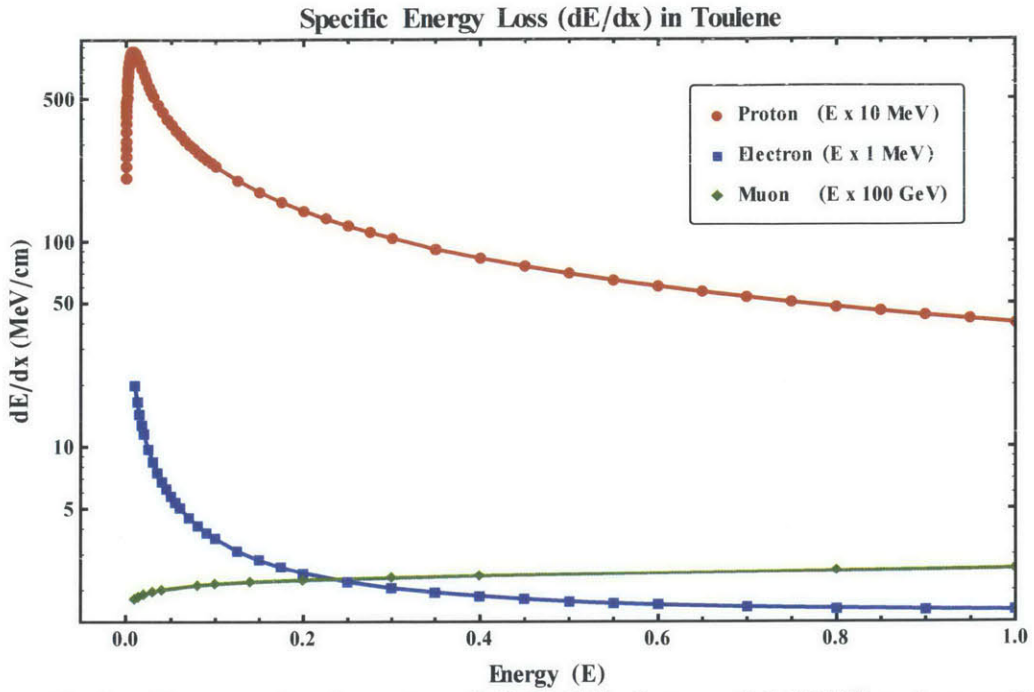

Figure 2.4. Specific energy loss for protons (0-10 MeV)[15], electrons (0-1 MeV)[15], and muon (1-100 GeV)[16] in toluene (C_7H_8). Ionization quenching of luminescence increases with increased specific energy loss.

Birks' semi-empirical formula is commonly used to describe the reduced scintillation response per unit path length dL/dx as a function of dE/dx:

$$\frac{dL}{dx} = \frac{S\frac{dE}{dx}}{\left(1+kB\frac{dE}{dx}\right)} \tag{2.1}$$

where S is the scintillation efficiency and kB describes the fraction of the excitations that are quenched.[17] Craun and Smith added a second order quenching term improving the fit for particle with larger specific energy loss.[18] Increased ionization quenching due to higher specific energy loss leads to a lower scintillation yield as shown in Figure 2.5. The term MeV electron equivalent (MeVee) has been introduced to quantify the light yield of heavy charged particles. A one MeVee proton would have an incident energy of several MeV.

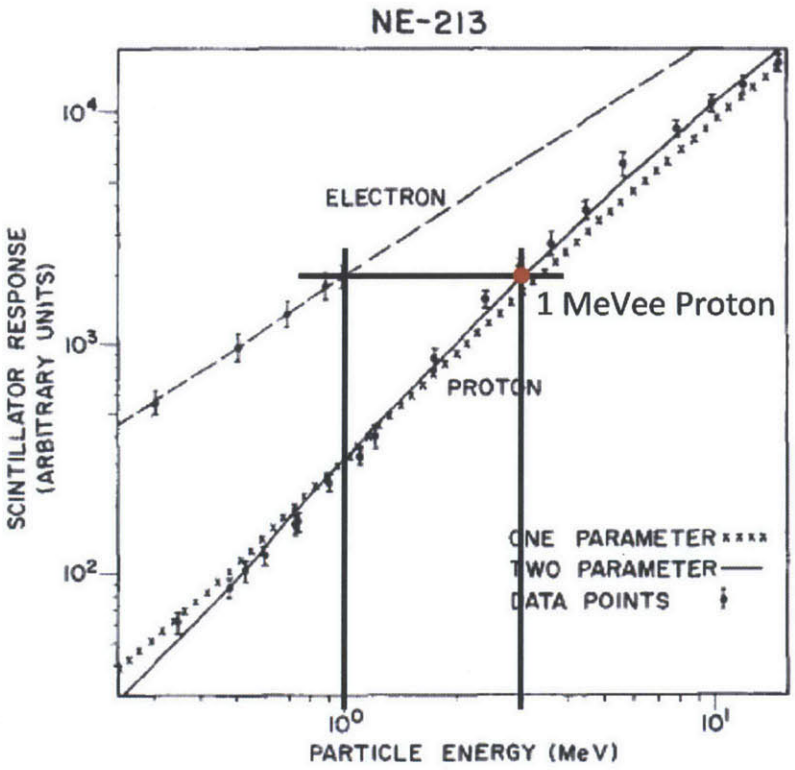

Figure 2.5. Comparison of scintillation light from electrons and protons in a xylene based organic scintillator. Ionization quenching provides alternate paths to internal degradation resulting in reduced prompt fluorescence for higher specific energy loss particles like protons. A 1 MeVee proton has the same light production as a 1 MeV electron but has an incident energy of 3 MeV. Image taken from Craun and Smith.[18]

The second effect introduced in regions of high activation is increased triplet annihilation. As described in Section 2.1, excited triplet states are primarily populated by ion recombination. Regions of high ionization lead to higher densities of triplet states increasing the delayed fluorescence contribution to the total scintillation light. Figure 2.6 shows the differential and integral pulses in a xylene based liquid scintillator (NE213) from a gamma ray and a neutron interaction. The scattered proton from the neutron interaction has a larger specific energy loss than the scattered electron from the gamma ray interaction. The resulting delayed fluorescence remains a small fraction of the total scintillation light but this difference in pulse shape can be detected with common pulse shape discrimination techniques and provide

the means to discriminate incident radiation based on its specific energy loss. It is generally accepted that the population of the long-lived triplet states is the source of the delayed fluorescence and any processes that inhibit (quench) this population will degrade the pulse shape discrimination capability. Many organic scintillators have inherent processes that quench the population of triplet states and therefore do not exhibit the pulse shape discrimination capability. Oxygen dissolved in the scintillator reduces the overall scintillation light and can quench the delayed fluorescence resulting in degraded or destroyed pulse shape discrimination capability.[12, 14, 17] Oxygen degassing in liquid scintillators can be achieved by nitrogen bubbling.

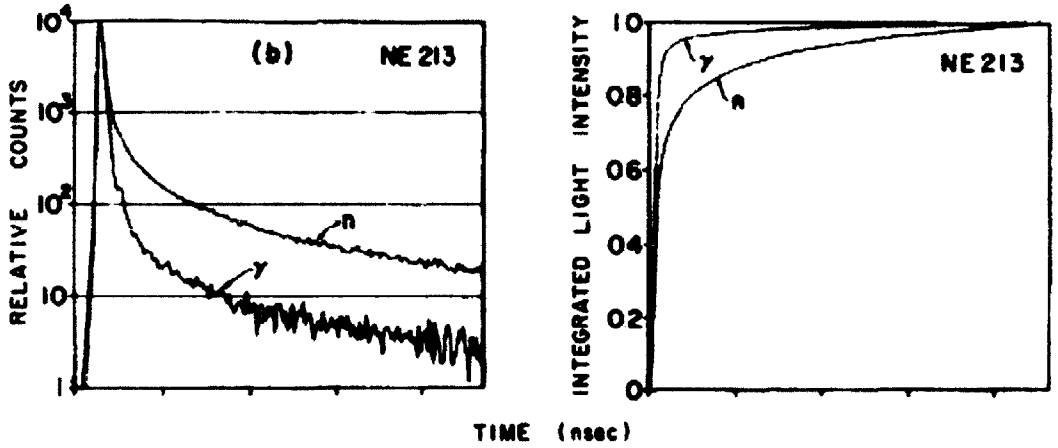

Figure 2.6. Differential and integrated curves showing the time dependence of gamma ray versus neutron response in a xylene based liquid scintillator. The time dependence can be used to differentiate incident radiation based upon its specific energy loss (*dE/dx*). Images taken from Kuchnir et al.[19]

2.3. Scintillation Light from Muons, Neutrons, and Gamma Rays

The final scintillation light from muon, neutron, and gamma ray interactions will vary significantly based upon their energy and the path length in the scintillator including the effects due to the incident angle. In this section, we will describe the expected angular and energy distributions for each type of incident radiation, the types and probabilities of interactions inside the scintillator, and estimate the expected scintillation light. The muon angular and

energy distributions are well documented and originate from cosmic ray interactions in the Earth's atmosphere. The neutron and gamma ray distributions will be based on a simple implosion-type nuclear weapon, which will be compared to an Americium-Beryllium (Am-Be) source, a common industrial neutron source

2.3.1. Muon Source and their Interactions

Terrestrial muons are a result of pion and kaon decay following a primary cosmic ray's interaction in the upper atmosphere. This initial interaction produces many short-lived particles in a hadronic cascade, but the muon's mass, energy, and half-life generally allow it to travel through the remainder of the Earth's atmosphere and penetrate the Earth's surface. Muons passing through the atmosphere at large zenith angles have longer path lengths and are less likely to reach the surface. The final muon distribution at surface has been well characterized and the angular distribution is found to be proportional to the square of the cosine of the zenith angle, $P(\theta) \propto cos^2\theta$. As shown in Figure 2.7, the muon flux is predominately vertical with fifty percent of muons incident at zenith angles less than 37.5°. This results in a commonly quoted muon flux of 1 muon min^{-1} cm^{-2} at sea level.[20]

With a mean lifetime of 2.2 μs very few muons would survive the trip through the atmosphere but since muons are produced at relativistic energies they experience a time dilation and some live long enough to penetrate over a thousand meters into the Earth's surface. The mean energy at sea level is approximately 4 GeV and increases with increasing depth. Similar to electrons, muon primary interactions of interest in matter are collisional (Bethe-Bloch) or radiative (Bremsstrahlung).[16] The muon, being 200 times heavier than the electron, generally does not experience the same large angle scattering when interacting with orbital electrons. The specific energy loss remains relatively constant at 2.3 MeV cm^2/g in the 1-10 GeV region.[16] With a low and constant specific energy loss, the scintillation light per

distance, dL/dx, will also be constant. For EJ-309 an OLS from Eljen Technology[21] the muon scintillation light per unit of distance is:

$$\frac{dL}{dx} = \frac{dL}{dE}\frac{dE}{dx}\rho \approx 11{,}500\ \frac{photons}{MeV}\,2.3\,\frac{MeV\ cm^2}{g}\,0.964\ \frac{g}{cm^3} \approx 25{,}500\,\frac{photons}{cm}. \qquad (2.2)$$

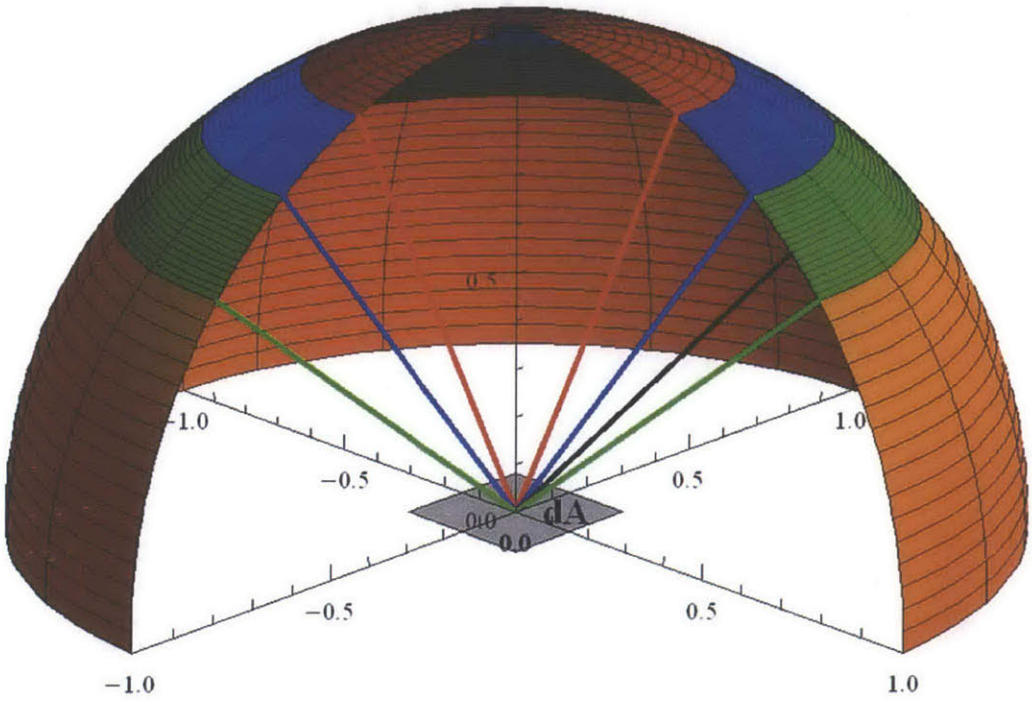

Figure 2.7. The cosmic ray muon angular distribution is proportional to the square of the cosine of the zenith angle. Each colored section represents 25% of the incident muons. Fifty percent are incident at zenith angles less than 37.5°. The black line is at 45°. Integration over all angles gives a muon flux of ~1 min^{-1} cm^{-2}.

The angular distribution of muons determines the expected path through a horizontal tube, the orientation during all laboratory testing, of a given diameter. A simulation was written to randomly sample the muon angular distribution $P(\theta) \propto cos^2\theta$ and determine if the sampled muon trajectory crossed the tube. As shown in Figure 2.8, when a muon intersects the tube, the simulation records its path length and then finds the mean path length of all muons passing through the tube. The mean path length is determined to be $(86 \pm 3)\%$ of the horizontal tube

diameter. Therefore, a 5mm diameter tube filled with EJ-309 will have a mean scintillation light of approximately $(11{,}000 \pm 400)$ photons.

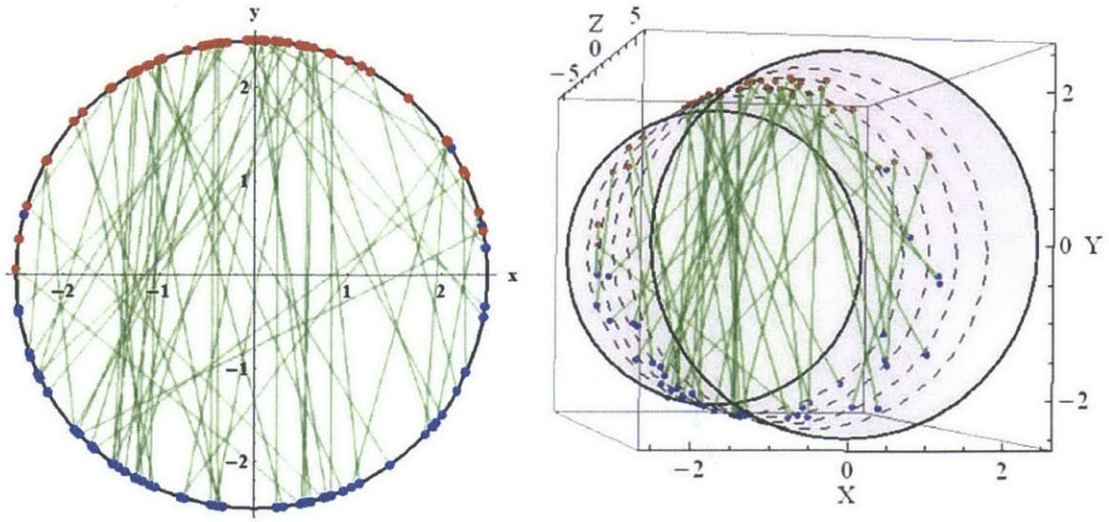

Figure 2.8. Estimating the muon path length through a horizontal tube. Based on the muon angular distribution at sea level the simulation randomly chooses a muon path and determines the path length through the tube. The mean path length is determine to be 86 ± 3 % of the diameter.

2.3.2. Neutron Sources and their Interactions

When authorities locate an unknown neutron source, the ability to determine if it is a nuclear yield producing device or not is critical to formulating the proper government response. The most common nuclear yield-producing material that has a prominent neutron signature is plutonium. It is important to recognize that highly enriched uranium (HEU) produces an almost undetectable ~2 neutrons s^{-1} kg^{-1}.[8] At ten meters away, this results in an un-attenuated flux of 1.5 neutrons m^{-2} min^{-1}, significantly below the fluctuating background of 60 neutrons m^{-2} min^{-1} from cosmic rays. Weapons grade plutonium (WgPu), in contrast, emits 56,000 neutrons s^{-1} kg^{-1}. Fetter et al. describes four hypothetical implosion-type, nuclear weapon designs using either HEU or WgPu as the fissile core, and either tungsten or depleted uranium as the tamper.[8] In my analysis, I will use the WgPu core with a depleted uranium tamper model as shown in Figure 2.9. The purpose of the dense tamper is to provide a large inward

momentum to counter the expansion of the fissile core as it becomes super-critical and begins to expand. The last few generations in the nuclear chain reaction, which occurs on a timescale of 10 ns, produces the bulk of the yield. Even modest increases in the number of generations before the weapon disassembles will significantly increase its yield. Fast neutron-induced fissions in the ^{238}U also increases the weapon's yield.

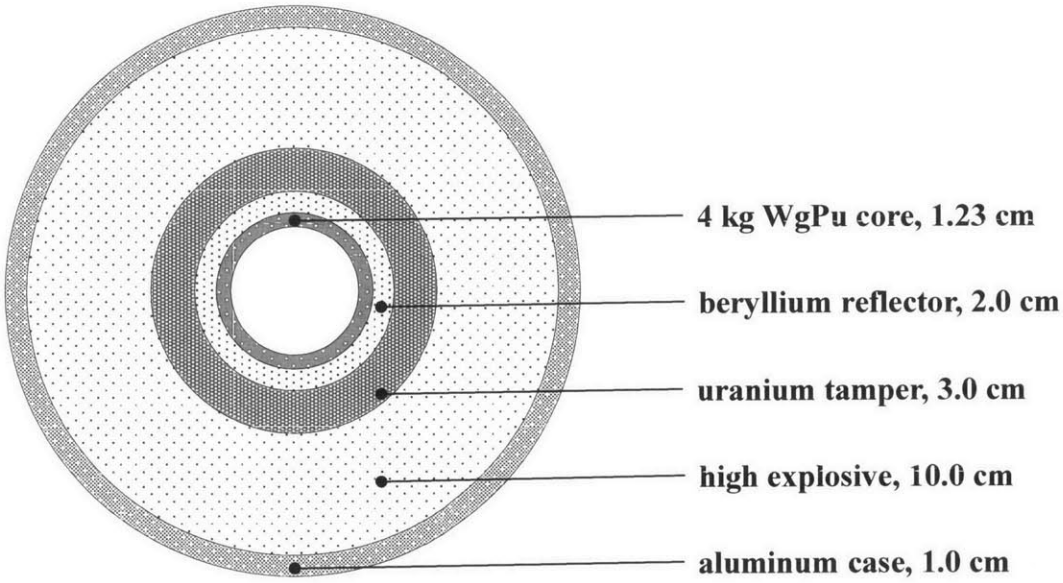

Figure 2.9. Hypothetical implosion-type nuclear weapon made of concentric sphere shells with a hollow center. The fissile core consists of 4 kg of weapons-grade plutonium with a thickness of 1.23 cm and an outer radius of 7 cm. The tamper is made of depleted uranium. Measurements provided are the thickness of each shell giving an overall outer diameter of 46 cm. Reproduced from Fetter, et al..[8]

The exact isotopic composition of WgPu will vary based on its production process but the fraction of isotopes with high spontaneous fission rates, specifically ^{238}Pu, ^{240}Pu, and ^{242}Pu, are generally kept below 7%. The presence of neutrons from spontaneous fission can initiate the nuclear chain reaction and the subsequent expansion too early, reducing the total number of generations in the reaction and significantly reducing the weapon's yield.[a] Table 2.1

[a] When a nuclear weapon pre-initiates and does not achieve its intended nuclear yield it is called a fizzle. It was determined during the Manhattan Project that plutonium could not be used in a gun-type design, a design in which two sub-critical masses driven together by explosives, because the spontaneous fission neutrons would cause pre-initiation.

summarizes the contribution of each isotope to this model's neutron signature. Spontaneous fission neutrons from ^{240}Pu and their induced fission neutrons are the largest contributors producing over 400,000 neutrons per second at the surface of the weapon.

Table 2.1. Estimated Neutron Source Escaping Surface of a Plutonium Based Nuclear Weapon.[22]

Plutonium Isotope	Spontaneous Fission Neutrons (s^{-1} kg^{-1})	(α,n) Neutrons (s^{-1} kg^{-1})	Fractional Composition	Total* (s^{-1})
238	2,600,000	220,000	0.00005	1009
239	22	630	0.933	4734
240	910,000	2,300	0.060	426800
241	500	22	0.0044	16
242	1,700,000	33	0.00015	2018
			TOTAL	**430,000**
*** Total for 4 kg of WgPu and a 1.94 multiplication from self-induced fission and (n,2n)**				

The neutron energy distribution, from spontaneous fission and neutron-induced fission, can be described by a Watt spectrum:

$$W(a,b,E') = \sqrt{\pi \frac{b}{4a} \frac{e^{\frac{b}{4a}}}{a}} e^{-aE'} \sinh \sqrt{bE'} \tag{2.3}$$

where E' is the secondary neutron energy, and a and b are parameters specific to the isotope of interest.[23] For neutron-induced fission, a is dependent on the incident neutron energy as:

$$a(E) = a_0 + a_1 E + a_2 E^2 \tag{2.4}$$

where the coefficients a_0, a_1, and a_2 are tabulated for fissionable isotopes. The neutron energy distributions for ^{240}Pu spontaneous fission, ^{252}Cf spontaneous fission, and neutron-induced fission in ^{239}Pu are shown in Figure 2.10. The majority of fission neutron will be created between 0.1 MeV and 10 MeV with a mean energy of approximately 2 MeV. Am-Be is a common industrial neutron source in which an alpha particle from the americium interacts with the beryllium to produce a neutron (α,n). Although the interaction produces a more

complicated neutron energy distribution as shown in Figure 2.10, the energy range is similar to fission neutrons.

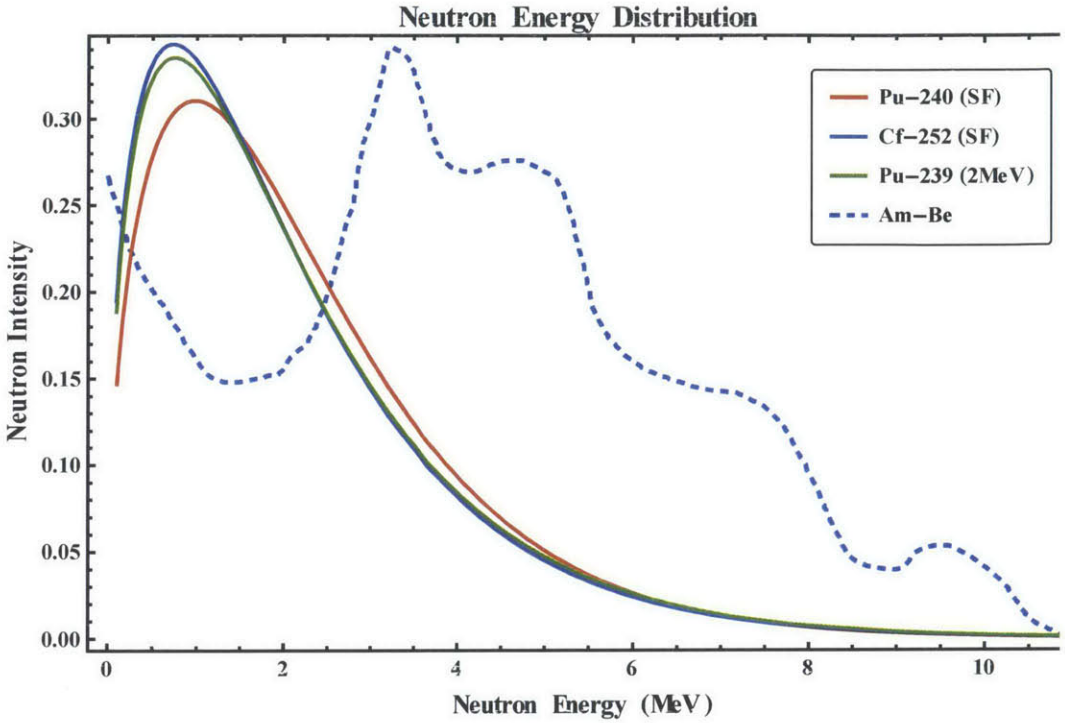

Figure 2.10. Neutron energy distribution for spontaneous fission of ^{240}Pu and ^{252}Cf, neutron-induced fission in ^{239}Pu, and alpha-neutron interaction (α,n) in Am-Be. The fission energy spectrum is defined by the Watt spectrum.[23] In the Am-Be neutron source an alpha particle from the ^{241}Am interacts with the Be to produce a neutron.[24]

The primary constituents of liquid scintillators are hydrogen and carbon; EJ-309 has a 1.25 H/C ratio. The dominant neutron interaction in hydrogen and carbon, over all neutron energies of interest, is elastic scattering as shown in Figure 2.11. In the fission-neutron energy range, the elastic scattering cross-sections remain essentially constant at 20 barns for hydrogen and 5 barns for carbon. Based on the larger cross section and more atoms per molecule, more than 80% of the interactions that occur will be with hydrogen. The low probability carbon scattering events produce little scintillation light and will only contribute to the low-level noise region of the spectrum. Elastic neutron scattering with hydrogen results in a recoil proton with

a maximum energy equal to the incident neutron energy and a mean energy equal to one-half of the incident neutron energy.

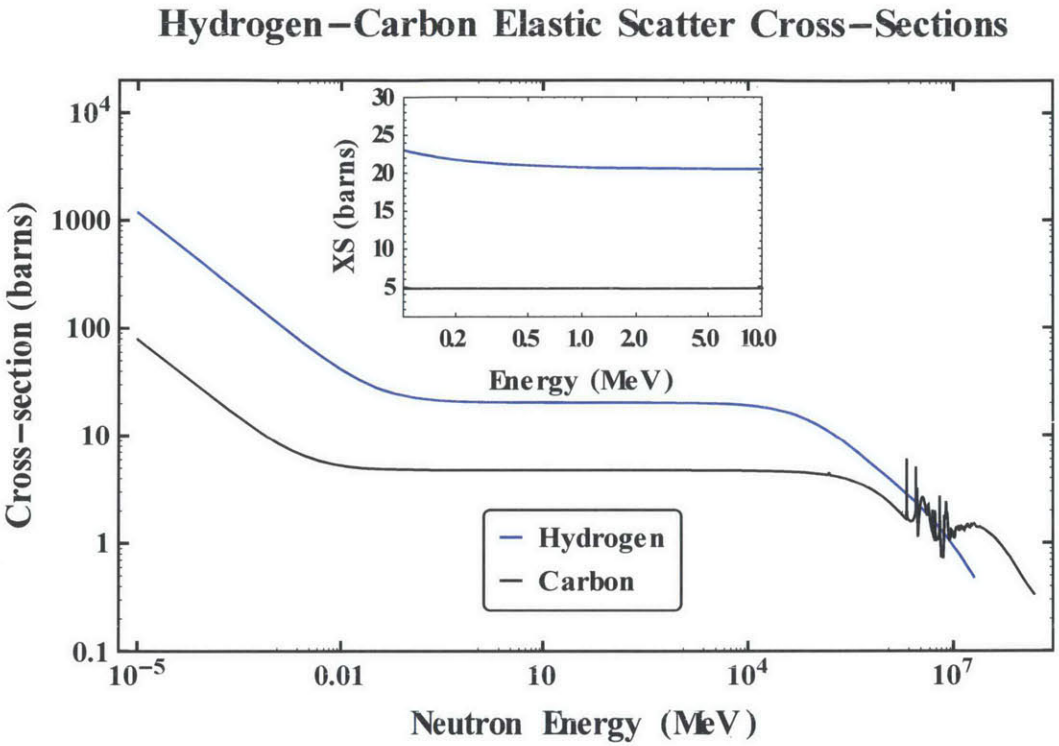

Figure 2.11. Elastic scatter neutron cross-section for hydrogen and carbon. Elastic scatter cross-section dominates at all energies of interest. In the fission neutron energy region (0.1 MeV to 10 MeV), the cross-sections remain almost constant at 20 barns for hydrogen and 5 barns for carbon as shown in the inset.[25]

Using the Watt spectrum for incident neutrons gives a mean recoil proton energy of 1.2 MeV. As discussed earlier, the larger specific energy loss of protons result in ionization quenching and reduced scintillation light. Using the empirical formula from Katz, Sharma, and Homayoonfar,[26] recent studies have characterized the neutron light output in EJ-309.[27, 28] For scattering on hydrogen the formula for the light output in MeVee is:

$$L(E_p) = aE_p - b(1 - e^{-cE_p}) \tag{2.5}$$

where a, b, and c are experimentally determined and E_p is the recoil proton energy in MeV. This provides the final piece of information required to estimate the range of scintillation light in EJ-309 from fission and Am-Be neutrons. Figure 2.12 shows the expected scintillation light as a function of recoil proton energy. Based on the neutron energy spectra we can estimate most recoil protons will be between 1 MeV and 3 MeV with a scintillation light between 1,700 photons and 10,400 photons.

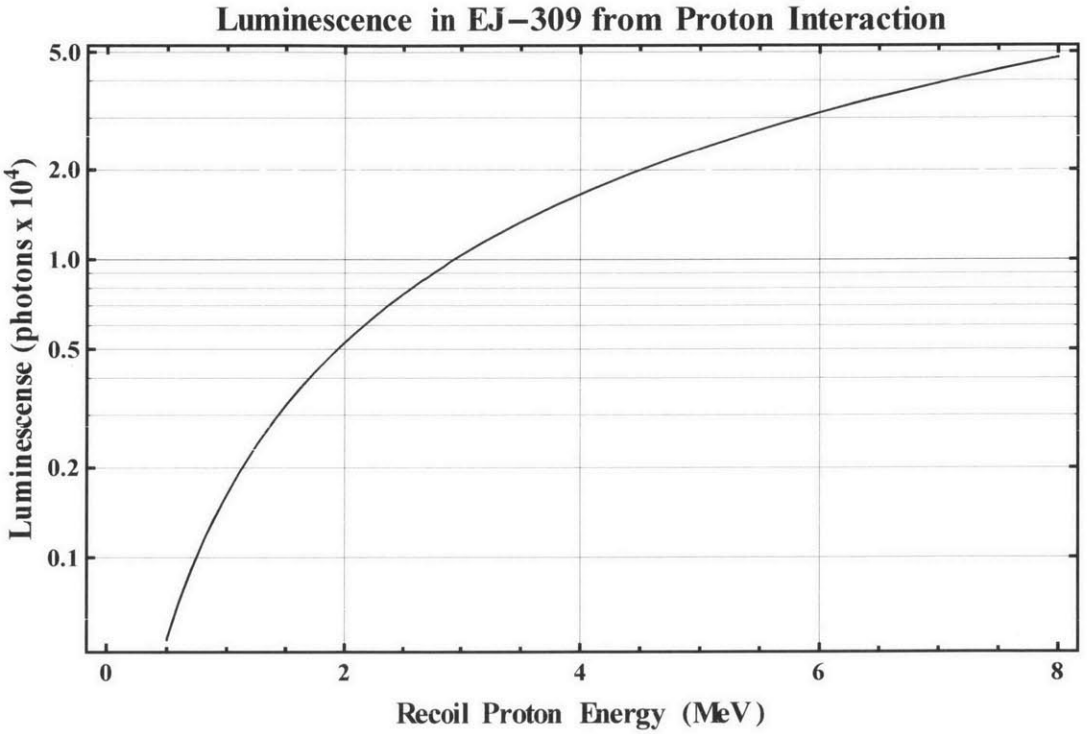

Figure 2.12. Scintillation light produced in EJ-309 as a function of recoil proton energy. The range of proton energy is based on the incident neutrons from ^{240}Pu and Am-Be interacting with hydrogen. The reduced scintillation light in EJ-309 due to the high specific energy loss of protons is based on data published in 2013 by Enqvist et al.[27]

2.3.3. Gamma Rays and their Interactions

The requirement for coincidence in multiple detection modules for tracking purposes makes any effects of gamma rays on the cosmic ray imager insignificant. On the other hand, gamma rays incorrectly identified as neutron can have a significant effect on the ability to

determine if an unknown neutron source is SNM or not. Because the fission process produces multiple neutrons, it is possible to detect a higher number of neutrons per time interval as compared to neutron sources not undergoing fission. Gamma ray events counted in the detection modules could alter the timing information and make it impossible to ascertain accurate information about the neutron source.

There are many gamma ray producing decays and interactions in the nuclear weapon model discussed in section 2.3.2. Gamma ray self-shielding, the absorption and scattering of gamma rays occurring inside the nuclear weapon, further complicates the gamma ray spectrum at the weapon's surface. The dominant gamma ray emission at the surface of the model is a decay product of ^{238}U with a 1.001 MeV line and a rate of 60,000 per second.[22] Gamma rays interact primarily with the carbon content of an organic scintillator to produce secondary electrons. Figure 2.13 shows the three primary gamma ray interactions inside an OLS; photoelectric effect, Compton scattering, and pair production; and the dominant interaction at an incident energy of 1 MeV is Compton scattering.

The secondary electrons from Compton scatter will have a kinetic energy, T_e, equal to:

$$T_e = E_\gamma \frac{1-Cos\theta}{(m_0c^2/E_\gamma)+1-Cos\theta} \tag{2.6}$$

where E_γ is the incident gamma ray energy, m_0c^2 is the electron rest mass energy, and θ is the scattered photon angle. This produces the well-known Compton edge associated with the maximum energy transferred to the secondary electron when the incident gamma ray is scattered at 180°. Figure 2.14 shows the calculated Compton electron energy distribution based on the Klein-Nishina formula. With a negligible photoelectric cross section and a low probability of multiple Compton scatters inside the small detector module, the maximum energy deposited will correspond to this Compton edge. For a 1 MeV gamma ray the maximum

Compton electron energy is 0.8 MeV. Assuming the electron deposits all of its energy, there are approximately 9,200 photons produced in the liquid scintillator. Neutrons can produce the same amount scintillation light making their discrimination difficult.

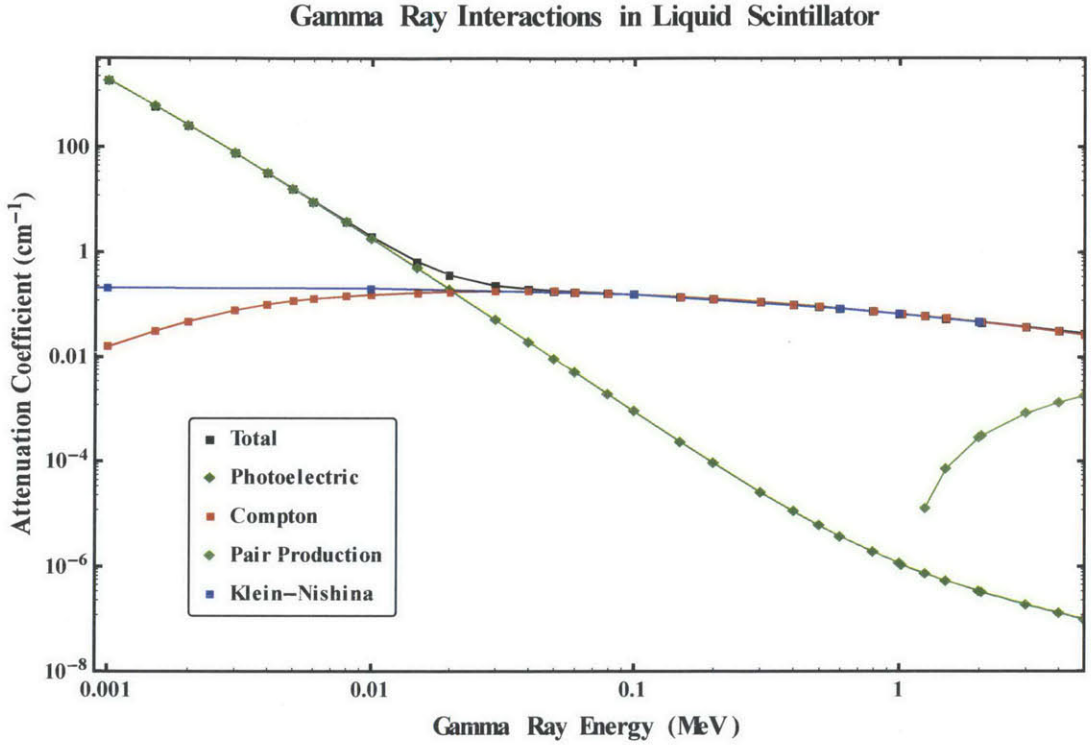

Figure 2.13. Attenuation coefficients in organic liquid scintillator for 1 keV to 5 MeV gamma rays.[29] Compton scatter is the primary interaction for gamma ray energies between 0.1 MeV and 1.0 MeV. Klein-Nishina calculation shown for comparison.

As discussed, the gamma ray sources from nuclear weapons and natural background produce a wide range of secondary electron energies, but the majority will fall below 2 MeV. Because strontium-90 (Sr-90) beta particles have an energy range from 0 to 2.2 MeV, it is used in many of the preliminary tests discussed later. Secondary electrons and betas will undergo the same energy depositing processes in the liquid scintillator although secondary electrons will be created at the gamma ray interaction point throughout the detector volume. This may cause some electron to interact in the wall of the detector before all of its energy is deposited in the OLS.

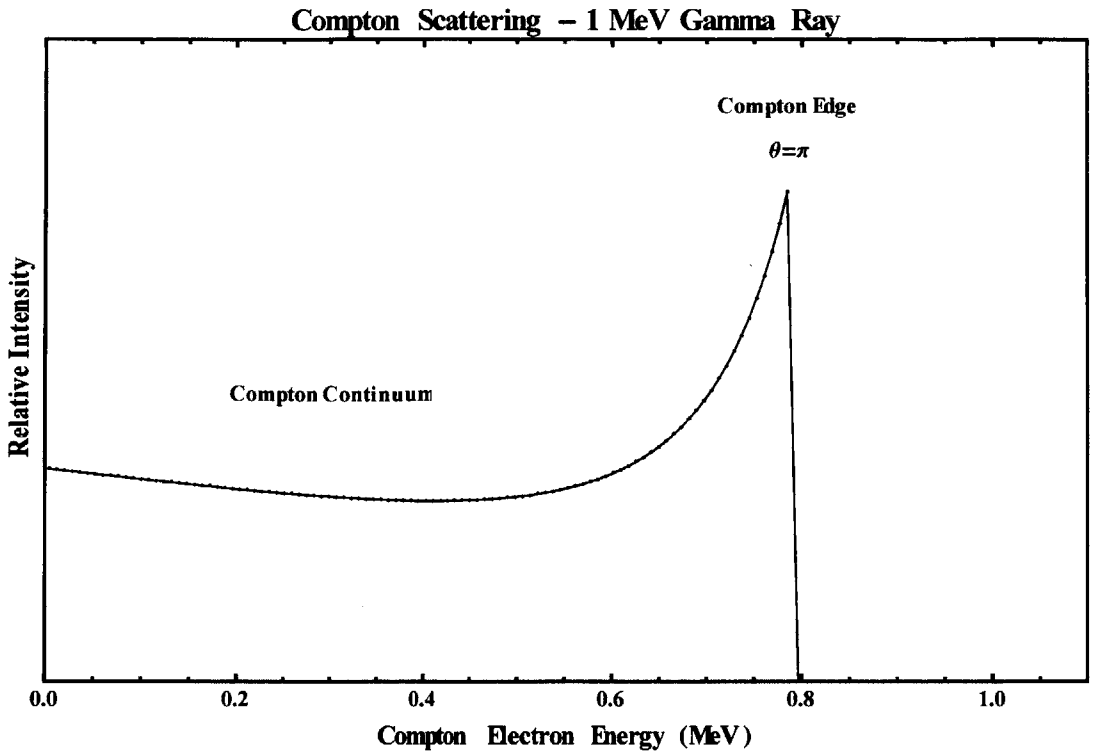

Figure 2.14. Compton continuum for a 1 MeV gamma ray. The Klein-Nishina formula describes the angular distribution of Compton scattering, and therefore, the Compton electron energy distribution. The maximum energy transfer occurs when the gamma ray is back scattered and corresponds to the Compton edge. This is the maximum energy deposited in the liquid scintillator assuming the probability of multiple Compton scatters in the small detector module is very low.

2.3.4. Summary of Expected Scintillation Light

Many factors will affect the actual scintillation light produced inside the OLS filled fluoropolymer tube. Based on the initial calculations the expected scintillation light is summarized in Table 2.2. In general, the detection module must be able to detect a localized signal of 10,000 photons produced anywhere along its length of 2-meters. For a detection module with a 1:400 ratio of diameter to length, efficient light collection becomes critical.

Table 2.2. Estimated Light Production for Muons, Neutrons, and Gamma Rays

Incident Particle	Expected Energy	Secondary Particle	Expected Scintillation Light (Photons)
Muon	4 GeV	NA	11,000
Neutron	2-6 MeV	Proton	1,600 - 10,400
Gamma Ray	1.001 MeV	Electron	9,200

3. Analysis of Light Collection Options

As discussed in chapter 1, the cosmic ray imaging (CRI) prototype was constructed using 5 mm diameter by 1-meter long plastic scintillating fibers because the OLS filled PTFE tubes demonstrated extremely poor attenuation. Since plastic fibers are not a viable option for scaling the CRI up to a 2-meter length, an alternative OLS based system is still required. With a 1:400 diameter to length ratio, an efficient method to propagate the scintillation light produced in the liquid scintillator to the photomultiplier tube (PMT) is critical.

A potential solution is to couple a wavelength shifting (WLS) fiber to the OLS filled PTFE tubing. The OLS light entering the WLS fiber is first absorbed and then isotropically re-emitted at longer wavelengths. Due to total internal reflection (TIR), the WLS fiber channels the portion of the photons re-emitted at angles greater than the critical angle down the fiber to the PMT.

To understand fully the optical parameters that caused the poor attenuation length in the OLS filled PTFE tubing and to evaluate potential WLS fiber configurations a three-dimensional light propagation simulation was created. In this chapter, I first review the important principles of light propagation to include the law of refraction, Fresnel's formulas, TIR, and specular and diffuse reflection. I also highlight Janecek and Moses' recent work on characterizing common reflector materials, which provides the probability distribution functions used in the simulation to determine the angle of reflection at the fluoropolymer boundaries.[30-34] Next, I describe the simulation and compare its results to initial measurements of the OLS filled PTFE tubes. Finally, I modify the simulation to incorporate WLS fibers to read-out the scintillation signal to the PMTs and estimate the expected signals.

3.1. Important Principles of Light Propagation

In my simulation, the fundamental light propagation principles applied are the law of refraction, Fresnel's formulas, TIR, and specular and diffuse reflection. The law of refraction, also called Snell's law, states light incident on a boundary between two materials with different indices of refraction will follow $n_1 \sin\theta_i = n_2 \sin\theta_t$ where the incident angle relative to the normal is θ_i, and the transmitted angle relative to the normal is θ_t as shown in Figure 3.1. Fresnel's formulas, derived from Maxwell's equations, give the intensities of the reflected and transmitted electromagnetic waves. The reflection coefficients for polarization parallel and perpendicular to the surface are:

$$R_{\parallel} = \left|\frac{n_1 \cos\theta_i - n_2 \cos\theta_t}{n_1 \cos\theta_i + n_2 \cos\theta_t}\right|^2 \qquad R_{\perp} = \left|\frac{n_2 \cos\theta_i - n_1 \cos\theta_t}{n_1 \cos\theta_t + n_2 \cos\theta_i}\right|^2 \tag{3.1}$$

and the transmission coefficients for polarization parallel and perpendicular to the surface are:

$$T_{\parallel} = 1 - R_{\parallel} \qquad T_{\perp} = 1 - R_{\perp}\,.^{35} \tag{3.2}$$

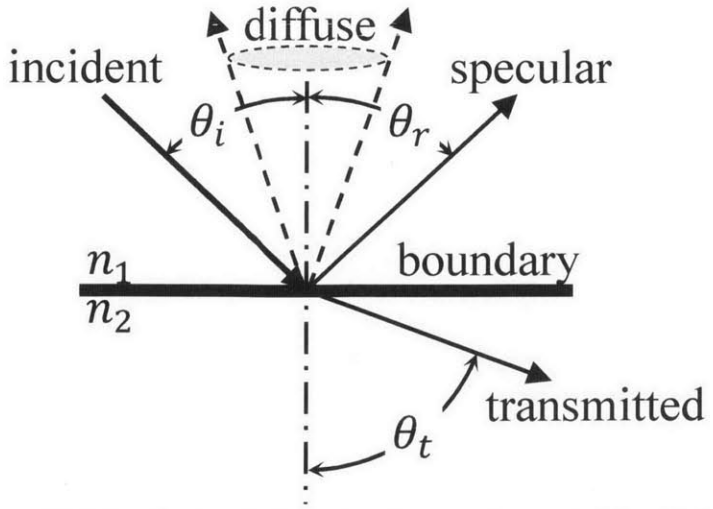

Figure 3.1. Diagram of light incident on the boundary between two materials with indices of refraction n_1 and n_2. The transmitted light obeys the law of refraction. The direction of the reflected light will depend on the nature of the boundary. In specular reflection, $\theta_i = \theta_r$. In diffuse reflection, the reflected angle is random is random in nature.

Since the OLS produces scintillation photons with random polarization, the average of the parallel and perpendicular coefficients are used. Figure 3.2 shows the reflection coefficients for light in the PTFE ($n_1 = 1.37$) wall incident on EJ-309 ($n_2 = 1.57$) and for light in the EJ-309 ($n_1 = 1.57$) incident on PTFE ($n_2 = 1.37$) as a function of incident angle, θ_i. The bottom graph also shows the conditions for TIR. Light that is incident on a medium having a lower index of refraction than the current medium and incident at angles greater than the critical angle, θ_C, will have a reflection coefficient equal to 100% (R=1).

Reflections are generally characterized as specular or diffuse, as illustrated in Figure 3.1. In specular reflection, the reflected angle is equal to the incident angle. In diffuse reflection, the reflected angle is pseudo-random with a distribution based on the material properties. Most materials display some combination of specular and diffuse properties; becoming more diffuse at small angles of incidence and becoming more specular at large angles of incidence. Janecek and Moses characterized many common reflectors materials (e.g., PTFE and titanium dioxide, TiO_2) to include the materials' diffuse and specular behavior as a function of incident angle.[30-34] They used the experimental setup shown Figure 3.3 with a 440 nm laser, which is closely matched to EJ-309's peak emission wavelength, to measure the angular response in 4° increments in the θ direction and 5° increments in the ϕ direction. The results for PTFE, also in Figure 3.3, shows predominantly diffuse reflections except at large incidence angles, for the laser source. The angular distributions for PTFE and TiO_2 were used as probability distribution functions in the simulation to determine the angle of reflection at the boundaries.

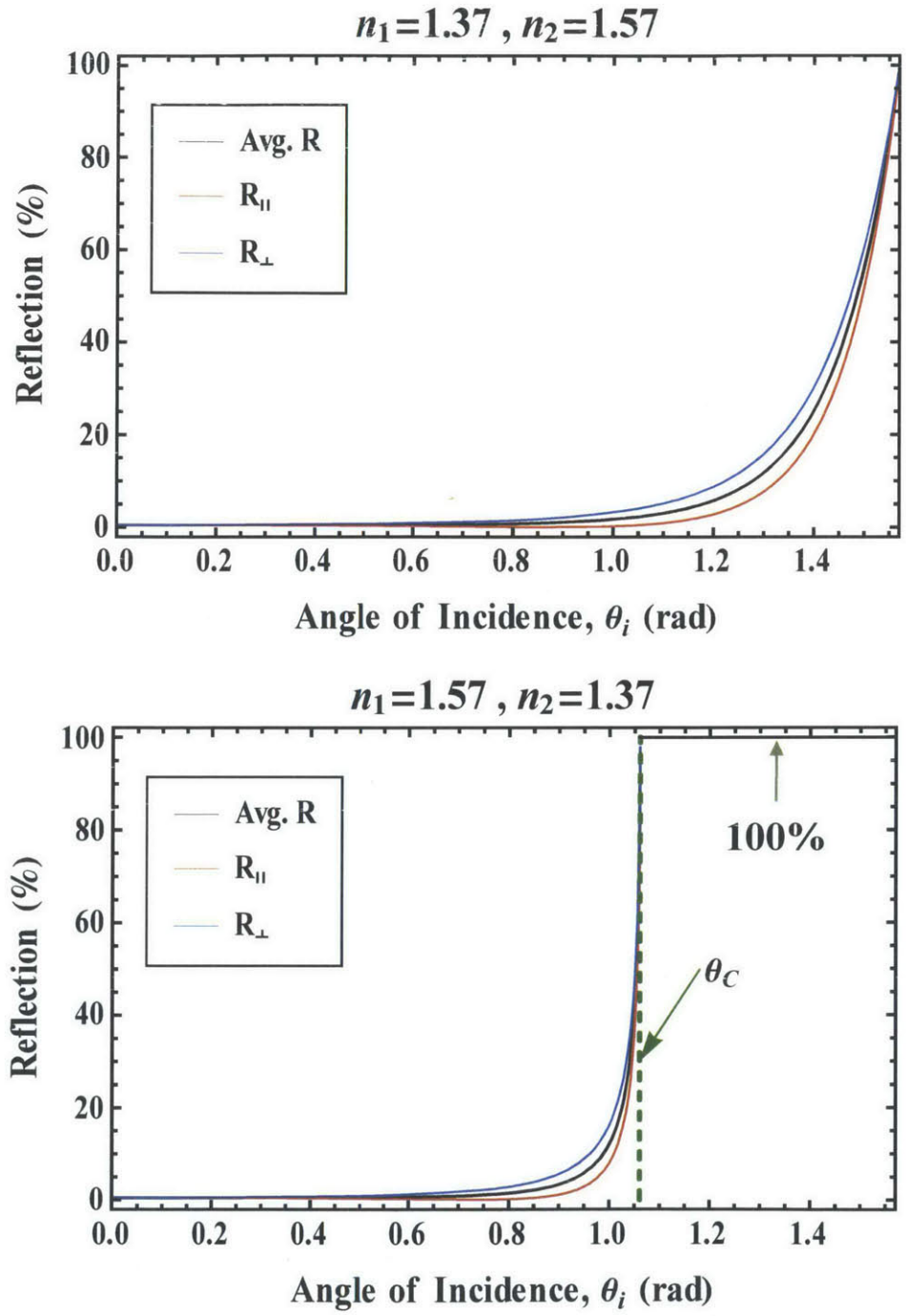

Figure 3.2. Plots of reflection coefficients based on Fresnel's formulas for boundaries between EJ-309 (n = 1.57) and PTFE (n = 1.37). Top: Light entering EJ-309, having a higher index of refraction than PTFE, will not experience TIR. Bottom: Light entering PTFE, having a lower index of refraction than EJ-309, will undergo TIR at incidence angles greater than the critical angle, θ_C, i.e., for $\theta_i > \theta_C$, R=100%.

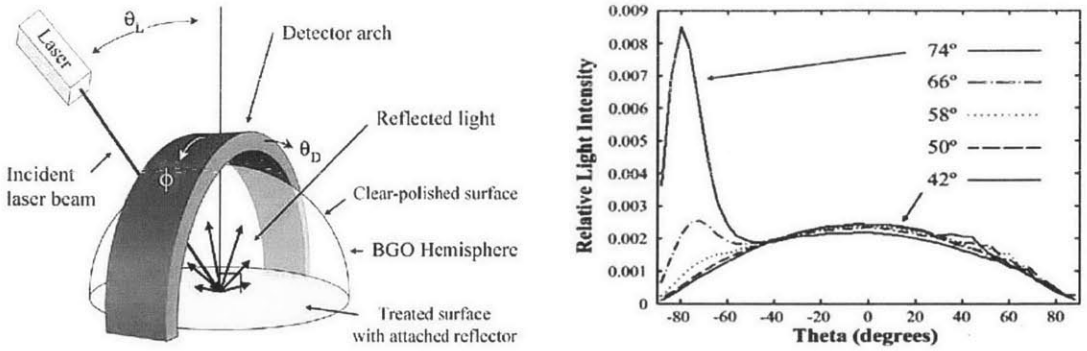

Figure 3.3. Measurements of optical properties of common reflectors. Left: Experimental setup to determine the reflective properties where θ_L is the laser angle of incidence, and θ_D and ϕ describe the position of the detectors that measure the reflected laser light. Image taken from Janecek and Moses.[34] Right: Measurement of PTFE reflectivity as a function of θ_D at $\phi=0°$ for laser angles of incidence equal to 42°, 50°, 58°, 66°, and 74°. PTFE shows a predominantly diffuse reflectivity with specular properties at larger laser angles of incidence. Image taken from Janecek and Moses.[31]

3.2. Model of Light Propagation

3.2.1. Light Propagation in Plastic Fibers

The propagation of light in a plastic scintillating fiber with an outer cladding is significantly different from the propagation of light in a PTFE tube filled with organic liquid scintillator. Careful control of the interface between the core and the outer cladding is possible in the drawing process of a plastic fiber, which results in a mostly specular interface with minimal wall losses.[36] The cladding-air interface is more difficult to control and susceptible to damage from handling, which results in rapid attenuation, within tens of cm, of light trapped between the cladding-air interface and the cladding-core interface.

Light incident on the core-cladding interface at incident angles, measured from the surface normal, greater than the critical angle, θ_c, experience total internal reflection (TIR) and are trapped in the fiber. The trapping efficiency, ε_t, is defined as the fraction of isotropic light

from a point inside the fiber that experiences TIR. At points along the axis of the fiber, the trapping efficiency is

$$\varepsilon_t = \Omega/2\pi = \left(\int_0^{2\pi}\int_0^{\frac{\pi}{2}-\theta_c} \sin\theta \, d\theta \, d\phi\right)/2\pi \tag{3.3}$$

where Ω is the solid angle of the cone defined by the critical angle θ_c. For circular fibers, the trapping efficiency increases as the radial distance from the central axis increases. Attenuation of the trapped light does occur and is primarily due to diffusion and absorption in the core material.[37] A typical plastic fiber has a trapping efficiency of 3%-6% and over 60% of its light remaining at 1-meter.[38]

Note that assuming specular reflections for our OLS filled tube, the trapping efficiency would be over 12% and nearly 40% of its light would remain at 1-meter, but measurements show a much poorer performance.

3.2.2. Description of Simulation

In order to understand the effects of the OLS-fluoropolymer interface causing this poor light propagation performance and to consider alternative module configurations, a three-dimensional light propagation model was written. The simulation characterizes the light collection of the OLS-fluoropolymer tube as a function of radial and axial position and independent of the type of radiation incident on the module.

In contrast to the specular reflections of the plastic fiber, here we assume a mixed specular/diffuse behavior at the tubing wall containing the OLS. In this case, photons at any point can be reflected outside of the trapping cone (i.e., at an incident angle smaller than the critical angle) which results in light loss out of the tube and poorer channeling. Shown in Figure 3.4 is a schematic of the initially proposed detection module. In the simulation

developed, the tube length, inside and outside diameters, and reflection properties of the inner walls are parameters that can be modified.

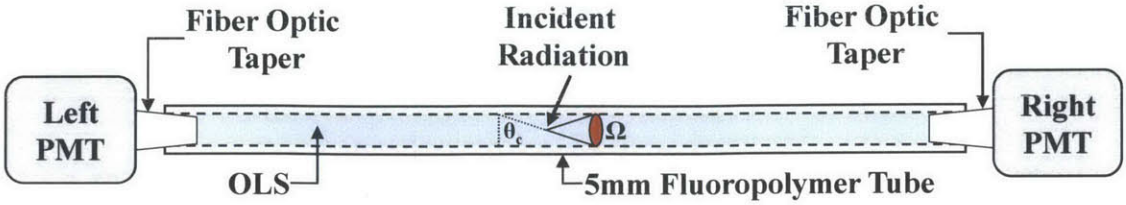

Figure 3.4. Schematic of organic liquid scintillator filled fluoropolymer tube (not to scale).

The flow of the simulation is show in Figure 3.5. The configuration file establishes key parameters such as the dimensions of the system, the indices of refraction for all materials, and the number of photons to be tracked, N. Each tracking loop starts with a photon at a known location with a known trajectory and ends with a new location and trajectory or the termination of the photon (e.g., the photon is collected in the PMT or it exits out the side). Initially, each photon is created isotropically at a given start position, giving the photon its initial position and direction. The photon is then tracked as it moves to and interacts with the next boundary. The simulation determines if the photon crossed the end of the tube before it reached the boundary, where it assumes it will be collected at the PMT. If the photon is located on the cladding-air interface and no surface is intersected then the photon is exiting the tube in an outward direction and the photon is lost.

If the photon survives to a boundary, the type of interaction, reflection or transmission, is determined based on the materials' properties, and the incident angle relative to the surface normal. Fresnel equations are used to determine the probability of reflection unless $n_1 > n_2$ and the incident angle is greater than the critical angle, in which case TIR occurs and the probability of reflection is 100%. The surfaces can be treated as specular or the angular distributions from Janecek and Moses' work can be used if the surface displays both specular and diffuse properties. If the photon is transmitted, the law of refraction determines the angle

of transmission. The photon's position and direction are updated and the process is repeated until the photon is collected in the PMT or escapes. The distance travelled by each photon is tracked and after the simulation each photon is weighted by $\omega_{att} = e^{-x/\lambda}$, where x is the path length and λ is the attenuation length of the material.

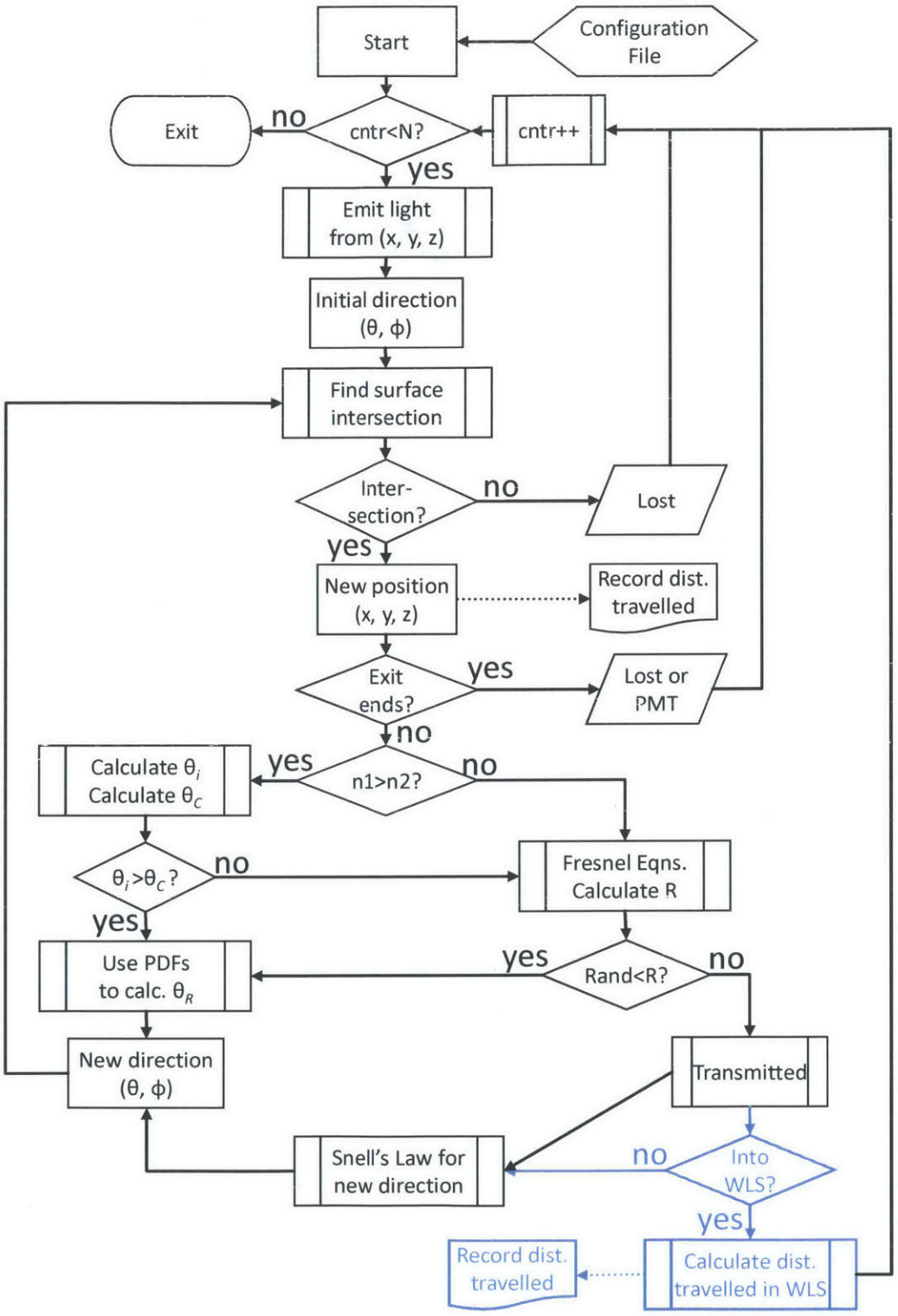

Figure 3.5. Flow diagram for light propagation model. Blue items are simulation modifications discussed in section 3.3.1.

Example photon paths in a small section of the PTFE tubing is shown in Figure 3.6. The simulated photons are isotropically created at the center of the tube, the green lines represent the photon paths and the red points are outer wall transmissions. Photons emitted at incident angles greater than the critical angle undergo diffuse reflections, which results in most photons transmitted out of the tube within a small number of wall interactions and near the point of creation. As expected, the photons emitted at incident angles less than the critical angle are immediately transmitted and lost which can be seen by the density of red points.

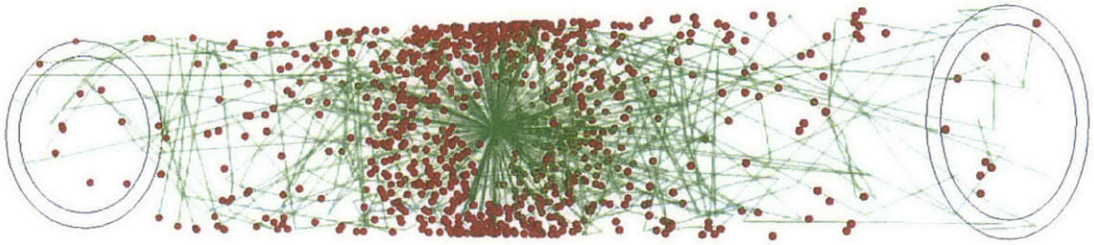

Figure 3.6. Example of photon paths in PTFE tubing from an isotropic point source located in the center of the tube. Green lines represent the photon paths and the red points are outer wall transmissions.

3.2.3. Analytical Estimation

An estimation of the signal attenuation can also be approximated by discretizing the angle θ based on the number of reflections a photon will undergo to reach the end of the PMT. In order to do so we have to assume specular reflections at the boundary between the OLS and the inner wall of the PTFE tube. The first angular group, $i = 0$, exits directly out of the tube with no reflections, $n = 0$, and is shown with a red line in Figure 3.7. This first angular group starts at $\theta_0 = 0$ (i.e., along the z-axis) and goes to an angle that subtends the opening of the tube, θ_1. The next group includes all angles in which the photon experiences one reflection before reaching the end of the tube, θ_1 to θ_2, as shown between the red and blue lines. This discretization continues until the angle is $\theta_{imax} = 90° - \theta_c$. Photons emitted at angles larger

than $90° - \theta_c$ are lost via transmission through the walls. The number and size of the angular groups varies with the distance to the PMT. Each group represents a fraction, ω_i, of the isotropic photons emitted in the positive z-direction (i.e., a fraction of 2π sr.) and is calculated as:

$$\omega_i = \Omega_i/2\pi = \left(\int_0^{2\pi} \int_{\theta_i}^{\theta_{i+1}} \sin\theta \, d\theta \, d\phi\right)/2\pi \,. \tag{3.4}$$

Photons emitted at angles $\theta < 10°$ comprise 12% of the TIR photons while photons emitted at angles $10° < \theta < 90° - \theta_c$ comprise 88% of the TIR photons.

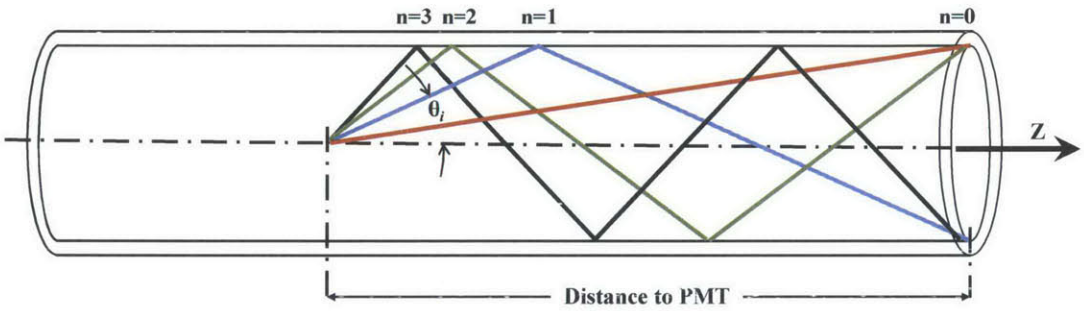

Figure 3.7. Discretization of the angle θ for an analytical approximation of signal attenuation. The angles are grouped based on the number of specular reflections, n. Photons emitted at larger θ experience more reflections before reaching the end of the tube.

We have now discretized the isotropic light based on the number of reflections and therefore can estimate the reflection losses for each group, $\rho_i = {R_i}^{n_i}$ where R_i is the reflectivity that is assumed constant for each group and n_i is the number of reflections or wall bounces. For example, assuming group 10 has a reflectivity of 95%, the reflectivity loss for group 10 is $\rho_{10} = 0.95^{10} = 0.599$. It is important to re-iterate that although group 10 will always experience 10 reflections, both $\omega_i$and ρ_i will be dependent on the distance to the PMT, i.e., position along the z-axis.

Similarly, we can estimate the attenuation loss in the OLS for each group, α_i, using an average path length for each group as a function of z, the distance to the PMT. The symmetry

of specular reflection gives $d(z,\theta) = z/\cos\theta$ independent of the number of reflections. The average path length for each group $\langle d_i(z)\rangle$ is then:

$$\langle d_i(z)\rangle = \frac{\int_0^{2\pi}\int_{\theta_i}^{\theta_{i+1}} \frac{z}{\cos\theta}\sin\theta d\theta d\phi}{\int_0^{2\pi}\int_{\theta_i}^{\theta_{i+1}}\sin\theta d\theta d\phi} = z\frac{\int_{\theta_i}^{\theta_{i+1}}\tan\theta d\theta}{\int_{\theta_i}^{\theta_{i+1}}\sin\theta d\theta}. \quad (3.5)$$

The integration in the numerator of equation 3.5 weights each path length with its corresponding solid angle and dividing by the group's total solid angle provides the average path length. Using the average path length, the attenuation loss in the OLS for each group is $\alpha_i = e^{-\langle d_i(z)\rangle/\lambda}$ where λ is the bulk attenuation length in the OLS. Although the attenuation lengths in liquid and plastic scintillators are wavelength dependent, a fixed one meter attenuation length for EJ-309 is used for all scintillation photons.[21, 36, 39-42] The losses due to reflectivity and bulk attenuation in the OLS can now be evaluated separately as a function of z and θ_i.

It is instructive to evaluate these losses for small angles, $\theta < 10°$, and large angles, $10° < \theta < 90° - \theta_c$, separately, as shown in Figure 3.8. The bulk attenuation losses for small angles and large angles are nearly equivalent due to the small differences in path length, e.g., $d(90\text{ cm}, 0°) = 90$ cm while $d(90\text{ cm},\ 90° - \theta_c) = 103$ cm. As the distance from the PMT increases, large angle photons experience a greater number of reflections and reflection losses quickly increase. Small angle photons do not experience the same increase in the number of reflections. The result, shown as "Total – Small θ" and "Total – Large θ", is that large angle photons contribute the bulk of the signal for the first 30 cm and small angle photons contribute the bulk of the signal past 50 cm. As discussed earlier, small angle photons comprise only 12% of the TIR photons and at 90 cm only 3% of the TIR photons reach the PMT.

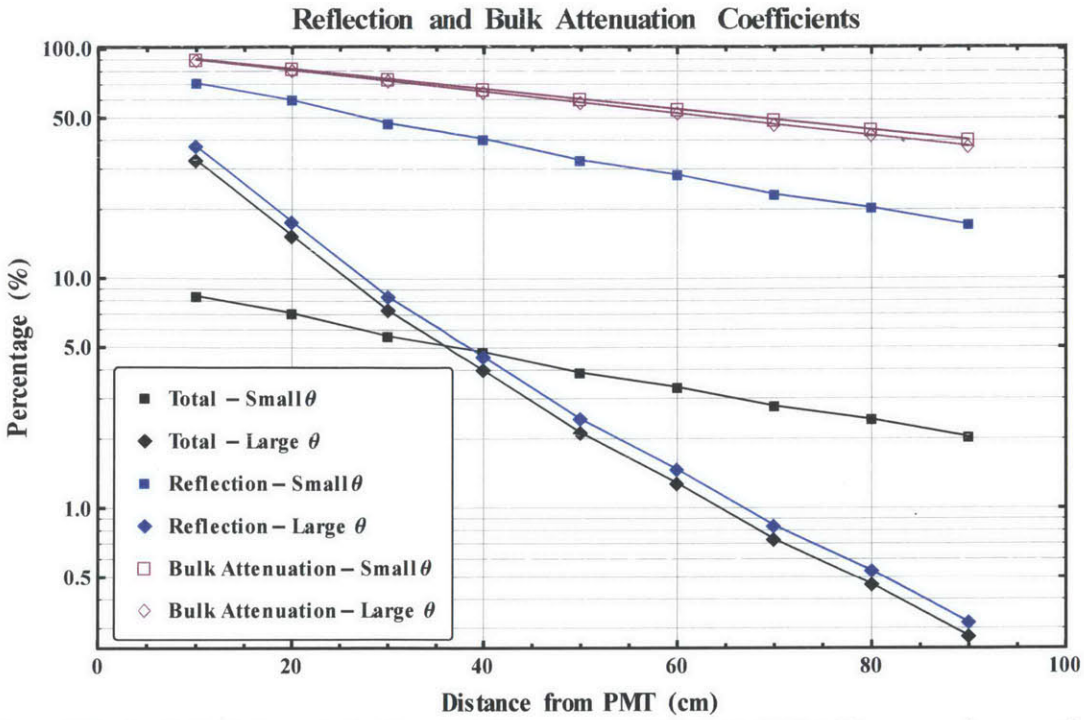

Figure 3.8. Analytical characterization of light losses in OLS filled PTFE tubing assuming specular reflections with ~90% reflectivity and a bulk attenuation length of 1 meter. Large θ photons, θ > 10°, contribute the majority of the signal for the first 30 cm while the small θ photons, θ < 10°, contribute the majority of the signal for the last 50 cm. The signal is attenuated by more than an order of magnitude within 90 cm. See text for additional information.

For a given distance from the PMT, z, the number of photoelectrons produced at the photocathode of the PMT is then $N_{pe}(z) = QE\ S_0 \sum_{i=0}^{i_{max}} \rho_i\ \alpha_i\ \omega_i$ where the quantum efficiency of the PMT is QE and S_0 is the initial number of photons created in the OLS. As discussed above, ω_i is the fraction of photons with attenuation and reflection losses α_i and ρ_i, respectively. Then one has:

$$N_{pe}(z) = QE\ S_0 \sum_{i=0}^{i_{max}-1} e^{-\langle d_i(z)\rangle/\lambda}\ R(\theta_i)^{n_i}\ \int_{\theta_i}^{\theta_{i+1}} \sin\theta\ d\theta. \qquad (3.6)$$

3.2.4. Comparing Modeled, Analytical, and Experimental Data

A one-meter long PTFE tube with an inner diameter of 5.28 mm was filled with EJ-309 and spectra from a Sr-90 beta source were measured in both left and right PMTs as the

source was positioned along the length of the tube. Optical tapers were used to seal the tubes and allow the scintillation light to enter Hamamatsu R6095 PMTs located at each end of the tube.[43] A third PMT, a Hamamatsu H8500, was used to trigger the data acquisition system.[44] The H8500 was positioned along the length of the tube opposite of the Sr-90 source as shown in Figure 3.9. The large amount of light escaping the sides of the tube provided a consistent trigger at all source positions. Although there is still a threshold effect due to the H8500, it is not dependent on the attenuation of the propagated light signal reaching the end of the tubes, either due to bulk attenuation or reflection losses.

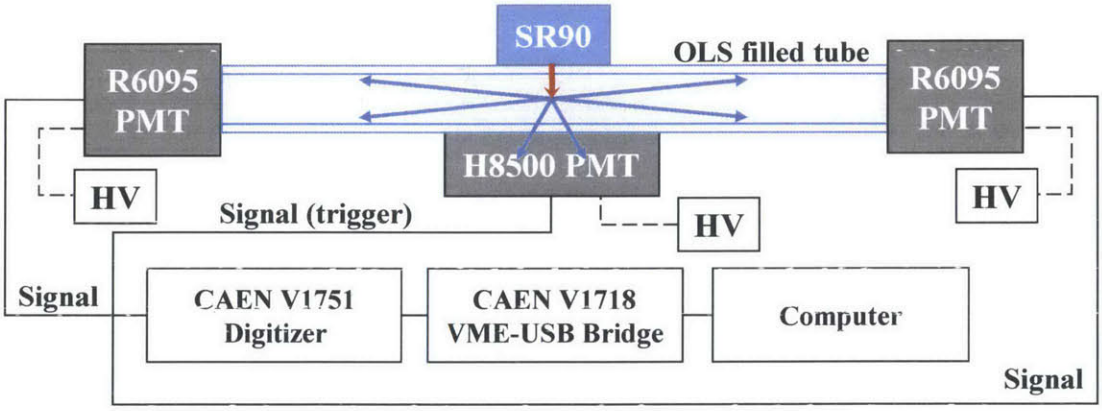

Figure 3.9. A portion of the light escaping the OLS filled PTFE tube is captured by a H8500 PMT that triggers the acquisition of the end PMTs.

The large variation in signal strength as a function of source position and the 1-volt dynamic range of the CAEN Model 1751 Digitizer required the high voltage to each PMT be varied to ensure the full spectrum at each position was collected.[45] Therefore, to compare spectra from position to position required the gain of each PMT, as a function of high voltage, be characterized. A short plastic scintillating fiber with a ^{90}Sr attached at a fixed location was used as an unchanging light source as spectra were measured at high voltages ranging from -1250 V to -1475 V. The gains observed were consistent with the manufacturer provided information. The calibrated gain as a function of high voltage for each R6095 PMT was then

used to convert the digitized pulses captured to the number of photoelectrons at the photocathode. The number of photoelectrons, N_{pe}, is calculated as:

$$N_{pe} = Q\, e^{-1}\, G^{-1} = (t \sum v_i / R)\, e^{-1}\, G^{-1} \tag{3.7}$$

Where, Q is the integrated charge, $\sum v_i$ is the sum of the voltage measurement in the pulse, t is the time interval between the digitized samples (i.e., the inverse of the digitizer's sampling rate), e is the charge of an electron, R is the digitizer input impedance (50 Ω), and G is the gain of the PMT as a function of high voltage.

Figure 3.10 shows a typical 15-minute measurement and highlights the original problem encountered in the CRI development; the poor attenuation in the OLS filled PTFE tubing. The Sr-90 source was positioned 75 cm from the left PMT along the 1-meter tube. The means of the left and right PMT signals, $(3.8 \pm 3)\ p.e.$ and $(29 \pm 16)\ p.e.$, demonstrate the significant attenuation of light occurring over the short distance of 75 cm. Of the 15,710 events triggered by the H8500 in this 15-minute measurement, more than 40% of the left PMT signals fall below a measurable cutoff while only 3% of the right PMT signals were below a measurable cutoff, demonstrating again the significant attenuation effects.

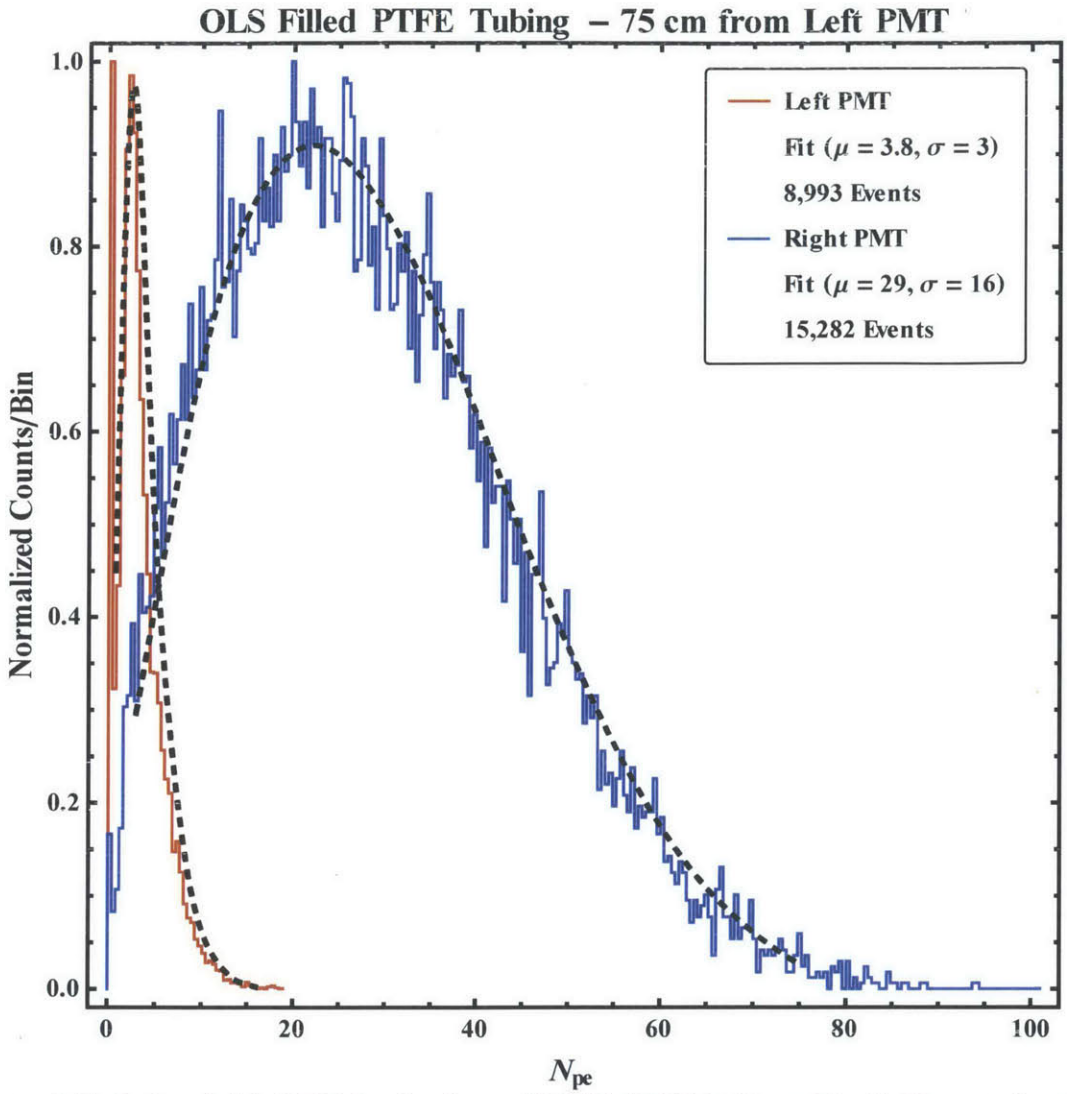

Figure 3.10. Left and right PMT signals using an OLS filled PTFE tubing with a Sr-90 source located 75 cm from the left PMT. The left PMT signal demonstrates the signals significant attenuation in just 75 cm. More than 40% of the left PMT signals fall below a measurable cutoff while only 3% of the right PMT signals were below a measurable cutoff

In general, we expect the mean of these spectra to have an exponential decrease with increased distance from the PMT. Figure 3.11 shows the measured data from the left and right PMTs compared with two modeled data sets ran with wall reflectivity of 85% and 95% and with two analytical estimations using reflectivity of 90% to 94% and 88% to 92%. All data sets show that the attenuation length is not constant along the length tube. Typical of narrow light guides, the section closest to the PMT has a small attenuation length resulting in more

than 90% signal loss in the first 50 cm. Both the modeled data and the analytical data support this being attributed to the rapid loss of the large angle signal. In the analytical calculation, photons emitted at these angles are rapidly lost due to the large number of reflections. In the model, they are lost because their reflections are determined by a more diffuse probability distribution function resulting in more transmission losses. Very few model photons undergo more than ten reflections resulting in relatively consistent reflection losses as shown with the modeled 85% and 95% reflectivity data. Overall, this provides confidence that the model is consistent with experimental results and can be used as a guide to evaluate other potential solutions.

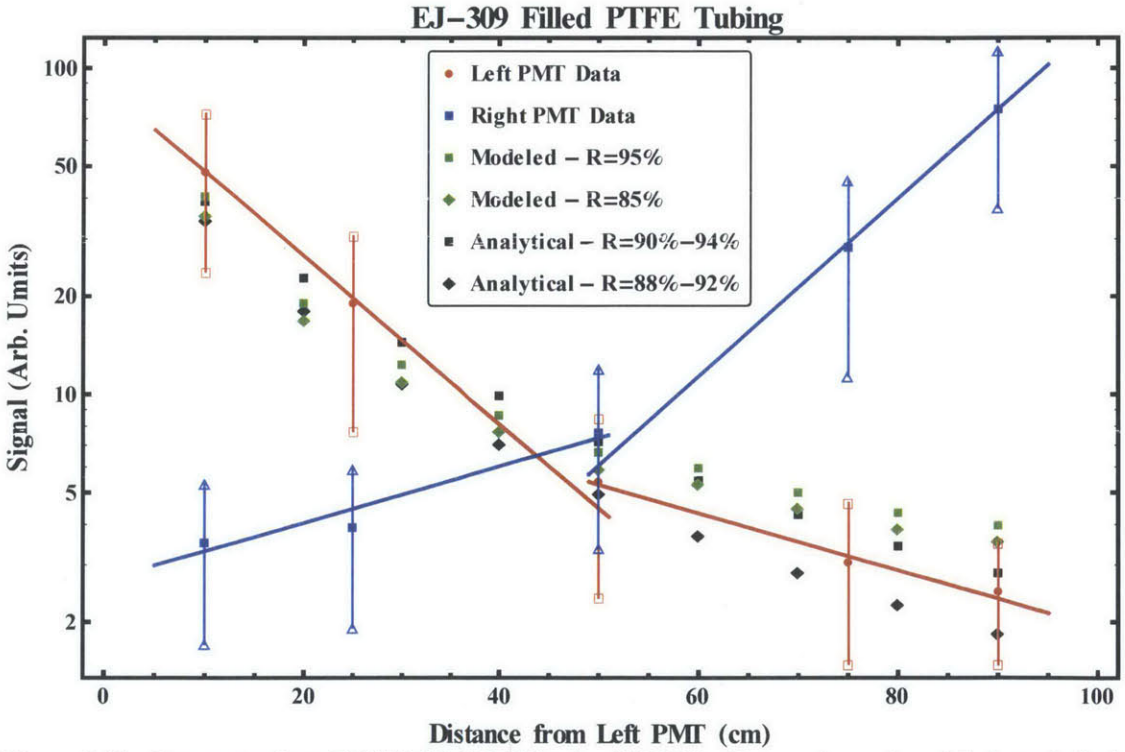

Figure 3.11. One meter long EJ-309 filled PTFE tube (4AWG). Comparison of modeled, analytical, and experimental data. The large attenuation in the first 50 cm makes reading the OLS light at the end of the tube impractical.

3.3. Modeling the Wavelength-Shifting Fiber Read-out

The poor attenuation in the OLS filled fluoropolymer tube makes direct measurements at its ends impractical at lengths over 50 cm. A potential solution is to use WLS fibers to read-out the OLS scintillation light to the PMTs. Scintillation light that enters the WLS fiber is absorbed and isotropically re-emitted at a longer wavelength. The WLS fiber then acts as a light guide and channels the re-emitted light to the PMTs. Light propagation in WLS fibers occur through the same TIR process however, in this case the reflection and bulk attenuation losses are far smaller. To estimate the expected signal from an OLS-WLS fiber coupled system the previous light propagation simulation was modified to include photon absorption in the WLS fiber.

3.3.1. Properties of Wavelength Shifting Fibers

There are many variations of WLS fibers but two primary vendors are Saint-Gobain Ceramics & Plastics Incorporated and Kuraray America, Incorporated. The majority of measurements performed in this work use 1mm and 2mm diameter BCF-91A fibers with a single cladding manufactured by Saint-Gobain.[38] Shown in Figure 3.12, these fibers consist of a polystyrene core ($n_{PS} = 1.60$) and a PMMA cladding ($n_{PMMA} = 1.49$) giving a trapping efficiency along the axis of 3.4% to approximately 7% near the core-cladding interface.

A second cladding of a fluorinated polymer ($n_{FP} = 1.42$) is an available optional for most fibers. The additional cladding improves the trapping efficiency along the axis to 5.6% but based on the configuration it may reduce the number of photons entering the WLS fiber. Figure 3.13 shows a muon creating isotropic scintillation light in the OLS along its path. Scintillation light entering the WLS fiber has a probability of being absorbed and re-emitted, P_{WLS}, equal to:

$$P_{WLS} = \left(1 - e^{-x/\ell_{MFP}(\lambda_{Inc})}\right) * \varepsilon_{RE} \tag{3.8}$$

where x is the path length of the light through the WLS fiber, $\ell_{MFP}(\lambda_{Inc})$ is the mean free path of a photon of wavelength λ_{Inc} inside the WLS fiber , and ε_{RE} is the re-emission efficiency quoted as 85% from Saint-Gobain.[46]

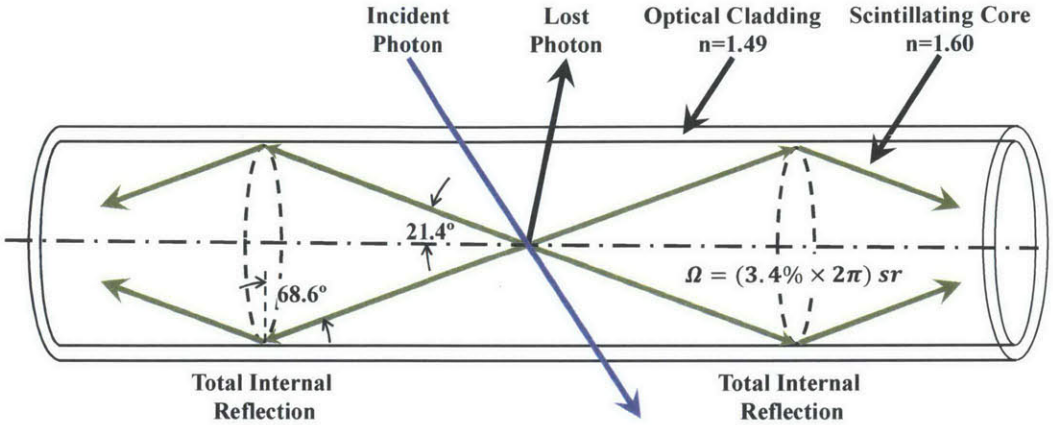

Figure 3.12. Saint-Gobain wavelength shifting fiber BCF-91A diagram.[38] Photons entering the WLS fiber can be absorbed and re-emitted isotropically at longer wavelengths. Only photons re-emitted such that their incident angle at the core-cladding interface is greater than the critical angle are channeled down the fiber.

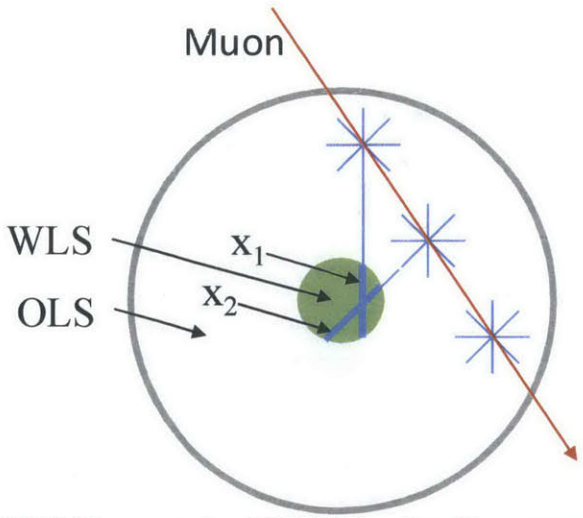

Figure 3.13. Example of WLS fiber capturing OLS light produced by a muon. As scintillation light is produced in the OLS a portion will enter the WLS fiber. The probability that the light will be absorbed depends on the path length of the light through the WLS fiber, e.g., x_1 and x_2.

The mean free path of an incident photon of wavelength λ_{inc} inside the BCF-91A fibers is shown in Figure 3.14. A 425 nm wavelength photon (the peak wavelength for many common OLS) has a mean free path of 0.21 mm inside the WLS fiber. The probability this photon will be absorbed along a 1 mm path through the WLS fiber is over 99% giving the probability of being absorbed and re-emitted, $P_{WLS} = 84.3\%$. Based on a specific OLS – WLS fiber combination, an average mean free path $\langle \ell_{MFP} \rangle$ can be calculated as

$$\langle \ell_{MFP} \rangle = \int_{\lambda_{min}}^{\lambda_{max}} \ell_{MFP}(\lambda')\, f_{inc}(\lambda')\, d\lambda' \tag{3.9}$$

where $f_{inc}(\lambda')$ is the probability distribution function describing the OLS emission spectrum and λ_{min} and λ_{max} are the minimum and maximum OLS wavelengths.

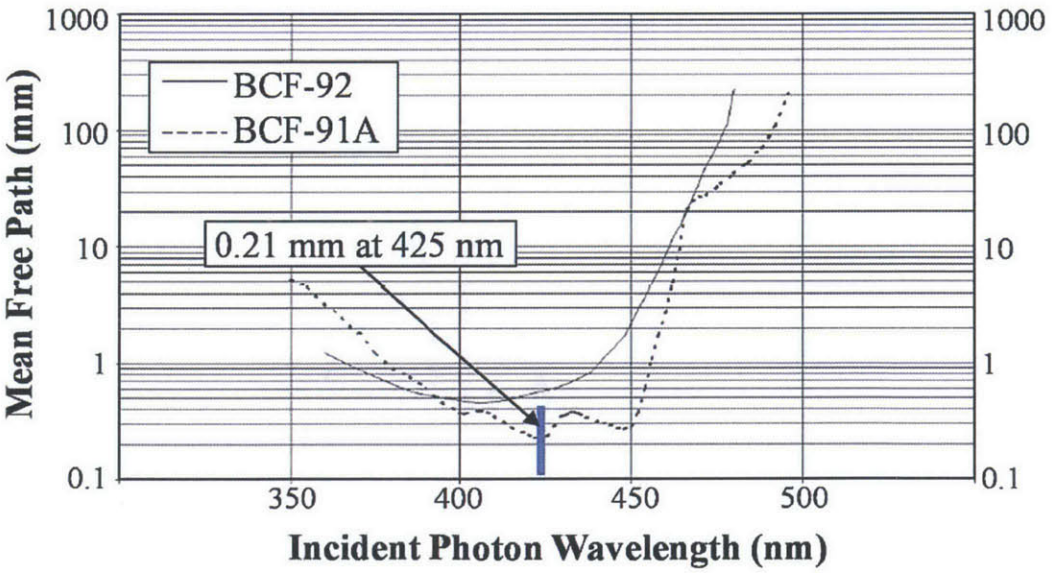

Figure 3.14. Mean Free Path in Saint-Gobain WLS fiber as a function incident photon wavelength.[46] The mean free path for a 425 nm wavelength photon, the peak wavelength for many common OLS, in the BCF91A is 0.21 mm, i.e., near the minimum mean free path as required for optimal photon absorption and re-emission.

Minimizing the average mean free path of an OLS – WLS fiber combination maximizes the probability of absorption in the WLS fiber, i.e., P_{WLS} is maximized. This also follows from the fact that the absorption spectrum in the WLS fiber is inversely related to the mean free path

in the WLS fiber, i.e., higher absorption occurs when the mean free path is smaller. The EJ-309 emission spectrum closely matches to the BCF-91A absorption spectrum as shown in Figure 3.15. Also shown is the WLS fiber emission spectrum and the small overlap with the WLS fiber absorption spectrum in the 460 nm to 470 nm region that will result in a small amount of self-absorption losses.

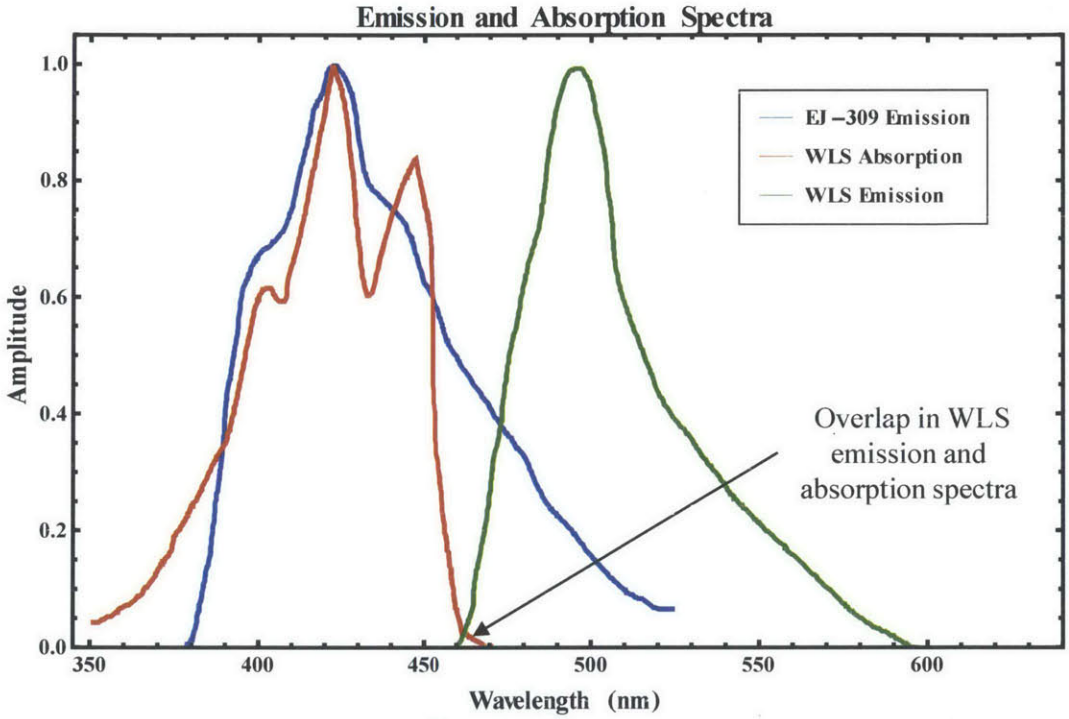

Figure 3.15. EJ-309 emission spectrum[21] and Saint-Gobain BCF-91A WLS fiber absorption and emission spectra.[38] Emission and absorption are well matched to maximize wavelength shifting. Small overlap between WLS fiber emission and absorption minimizes self-absorption.

Adjustments made to the previous light propagation model to include WLS fiber absorption are shown in Figure 3.5 highlighted in the blue. First, the path of the photon is tested to determine if it intersects the WLS fiber based upon the geometry established in the configuration file. If the photon intersects the WLS fiber, the probability of reflection is again calculated using Fresnel equations and the outer PMMA cladding is treated as specular. If the photon is transmitted into the WLS fiber, the path length from the entry point along the refracted trajectory to an exit point is calculated and the photon is absorbed in the WLS fiber.

The model does not consider the small possibility that the photon will pass through the fiber. The path length in the WLS fiber and the re-emission efficiency are used to weight the absorbed photon. If the photon is reflected at the WLS fiber interface, a new direction is calculated and the simulation continues until the photon is absorbed in the WLS fiber, escapes, or is killed.

3.3.2. Expected Light Collection Using WLS Fiber

To compare the expected WLS fiber signal to the OLS filled PTFE signal, the number of photoelectrons produced at the PMT from the WLS light can be calculated using, $N_{pe} = N_{photons}(z)\ QE$, where

$$N_{photons}(z) = \varepsilon_{Trap}\ \varepsilon_{Att}(z)\ \ (S_0\ \ \varepsilon_{WLS}\ P_{WLS}) \tag{3.10}$$

and S_0 is the initial number of photon produced in the OLS, ε_{WLS} is the probability of a photon entering the WLS, P_{WLS} is the probability of absorption and re-emission in the WLS fiber, ε_{Trap} is the trapping efficiency of the WLS fiber, and $\varepsilon_{Att}(z)$ is the attenuation of light propagating through the WLS fiber and is position dependent. As described in section 3.3.1, the modified simulation is used to estimate the probability of a photon entering the WLS fiber, ε_{WLS}, and the probability of absorption and re-emission, P_{WLS}.

A 2mm diameter WLS fiber was modeled running along the axis of the OLS filled PTFE tube. The WLS fiber is submerged in the OLS as shown in Figure 3.16. The simulation initiated 100,000 photons at various radii between the outer wall of the WLS fiber and the inner wall of the PTFE tube. As can be seen from Figure 3.13, the probability of entering the WLS fiber will vary radially. We found this was 74% near the WLS fiber outer wall and 56% near the inner wall of the PTFE tube giving a weighted average $\varepsilon_{WLS} = 0.59 \pm 0.04$. Correspondingly, the average photon path length in the WLS fiber was determined in the simulation to be (1.12 ± 0.02)mm. Assuming a mean free path for all photons to be 0.21 mm

(using the OLS emission peak wavelength of 425 nm) gives the probability that a photon entering the WLS fiber is absorbed and re-emitted to be $P_{WLS} = 0.846$. Based on EJ-309 producing 11,500 photons per 1 MeV electron, the estimated N_{pe} for a 0.5 MeVee, 1.0 MeVee and 2.2ee MeV energy loss without attenuation effects, i.e., $\varepsilon_{Att} = 1$, is 22 $p.e.$, 43 $p.e.$, and 95 $p.e.$, respectively.

Figure 3.16. Example of modeled configuration with 2mm diameter WLS inside OLS filled AWG4 PTFE tube.

A small prototype using a 2 mm diameter WLS fiber inside an EJ-309 filled PTFE tube with a 5.28 mm inner diameter was built and spectra were measured using ^{90}Sr and ^{137}Cs. In Figure 3.17, the simulated signals for a 0.5 MeVee, 1.0 MeVee and 2.2 MeVee without attenuation effects are shown as dashed lines with the ^{90}Sr and ^{137}Cs spectra. The Sr-90 betas have a maximum energy at 2.2 MeV and the Compton continuum for the 0.662 MeV Cs-137 gamma ray starts at approximate 0.5 MeV, corresponding well with the simulated values.

Our initial estimate of the number of photons produced by a muon inside the OLS was 11,000, which is close to 11,500 produced by a 1 MeV electron. Using the 1 MeV electron simulated signal the muon signal is estimated to be 41 $p.e.$ without attenuation effects. The manufacturer stated attenuation length for BCF-91A is 3.5 meters, giving the attenuated signal 2 meters from a muon interaction point approximately equal to 22 photoelectrons.[38] Assuming the PMT pulse is triangular with a width of t, i.e., the area of the pulse is $(V_{max}\ t)/2$, gives a maximum voltage of

$$V_{max} = 2\big(R \cdot N_{pe} \cdot G \cdot e\big)/t. \qquad 3.11$$

Using $N_{pe} = 22\ p.e.$, $G = 2.1 \times 10^6$, $t = 15$ ns, and $R = 50\ \Omega$ gives $V_{max} \approx 49.9$ mV, a reasonably discernable pulse. Based on these results, the WLS fiber coupled to an OLS filled fluoropolymer tube may be a viable solution for the CRI.

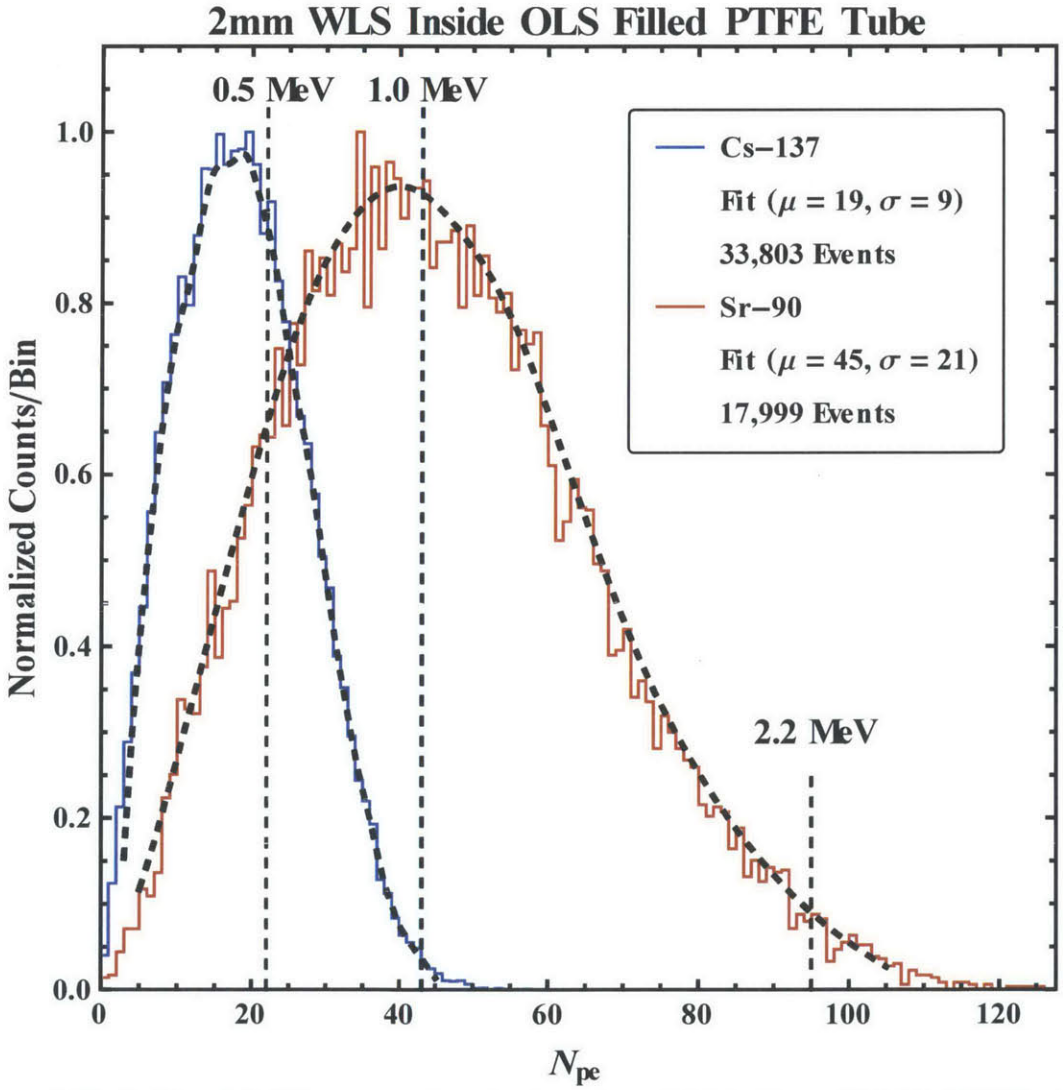

Figure 3.17. Sr-90 and Cs137 spectra collected using a 2mm WLS inside an OLS filled PTFE tube. Modeled signal for a 0.5 MeVee, 1.0 MeVee, and 2.2 MeVee, marked with dashed lines, are included for comparison.

4. Detector Module Fabrication and Testing

Before constructing the full two-meter detector modules, an optimal configuration based on available materials needed to be identified. We considered several arrangements of organic liquid scintillators (EJ-305 and EJ-309) coupled to fluoropolymer tubes (fluorinated ethylene propylene (FEP), and PTFE) of different diameter and with one or more WLS fibers inside the tube submerged or attached to the outside. The ten configurations considered are listed Table 4.1. Based on several factors, configuration number 8, with two 2mm diameter WLS fibers attached to the outside of an EJ-309 filled FEP tube, was selected. This choice is motivated by the results in the next sections. The attenuation length of a full two-meter detection module using this configuration was then characterized.

Table 4.1. Sample Detection Module Configurations Tested.

Number	OLS	WLS Fiber			Tube Mat.	Ext. Material
		Dia.	Position	Qty.		
1	EJ-309	2 mm	Internal	1	FEP	None
2	EJ-309	2 mm	Internal	1	PTFE	None
3	EJ-309	2 mm	External	1	PTFE	Teflon Tape
4	EJ-309	2 mm	External	1	FEP	Teflon Tape
5	EJ-305	2 mm	External	1	PTFE	Teflon Tape
6	EJ-305	2 mm	External	1	FEP	Teflon Tape
7	EJ-309	1 mm	External	3	FEP	Teflon Tape
8	EJ-309	2 mm	External	2	FEP	Teflon Tape
9	EJ-309	2 mm	External	2	PTFE	Teflon Tape
10	EJ-309	2 mm	External	4	FEP	Teflon Tape

4.1. Detector Module Materials

4.1.1. Choice of Organic Liquid Scintillators

Two Eljen Technologies' OLS, EJ-309 and EJ-305, were used to evaluate potential detector module configurations. Some of their physical properties are summarized in Table 4.2. The BCF-10 plastic scintillating fiber and EJ-321-H, a mineral oil based OLS, are also listed for

comparison. In order to minimize the quenching effect of dissolved oxygen, nitrogen was bubbled through the OLS before use. Also, a syringe pump and a long thin tube were used to slowly pump the OLS into the larger fluoropolymer tubing. This allowed the tubing to be filled from the bottom minimizing captured air bubbles and additional exposure to oxygen during the filling process.

Table 4.2. Physical Properties of Organic Liquid Scintillators.

Material	Photons Per 1Mev electron	Specific Gravity	Index of Ref.	PSD	Flash Point (°C/°F)	Decay Time (ns)	Att. Length (m)
EJ-305	12,000	0.893	1.505	No	45/113	2.7	>3
EJ-309	11,500	0.964	1.57	Yes	144/291	3.5	>1
EJ-321-H	7,800	0.86	1.48	No	81/178	2.0	>5
BCF-10*	8,000	1.05	1.60	No	50/122**	2.7	2.2
*Plastic scintillator data for reference **Maximum operating temperature							

EJ-305 and EJ-309 have similar scintillating properties. EJ-305's lower index of refraction is preferred for external configurations in which maximizing the transmission of light through the tubing corresponds to maximizing the ratio of the indices of refraction of the tube to the OLS, n_{tube}/n_{OLS}. EJ-305 also has a slightly better attenuation length and decay time. It is important to recall that the bulk attenuation of the OLS is not a critical property because the majority of photon losses are due to wall interactions. EJ-305 has a slightly higher photon production than EJ-309 but because of its lower density, muons will produce a few percent more photons in EJ-309 than in EJ-305. EJ-305, unlike EJ-309, does not have pulse shape discrimination capabilities, limiting its suitability for the fast neutron detection application. Its lower flash point and higher toxicity also makes EJ-305 less desirable for man-portable detection systems such as the proposed fast neutron detector.

Both EJ-305 and EJ-309 do chemically react with the polystyrene core of the WLS fiber although EJ-305 is more aggressive. In order to test the viability of the proposed read-out scheme (Figure 3.16) the end of a 2mm diameter WLS fiber sample was submerged in EJ-

309 exposing the core to the OLS. The EJ-309 slowly dissolved the core leaving only the PMMA cladding as shown in Figure 4.1. In order to test the long-term effects on the cladding and its ability to protect the polystyrene core, small samples of PMMA tubing were partially submerged in EJ-305 and EJ-309 for six months. The EJ-309 sample did not show any visible signs of an interaction and when manipulated the sample did not appear more brittle than an un-exposed sample. The EJ-305 sample showed a clear degradation in the material as shown Figure 4.2. Although it is unclear if the degradation would have resulted in a breach of the cladding a decrease in optical performance is a reasonable expectation. Based on these results, detection module designs that have WLS fiber submerged in EJ-305 are considered unviable for long-term applications. This does not preclude EJ-305 for use with external WLS fibers, as no reactions with the fluoropolymer tubes were observed.

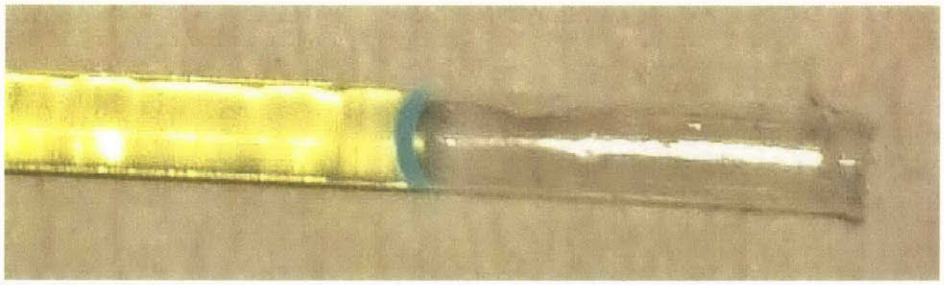

Figure 4.1. The WLS fiber polystyrene core was dissolved by EJ-309 at room temperature leaving behind the outer PMMA cladding.

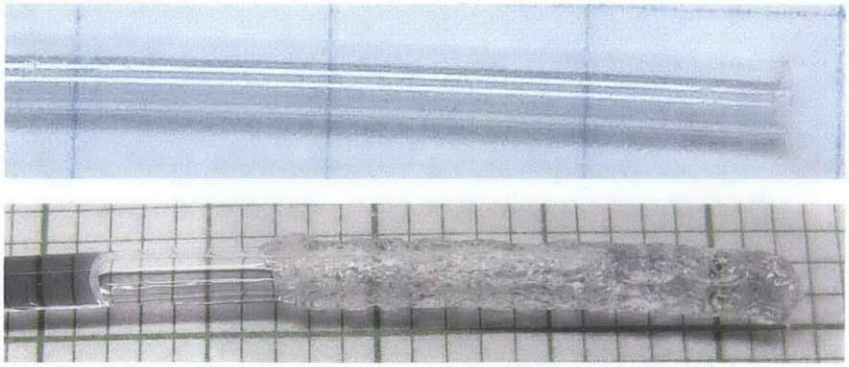

Figure 4.2. PMMA tubing before (top) and after (bottom) being submerged in EJ-305 for six months.

4.1.2. Choice of Fluoropolymer Tubes

The initial CRI concept looked for OLS-fluoropolymer tube combinations that maximized TIR, i.e., the light signal propagated along the tube. This corresponds to minimizing the ratio of the indices of refraction of the tube to the OLS, n_{tube}/n_{OLS}, and is opposite to requirements for an external WLS fiber, which are to minimize TIR in the OLS in order to collect more signal.

For internal WLS fiber configurations the tube index of refraction is less important and maximizing the ratio of the indices of refraction of the WLS fiber cladding to the OLS, $n_{WLS\ cladding}/n_{OLS}$, will improve the light transmission into the WLS fiber. In other words, light propagated along the tube favors larger n_{OLS} (e.g. EJ-309) whereas light collected with an external WLS fiber favors low n_{OLS} (e.g. EJ-305). Two fluoropolymer tubes made of PTFE and FEP were tested in various combinations with the OLS and WLS fibers. Table 4.3 summarizes the physical properties of the tubing.

Table 4.3. Physical Properties of Fluoropolymer Tubes.[47]

Tube	Name	Index of Ref.	Optical Clarity	Inside Dia. (mm)	Wall Thk. (mm)	Density (g/cm^3)
PTFE	Polytetra-fluoroethylene	1.35-1.37	Opaque	5.28 ± 0.2	0.51 ± 0.1	2.15
FEP	Fluorinated ethylene propylene	1.338	96%	5.28 ± 0.2	0.51 ± 0.1	2.20

These are common tubing materials and can be obtained in a wide range of diameters and wall thicknesses. Tests were conducted on PTFE and FEP tubing, both with a 5.28 mm inside diameter and a wall thickness of 0.51 mm, manufactured by Zeus Industrial Product, Inc. FEP has excellent optical clarity allowing for a thicker wall if durability was determined to be a concern. Although PTFE is considered an opaque material, at wall thicknesses of 0.51

mm it is translucent, allowing light produced in the OLS to be transmitted for potential absorption in an external WLS fiber.

4.1.3. Choice of Wavelength Shifting Fibers

Single-clad, BCF-91A WLS fibers with 1 mm and 2 mm diameter were ordered from Saint-Gobain and delivered on 30" diameter spools as show in Figure 4.3. Each fiber had to be cut to length and the ends sanded and polished by hand to ensure a good optical connection to the PMT. A course grit (600) sandpaper was first used to smooth the rough-cut edge followed by a fine grit (1200) sandpaper. A figure eight motion was used to minimize the surface scratches. A polishing pad was then used for the final stage. Examples of the rough-cut WLS fiber and the fully polished WLS fiber are shown in Figure 4.4. When multiple fibers are used, they are sanded and polished together as shown in Figure 4.5.

Figure 4.3. Spool of 2 mm diameter BCF-91A wavelength shifting fiber manufactured by Saint-Gobain Ceramics & Plastics, Inc.

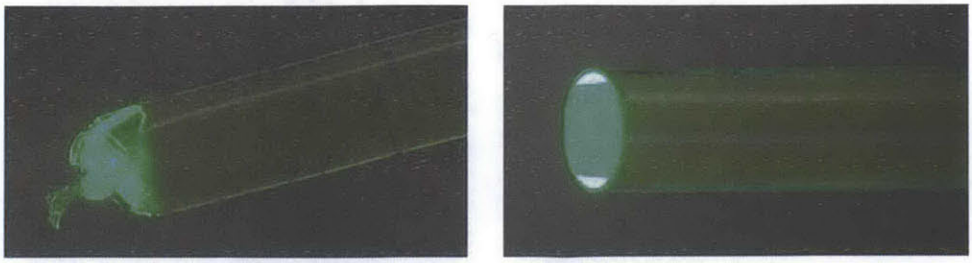

Figure 4.4. Example of WLS fiber before (left) and after (right) sanding and polishing.

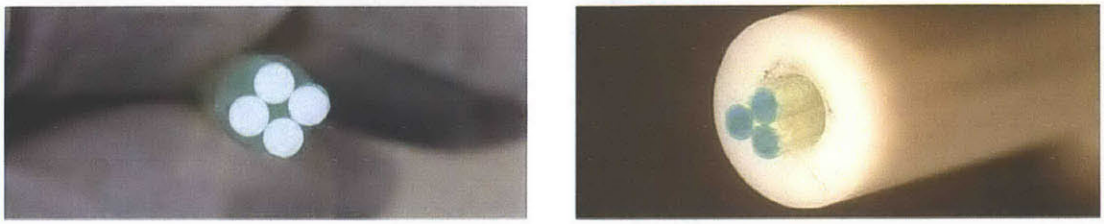

Figure 4.5. Multiple WLS fiber configurations are sanded and polished together to improve the optical connection to the PMT. A white Teflon collar (right) was used to hold the three 1 mm diameter WLS fibers together.

There are advantages and disadvantages to using single-clad versus multi-clad WLS fibers. The multi-clad WLS fibers would have better light transmission along the fiber to the PMT and be less susceptible to light losses due to damaged cladding. However, in the internal configuration, the lower refractive index of the additional cladding would reduce the light transmission into the WLS fiber reducing the amount of light to be channeled to the PMT. It is not expected that either of these effects would be significant. When ordering the WLS fiber from Saint-Gobain they were not able to produce multi-clad WLS fibers due to mechanical problems, making a comparison of the single-clad and multi-clad WLS fibers not possible.

4.2. Sample Detection Module Testing

The experimental setup used to test the sample detection modules is similar to the setup described in Chapter 3 with small modifications as shown in Figure 4.6. The Sr-90 source was

placed six inches from the end of the WLS fiber. Again, the H8500 provides a reliable trigger when the Sr-90 betas deposited energy in a small region in front of the H8500. When Teflon or aluminum tape was used as an external reflector, a 1.5 cm space, slightly wider than two H8500 pixels, was left uncovered to allow light to escape to the H8500. A CAEN V1751 digitizer was used to collect the WLS fiber and the OLS spectra from the R6095 and H8500 respectively. The areas of each digitized pulse were calculated and fit to a distribution as shown in the next section.

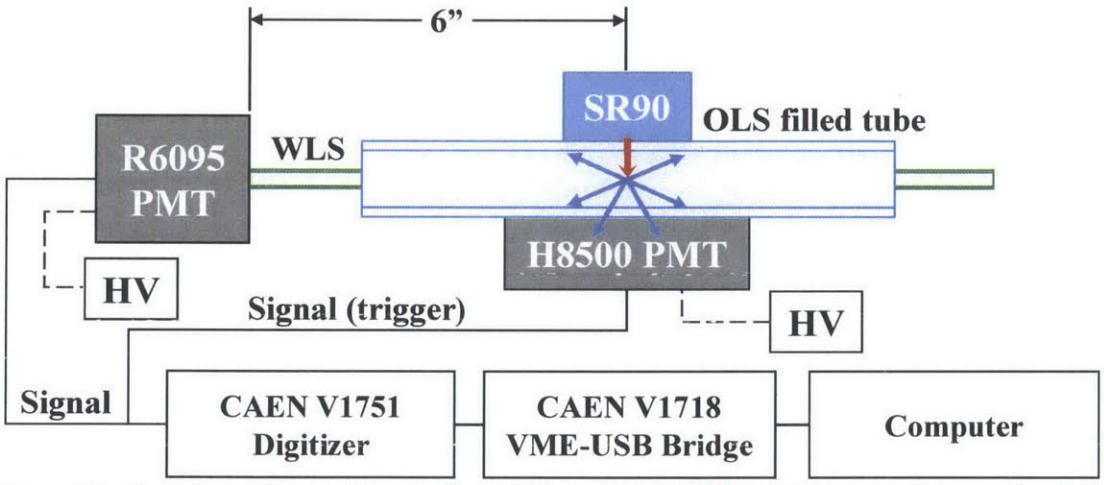

Figure 4.6. Experimental setup for sample module testing. A H8500 PMT was used to monitor light escaping the side of the OLS filled tube. In order to capture events localized at the source, only two pixels of the H8500 were used. The WLS light was captured by a R6095 PMT and recorded when the H8500 signal was above an established threshold.

4.2.1. Results for an Internal 2mm Diameter WLS Read-out

Both FEP and PTFE tubing with a 2mm diameter WLS fiber and EJ-309 were used to test the internal configuration. The WLS fibers were sealed inside each tube using a Teflon cap as shown in Figure 4.7. The cap provide a tight seal around a single WLS fiber and the inner wall of the tube. The Teflon cap functioned well for initial testing but a long-term solution for sealing the tubes around the WLS fiber was not investigated. The difficulty in machining multiple off- axis holes in the small diameter cap limited the internal configuration

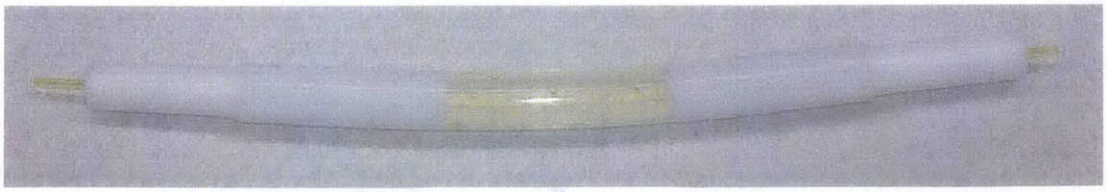

Figure 4.7. Teflon caps at each end of the fluoropolymer tube provide a seal around a single WLS fiber and the tube. Clear EJ-309 inside the tube appears yellow due to the submerged WLS fiber.

to only single WLS fiber. The spectra collected for the internal configuration are shown in Figure 4.8 and summarized in Table 4.4. The majority of the WLS fiber signal is expected to be from scintillation light entering directly from the OLS into the WLS fiber. This results in similar signals of FEP and PTFE with mean values of 93.9 ± 0.4 (arb. units) and 102.0 ± 0.4 (arb. units), respectively. The slightly higher mean of the PTFE tubing may be caused by its high reflectivity, allowing for the capture of additional photons that are lost to transmission in the FEP tubing.

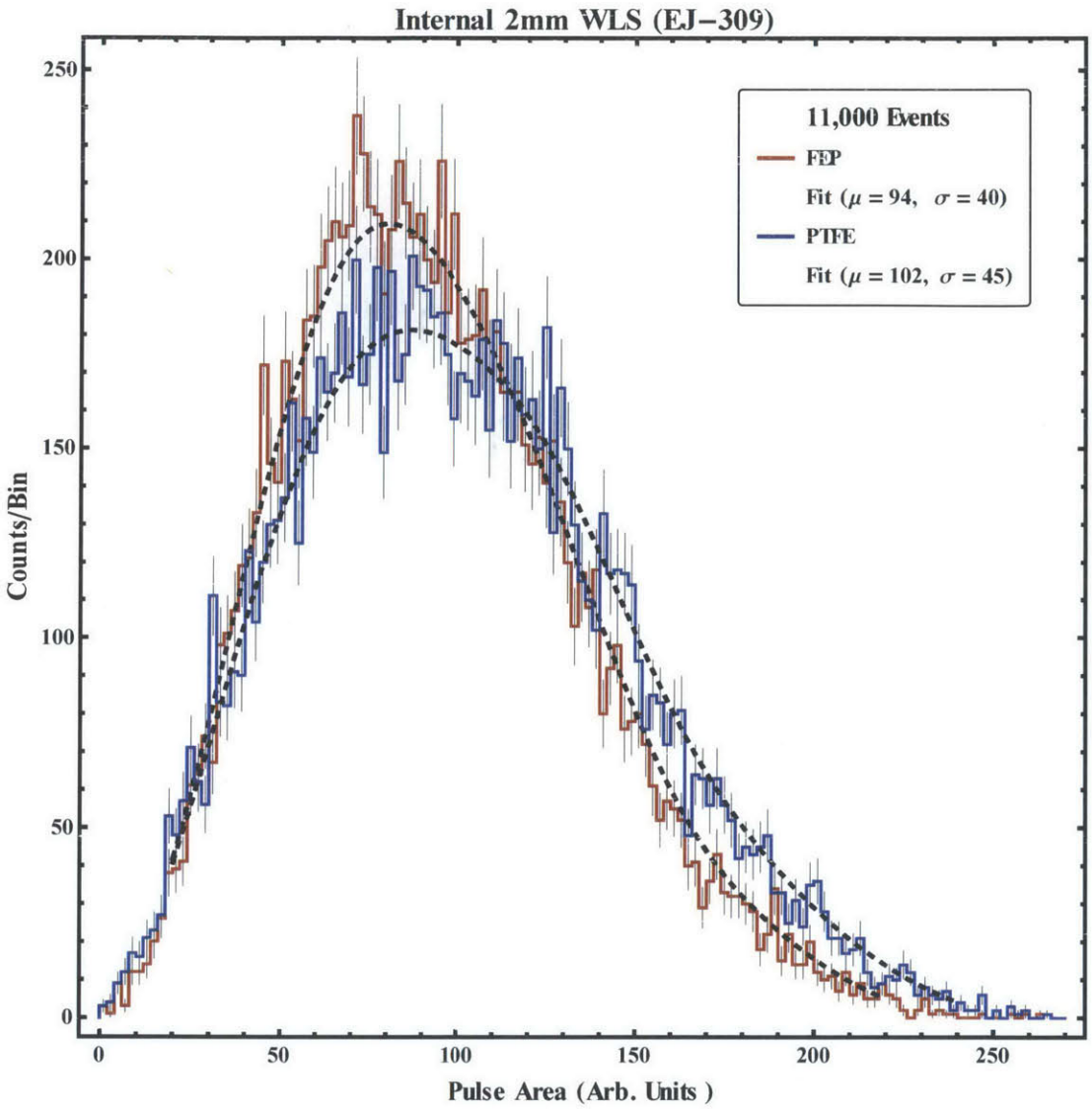

Figure 4.8. Spectra from Sr-90 using a 2mm WLS fiber inside FEP and PTFE tubing filled with EJ-309.

Table 4.4. Testing Summary of Internal Configurations with Single 2mm WLS Fiber.

Number	Mean (Arb. Units)	OLS	WLS Fiber			Tube Mat.	Ext. Material
			Dia.	Position	Qty.		
1	93.9 ± 0.4	EJ-309	2 mm	Internal	1	FEP	None
2	102.0 ± 0.4	EJ-309	2 mm	Internal	1	PTFE	None

4.2.2. Results for a Single 2mm WLS fiber – External

An alternative read-out configuration is to place one or more WLS fiber on the outside of the tubing as shown in Figure 4.9. The external configuration allows for a simpler sealing solution since the WLS fiber does not have to run through the end cap, although this geometry reduces the amount of scintillation light entering the WLS fiber. Since the WLS fiber does not come into contact with the OLS, long-term degradation of the WLS fiber is not a concern and EJ-305 can be considered. Besides the simplified sealing of the OLS inside the fluoropolymer tubes, another advantage of the external configuration is the option to increase the number of WLS fibers. This provides the ability to increase the signal strength, giving a more reliable measurement and the potential to increase further the length of the system.

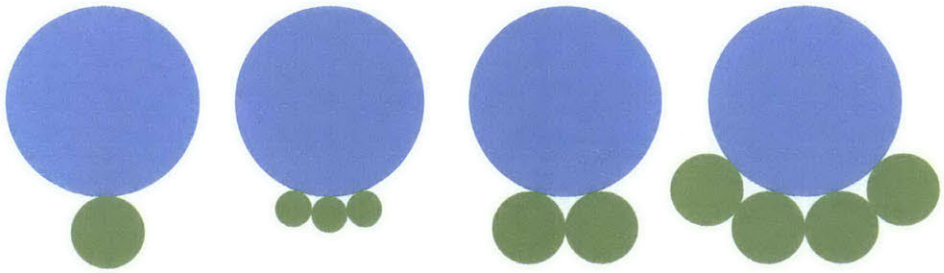

Figure 4.9. The external application of WLS fiber read-out allows for different configuration to optimize the OLS light collected.

Four combinations using a single external 2 mm diameter WLS fiber with FEP or PTFE and EJ-305 or EJ-309 were tested with a Sr-90 source. The spectra collected for the external configuration are shown in Figure 4.10 and summarized in Table 4.5. The external configuration signals are approximately 1/3 of the internal configuration signals seen in Figure 4.8. The ^{90}Sr beta particles immediately start losing energy and producing scintillation light upon entering the OLS. The internal WLS fiber, in closer proximity to the source than the external WLS fiber, subtends a larger fraction of the isotropic scintillation light resulting in the larger signals measured. The spatial distribution of the scintillation light, i.e., the type of

incident radiation, relative to the location of the WLS fibers will affect the magnitude of the signals collected for the internal versus external configurations.

Overall, the data shows all external configurations tested to be nearly equivalent. Many competing factors contribute to the measured mean, such as the quantity and spatial distribution of the scintillation light produced in each OLS, the clarity of the fluoropolymer tube, and the critical angle at the OLS-tube interface. A surprising result is the minimal affect PTFE's opacity has on allowing light to reach the external WLS fiber. As mentioned early, at a wall thickness of 0.51 mm, PTFE is translucent. As the wall thickness increases, it becomes more opaque. If thicker walls were required for mechanical integrity, the signal from the external configuration with PTFE would be reduced and potentially become an unviable option. A slightly higher mean was observed in the PTFE/EJ-305 combination, 38.0 ± 0.2 (arb. units), over the FEP/EJ-309 combination, 35.9 ± 0.2 (arb. units). It is judged that this small advantage in favor of EJ-305 does not justify the additional issues due to its low flash point and higher toxicity. Therefore, the following external configurations with multiple WLS fibers are conducted only with the EJ-309.

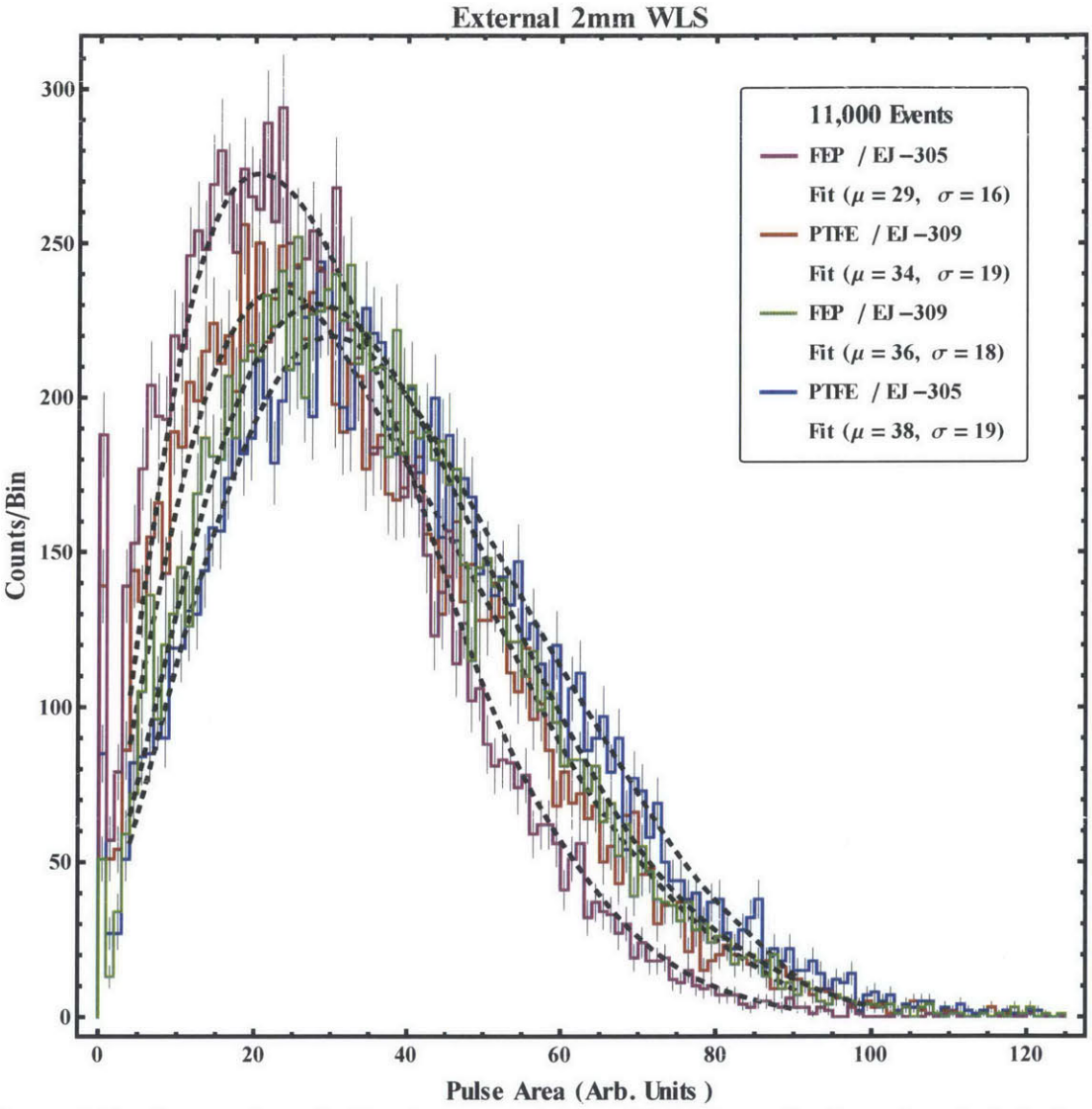

Figure 4.10. Spectra from Sr-90 using external 2mm WLS fiber. Configurations include four combinations of AWG4 FEP and PTFE tubing with EJ-305 and EJ-309. Note that the optical clarity of FEP (96% transparent) compared to PTFE(opaque) does not appear to be a critical factor at the 0.51 mm wall thickness. The external configuration signals are approximately 1/3 of the internal configuration signals seen in Figure 4.8.

Table 4.5. Testing Summary of External Configurations with Single 2mm diameter WLS Fiber.

Number	Mean (Arb. Units)	OLS	WLS Fiber			Tube Mat.	Ext. Material
			Dia.	Position	Qty.		
3	33.5 ± 0.2	EJ-309	2 mm	External	1	PTFE	Teflon Tape
4	35.9 ± 0.2	EJ-309	2 mm	External	1	FEP	Teflon Tape
5	38.0 ± 0.2	EJ-305	2 mm	External	1	PTFE	Teflon Tape
6	29.2 ± 0.2	EJ-305	2 mm	External	1	FEP	Teflon Tape

4.2.3. Results for Multiple WLS Fiber – External

Three multiple WLS fiber configurations shown in Figure 4.9 were tested using EJ-309 and FEP tubing. The four 2 mm diameter WLS fiber configuration was also testes using PTFE tubing. In this initial testing, only configurations with the WLS fibers adjacent to each other were used. This allowed for a more consistent placement of the WLS fiber along the tube. As previously discussed, the type of radiation being measured will affect the optimal positioning of the external WLS fibers. The final placement of external WLS fibers should be carefully planned to maximize the scintillation light collected, minimize the loss of active detection volume in the system and to efficiently route the multiple WLS fibers to the PMT. The WLS fibers were held against the tubing using Teflon tape while leaving a 1.5 cm space for light to reach the H8500 PMT.

The spectra collected for the multiple WLS fiber external configurations are shown in Figure 4.11 and summarized in Table 4.6. Based on the single 2mm diameter WLS fiber measurement the double and quadruple configurations are expected to be approximately 70 and 140 arbitrary units, respectively. The 2 x 2mm (FEP) mean is 57.6 ± 0.3 (arb. units), the 4 x 2mm (PTFE) mean is 133.3 ± 0.6 (arb. units), and the 4 x 2mm (FEP) mean is 136.9 ± 0.6 (arb. units). Although slightly lower than expected, they are in good agreement with the expected linear increase. The last configuration uses three 1mm diameter WLS fibers with FEP tubing. The 3 x 1mm (FEP) mean, 57.0 ± 0.3 (arb. units), is very similar to the 2 x 2mm (FEP) measurement. Using the 3 x 1mm (FEP) instead of the 2 x 2mm (FEP) provides a volume per meter reduction of over 60% with a cost reduction of approximately 50%. Although these are clear advantages, the attenuation length is typically poorer for small diameter fibers.

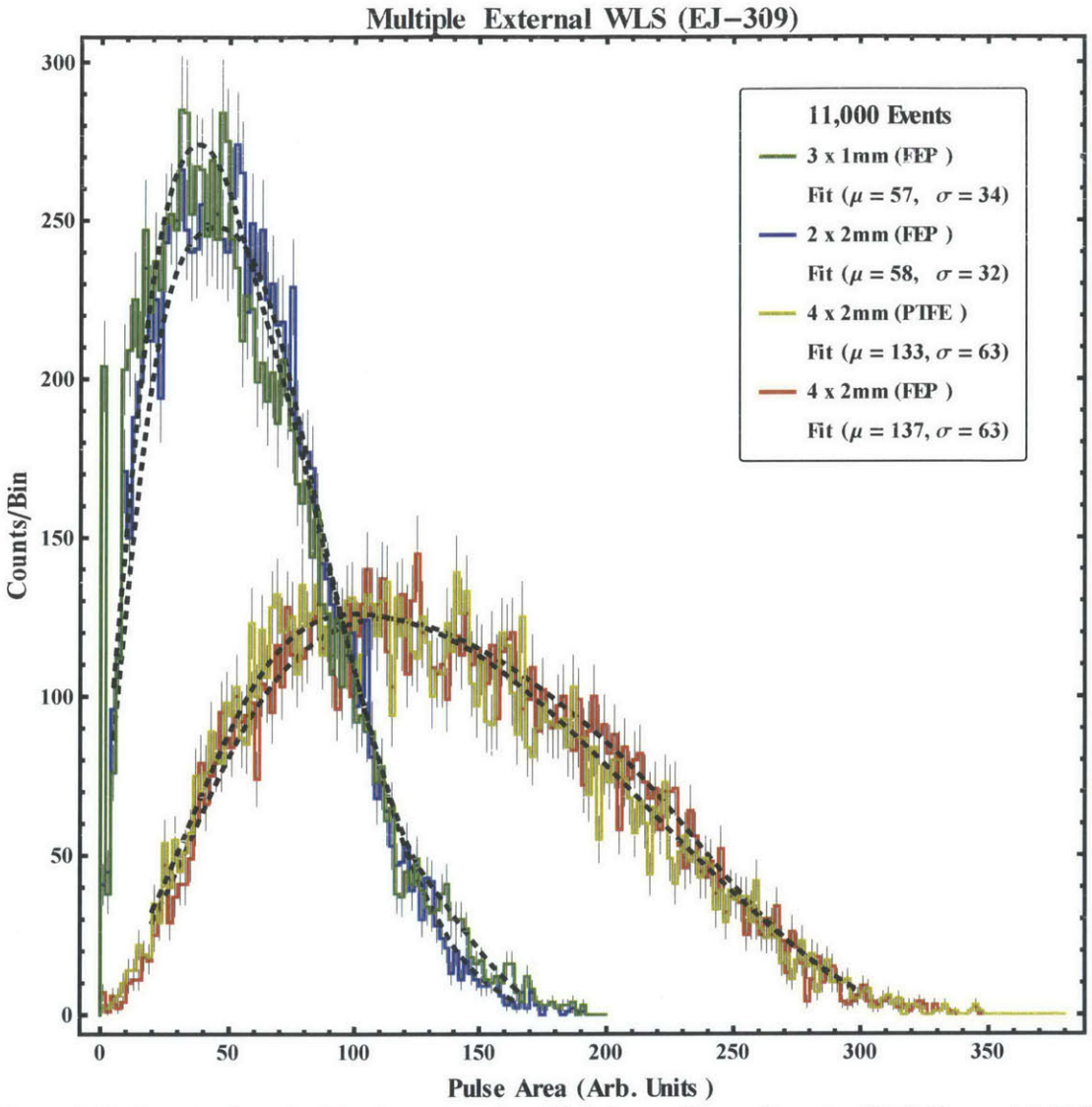

Figure 4.11. Spectra from Sr-90 using external multiple 1m and 2mm diameter WLS fibers with FEP and PTFE tubing filled with EJ-309. The external configuration provides the ability to increase the number of WLS fibers with the potential to increase further the length of the module.

Table 4.6. Testing Summary of External Configurations with Multiple 1mm and 2mm Diameter WLS Fibers.

Number	Mean (Arb. Units)	OLS	WLS Fibers			Tube Mat.	Ext. Material
			Dia.	Position	Qty.		
7	57.0 ± 0.3	EJ-309	1 mm	External	3	FEP	Teflon Tape
8	57.6 ± 0.3	EJ-309	2 mm	External	2	FEP	Teflon Tape
9	133.3 ± 0.6	EJ-309	2 mm	External	4	PTFE	Teflon Tape
10	136.9 ± 0.6	EJ-309	2 mm	External	4	FEP	Teflon Tape

4.3. Module Testing Summary

Although the signal measured with a single 2mm diameter WLS inside the OLS is approximately three times the signal from the same fiber located outside of the OLS, the challenge of creating a long-term, leak-proof cap makes it a problematic solution. By using multiple WLS fibers in the external configuration, at the expense of occupying limited space with inactive detection material and increased costs, larger signals can be produced with less complicated sealing requirements. For example, the four 2 mm diameter WLS fiber with FEP tubing and EJ-309 produced a 30% larger signal than the internal WLS fiber configuration.

EJ-309's pulse shape discrimination capability, higher flash point, and lower chemical toxicity outweighed the slightly superior signal measured with EJ-305. Although there was no consistent data suggesting the signal from PTFE or FEP outperformed the other, the potential to use thicker walls or to develop transparent custom drawn tubes that can hold the OLS and WLS fibers without the need to assemble makes FEP the logical option. Based on these findings the initial 2 meter detection module will consist of two 2mm diameter WLS fibers attached to the outside of an EJ-309 filled FEP tube.

4.4. Individual Detector Module Testing

In order to test the 2 meter long detection module, a lightproof container was assembled. Testing was conducted in the same manner as the small modules, using a H8500 PMT to trigger the pulse collection, with the addition of a second R6095 PMT in order to measure the signal at each end of the WLS fibers. The testing setup is shown in Figure 4.12. Using a Sr-90 source, digitized pulses from the left and right PMTs were collected at nine source locations, every 20 cm, along the module. The mean and standard deviation of each pulse area spectra were calculated and are shown in Figure 4.13 with the 1-meter OLS filled

PTFE results for comparison. As was seen with the attenuation of the OLS fiiled PTFE tube, the attenuation length is not constant along the length of the module. The initial 80 cm to 100 cm can be characterized with an attenuation length $\lambda = 0.8 \pm 0.1\ m$. Almost 30% of the signal remains after one meter as compared to the less than 5% remaining after one meter in the OLS filled PTFE tubing. The last 100 cm has an approximate attenuation length of $\lambda = 2.8 \pm 0.7\ m$. This results in 20% of the signal remaining after traveling the full two-meter length of the module. This is half of the expected signal based on the manufacturer stated attenuation length of 3.5 meters. In following chapter, the effects of this attenuation on the module's muon detection rates will be evaluated.

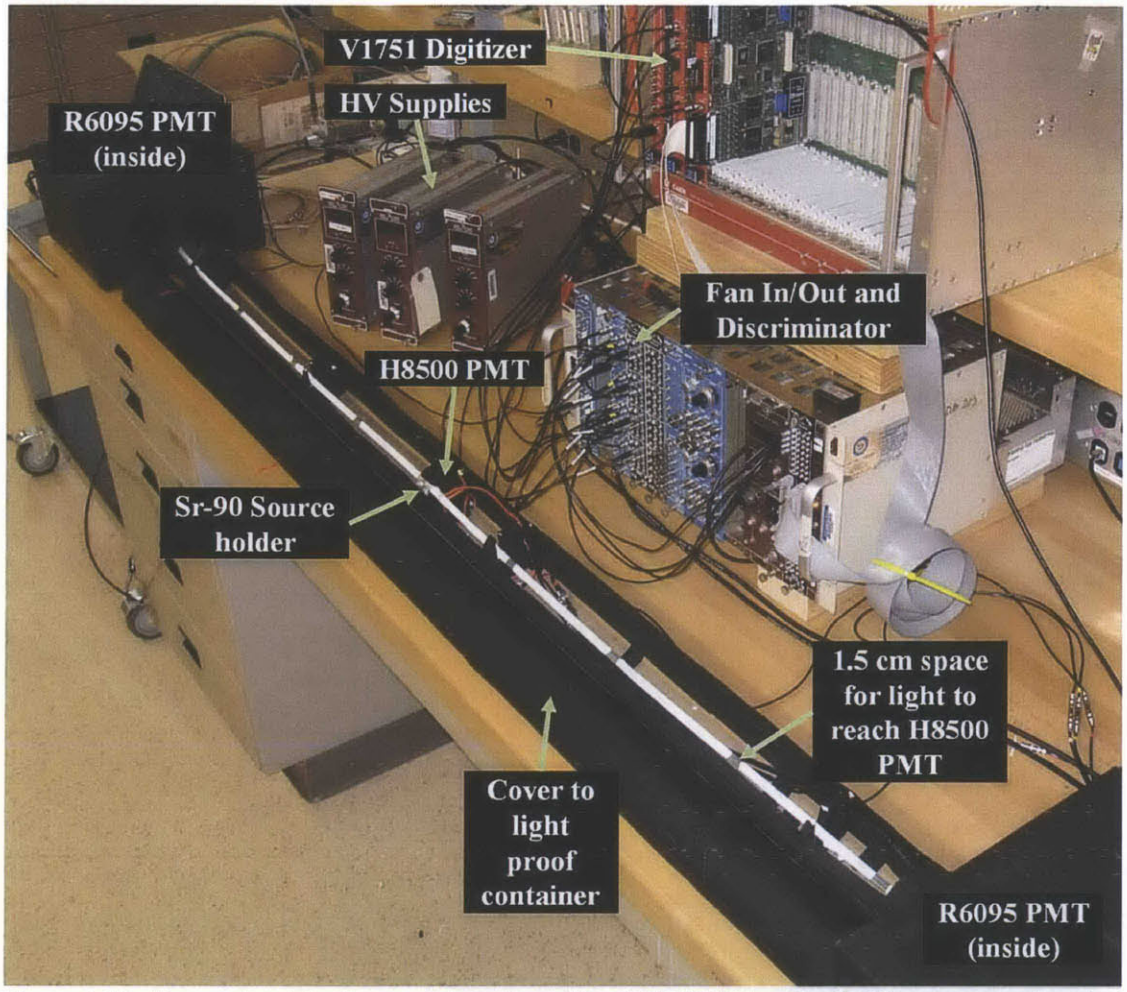

Figure 4.12. Two-meter detection module testing. The H8500 PMT and a Sr-90 source are placed at the 1.5 cm openings in the white Teflon tape which are positioned every 20 cm along the detection module. High voltage supplies provide separate bias to the H8500 and two R6095 PMTs located in dark boxes at each end of the module. Signals from each PMT are connected to a Fan in/out module and then connected to the CAEN V1751 digitizer.

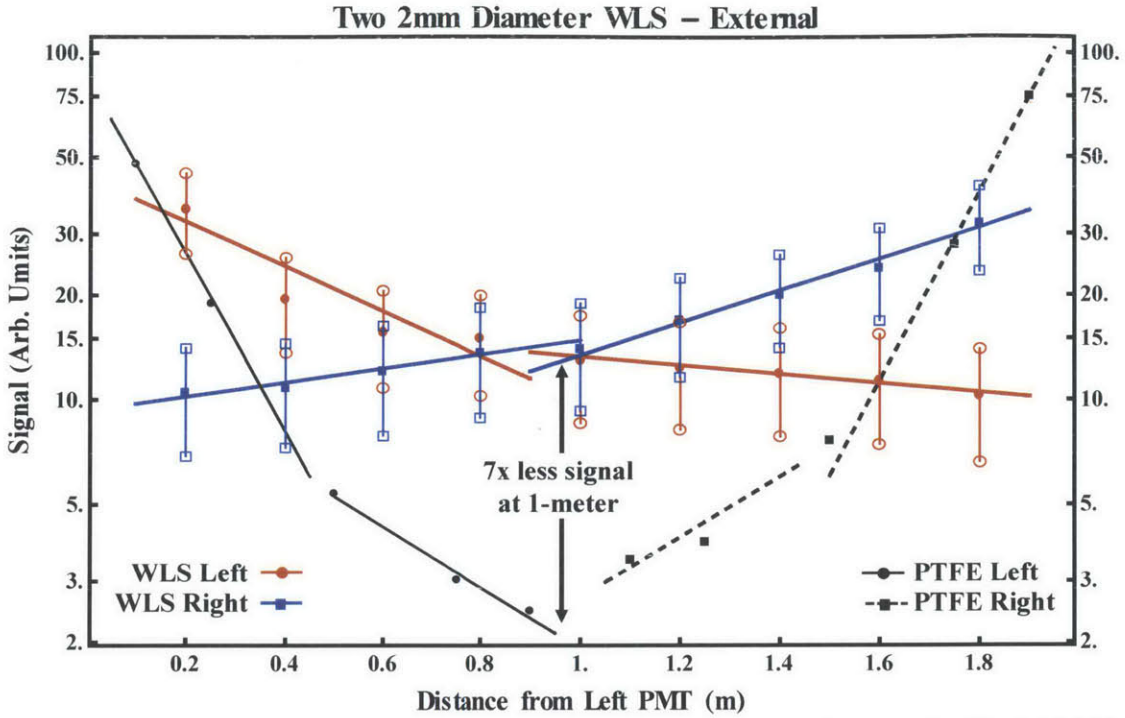

Figure 4.13. Attenuation length determination for a two-meter long detection module. The initial 80-100 cm can be characterized with an attenuation length of $\lambda_1 = 0.8 \pm 0.1$ m and the final 100 cm can be characterized with an attenuation length of $\lambda_2 = 2.8 \pm 0.7$ m. Previous data from OLS filled PTFE, shown in black, has 7 times less signal at 1-meter.

5. Detecting Muons

As stated at the beginning, the alternative detection module for the cosmic ray imaging system should operate at a continuous length of at least two meters with comparable muon detection efficiency to the current plastic fibers. In addition, having the ability to provide interaction position along the module would be beneficial.

In chapter 4, initial experiments identified the two 2mm diameter WLS fibers attached to an EJ-309 filled FEP tube configuration as a potential alternative to the current plastic fibers. In this chapter, the module's muon detection capabilities are characterized and compared to a plastic fiber. The experiments conducted demonstrate that the module's muon detection efficiency matches or exceeds that of the plastic fiber; the muon detection efficiency is uniform at all positions along the 2-meter module with the potential for increased length; and pulse timing information can be used to determine coarsely the interaction position.

5.1. Detection Module's Muon Efficiency Compared to Plastic Fibers

5.1.1. Experimental Setup

In order to compare the muon detection efficiency of the OLS module read-out by two 2mm diameter WLS fibers with that of a conventional plastic fiber a 1" x 1" x 4" plastic scintillator, i.e., trigger, was placed below the OLS module and plastic fiber as shown in Figure 5.1. Coincident events with the trigger and the OLS module or the plastic fiber are collected as muon events. Typically, a second trigger scintillator is used and only events in triple coincidence, i.e., events in both triggers and either the OLS module or the plastic fiber, are collected as muon events. A second trigger scintillator could not be used because of spatial constraints inside the lightproof container. In our setup, the 1" x 1" x 4" plastic scintillator triggered the collection of the OLS module and plastic fiber signals in the V1751 digitizer and

coincident events with the trigger were extracted in post-processing. R6095 PMTs, operating at -1200 V, were used to collect the light from the OLS module and the plastic fiber.

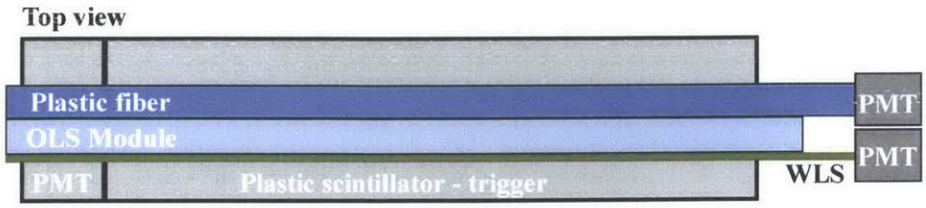

Figure 5.1. OLS module versus plastic fiber muon detection efficiency experimental setup. All plastic scintillator (1" x 1" x 4") events above 200 mV triggered the collection of the OLS module and plastic fiber signal. All OLS module and plastic fiber events above 30 mV were counted as muon events.

5.1.2. Results

Data was collected for more than 24 hours and the pulse height spectra of the OLS module and plastic fiber are shown in Figure 5.2. With no background suppression of the trigger, i.e., no second trigger scintillator, over 140,000 events were collected. The majority of these events were not coincident with either the OLS module or the plastic fiber resulting in over 120,000 events in each of their pedestals. Since their PMTs were operated at the same high voltage, the large light signal of the plastic fiber resulted in a saturated pulse height spectrum. Generally, this would increase low energy noise in the spectrum but it is suppressed by the coincident requirement. This is similar to the actual CRI design since we require hits in at least four fibers for a valid muon event, which results in excellent background suppression. The spectra show a clear detection cutoff at 30 mV giving $11{,}900 \pm 100$ coincident OLS module counts and $7{,}720 \pm 90$ coincident plastic fiber counts. Table 5.1 shows a summary of the detectors' dimensions and the data collected. Although the muon distribution complicates the efficiency comparison of non-geometrically identical detectors, detection rates per area are determined to compare the OLS module to the plastic fiber.

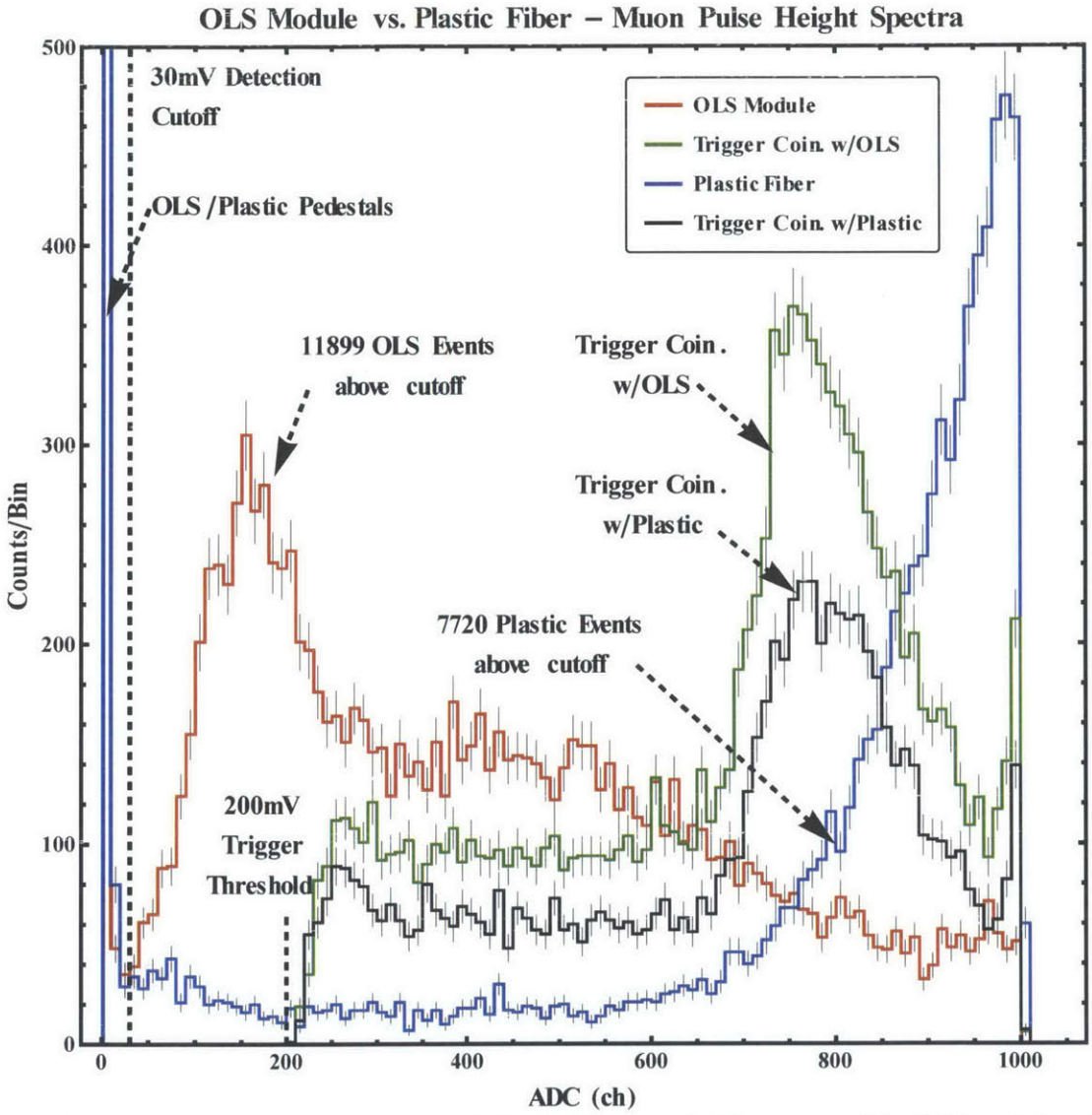

Figure 5.2. Comparison of OLS module and plastic fiber pulse height spectra. The OLS module and plastic fiber signals were collected when a large rectangular scintillator (trigger) measured an event above ~200 mV. Of the 140,000 triggered events, less than 20,000 were coincident with OLS module or plastic fiber signals over 30 mV.

Table 5.1. Muon Detection Efficiency Comparison Data.

Detector	Outer Diameter (cm)	Length (cm)	Coincident Counts (x1000)	Count rate per area (min^{-1} cm^{-2})
Module (SW)	0.63 ± 0.05	10.2 ± 0.6	11.9 ± 0.1	1.17 ± 0.1
Plastic Fiber	0.50 ± 0.02	10.2 ± 0.6	7.72 ± 0.09	0.96 ± 0.07
SW-standard wall (0.051 ± 0.01) cm				

The module used FEP tubing with a 5.28 mm inner diameter and a wall thickness of 0.51 mm, while the plastic fiber had an inner diameter of 4.85 mm and a cladding thickness of 0.15 mm. Without considering the area of the WLS fibers, the OLS module detected 1.2 ± 0.1 muons·min^{-1}·cm^{-2} while the plastic fiber detected 0.96 ± 0.07 muons·min^{-1}·cm^{-2}. This is essentially 100% detection of the expected ~1 muons·min^{-1}·cm^{-2} fluence at sea level. The FEP tubing is also available in wall thicknesses of 0.38 mm and 0.25 mm which should increase the module's count detection rate to as high as 1.28 ± 0.1 muons·min^{-1}·cm^{-2}. Although the dimensions of the two 2mm diameter WLS fibers were not included, it is expected that the fluoropolymer tube dimensions will determine the percentage of active detection volume and the WLS fibers will primarily occupy exiting voids between the tubes, i.e., the WLS fibers will not significantly reduce the active detection area. Based on these results, a system using OLS modules read-out by two 2mm diameter WLS fibers would match or improve the detection efficiency of the current plastic fiber based system.

5.2. Evaluating the Full-Length Response of the Detection Module

5.2.1. Experimental Setup

The OLS module's response is characterized as a function of position to evaluate the loss of detection efficiency due to the WLS fiber capture and transmission efficiencies. The evaluation uses the same experimental setup shown in Figure 4.12 with the signal processing

shown Figure 5.3. The H8500 was placed at five positions along the module to identify when an interaction occurred at that position and to trigger the collection of the left and right PMT signals in the V1751 digitizer. Only two pixels of the H8500 are used in order to limit the region in which events are detected.

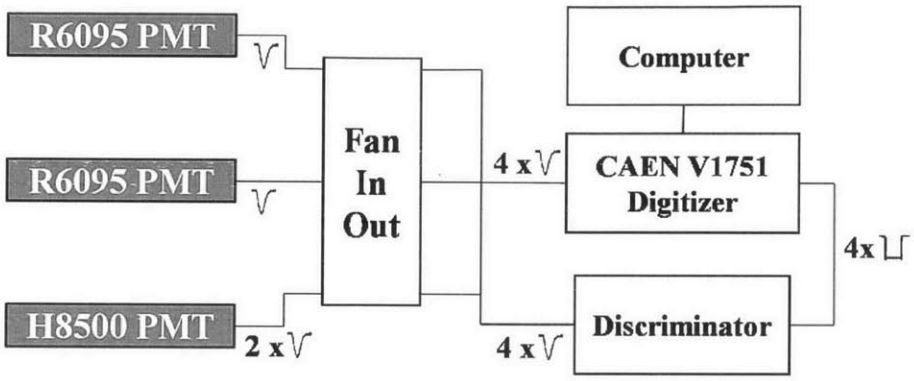

Figure 5.3. Signal processing for characterizing the detection module response to muons.

The rate of muons passing through this 1.5 cm long by 0.528 mm wide area is approximately 0.013 Hz. A 40 mV trigger threshold established a lower limit of OLS scintillation light that must be present to trigger the digitizer, i.e. to evaluate the subsequent capture and transmission in the WLS fiber. Our trigger did not prevent the contributions from gamma ray and neutron background radiation. With the relatively high trigger rates measured, approximately 0.06 Hz, and the expectation that muon events generally produce more scintillation light in the OLS, it is reasonable to predict that all muon events are captured usingthis 40 mV threshold. The PMT signals are first sent to a fan in-out module allowing the signals to be routed to the digitizer and a discriminator. The discriminator's square pulses are also sent to the digitizer to provide timing information, which will be discussed in section 0. Unlike the attenuation length characterization in section 4.4 that varied the high voltage to capture pulse height information, the high voltage supplies for the left and right PMTs are maintained at -1475 V for all measurements. This results in saturation of some pulses, which does not affect detection efficiency but destroys pulse height information.

5.2.2. Results

Data was collected at 20 cm, 60 cm, 100 cm, 140 cm, and 180 cm from the left PMT and each collection was run for more than twenty hours. The measured triggering rates at each position are 0.062 Hz, 0.061 Hz, 0.061 Hz, 0.059 Hz, and 0.056 Hz, respectively. Pulse height spectra from the left PMT, right PMT, and both channels of the triggering PMT, for each position along the module, are shown in Figure 5.4 through Figure 5.8. The H8500 PMT shows standard, self-triggered muon/background spectra with a gradual increase in counts toward lower energies and a rapid drop at its threshold. The consistent triggering rates and the typical H8500 PMT pulse height spectra, we are confident that the WLS fibers are being exposed to the same distribution of OLS light pulses at each position and there are no anomalies between datasets.

At the center position, Figure 5.6, the right PMT spectra shows a slightly higher gain that has been typical of this PMT. As the triggering PMT is moved left or right, the pulse height spectra shift as expected. Based on the data, a 40 mV detection cutoff can be used to determine if an event is detected in the OLS module. Assuming the H8500 detects and triggers on 100% of the true events, coincident events in the left and right PMTs are considered a positive detection. If a single PMT is above the cutoff, the event is detected but with a lower reliability. If neither PMT signal is above the cutoff, the module did not detect the event. The percentage of triggered events in which both left and right PMTs are above the cutoff, are from left to right, 95.6%, 95.2%, 95.5%, 95.7%, and 95.2%. The average positive detection rate is $(95.4 \pm 0.1)\%$ and including single PMT detections the rate is $(99.68 \pm 0.06)\%$. Since these events include lower light yield background events, it is reasonable to expect better performance when only measuring higher light yield muons. If only events above 300 mV in the H8500 are considered, the percentage of triggered events in which both left and right PMTs

are above the cutoff increase to, from left to right, 97.9%, 98.6%, 98.9%, 98.7%, and 98.2%. The average positive detection rate at this threshold is $(98.4 \pm 0.5)\%$. Overall, the module demonstrated a continuous detection capability along the full length of the 2-meter module with less than 5% losses due to attenuation. The increased signals measured in section 4.2.3 with additional external WLS fibers also demonstrate the potential to increase the module's length.

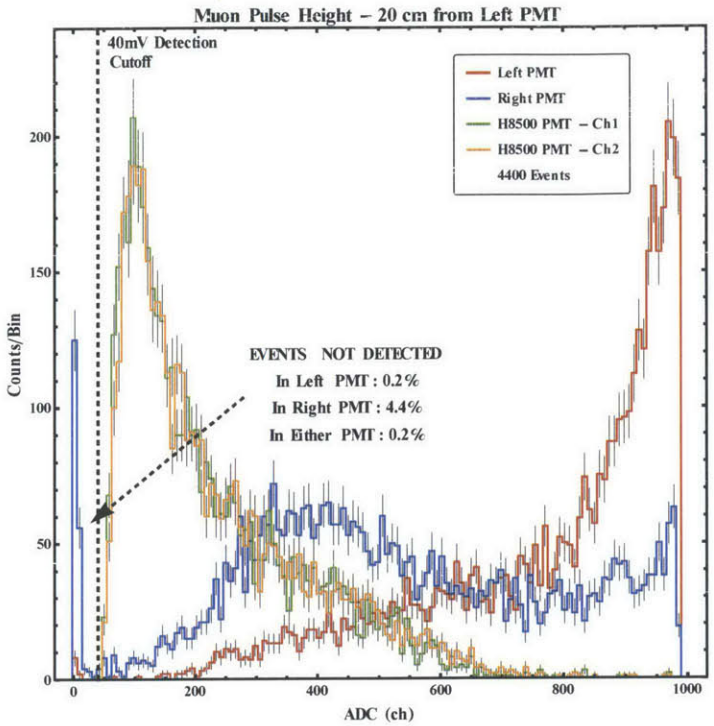

Figure 5.4. Detection module's response to muons at 20 cm from the left PMT. No more than 0.2% of triggered events are undetected by the either the left or right PMT.

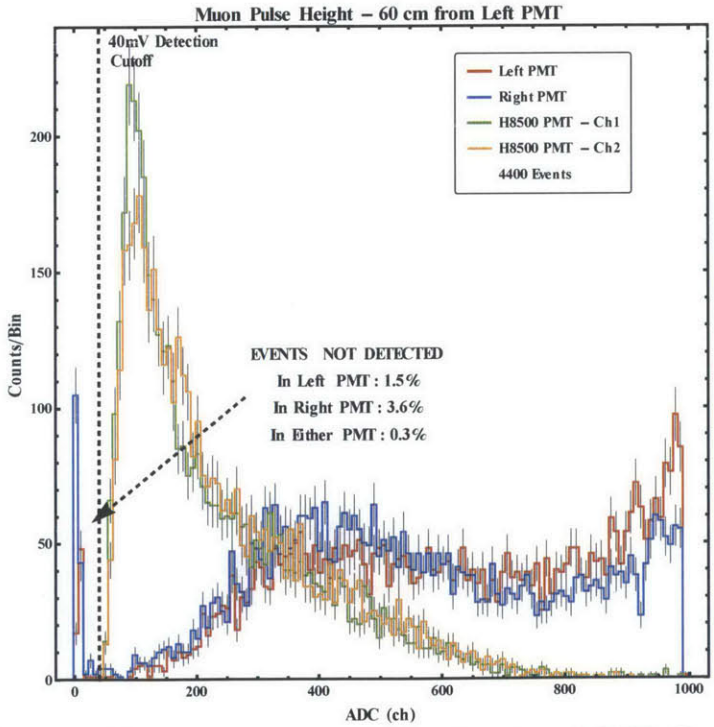

Figure 5.5. Detection module's response to muons at 60 cm from the left PMT. No more than 0.3% of triggered events are undetected by the either the left or right PMT.

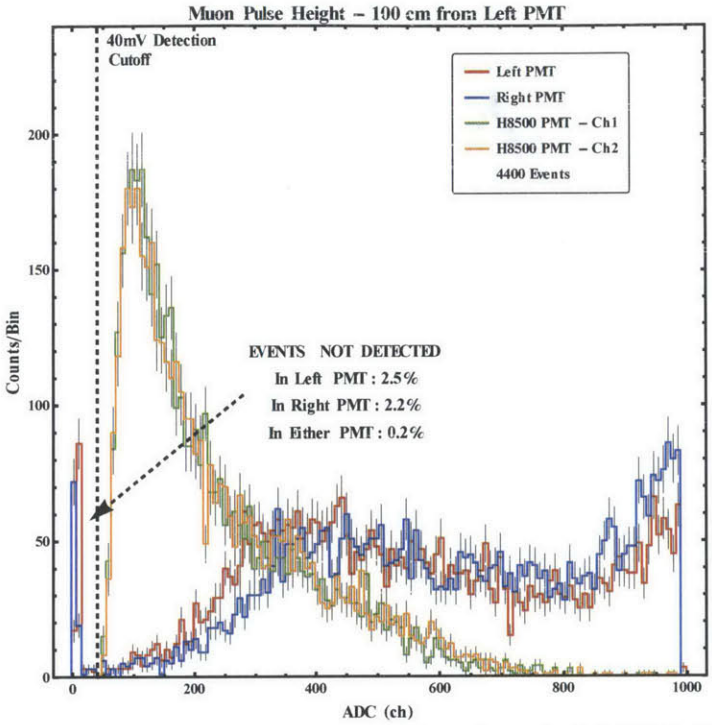

Figure 5.6. Detection module's response to muons at 100 cm from the left PMT. No more than 0.2% of triggered events are undetected by the either the left or right PMT.

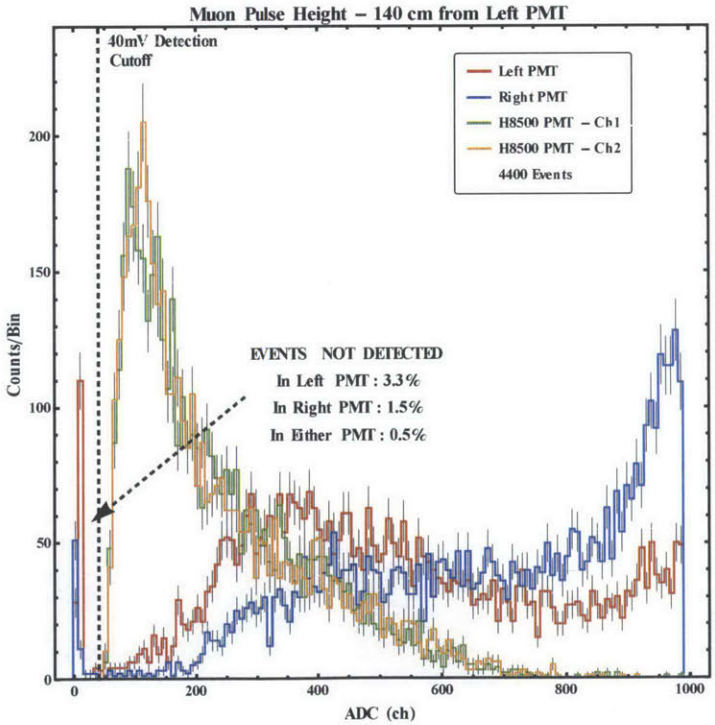

Figure 5.7. Detection module's response to muons at 140 cm from the left PMT. No more than 0.5% of triggered events are undetected by the either the left or right PMT.

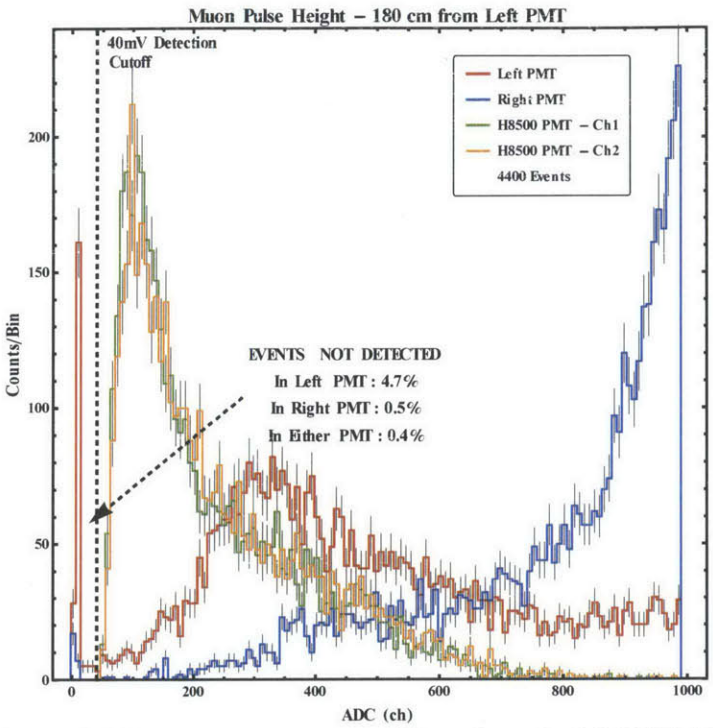

Figure 5.8. Detection module's response to muons at 180 cm from the left PMT. No more than 0.4% of triggered events are undetected by the either the left or right PMT.

5.3. Determining Interaction Position along Detection Module

Determining the interaction point along the detection module is necessary for muon path reconstruction. In the current cosmic ray imaging system, fibers in adjacent layers cross paths only once in the length of the tool. Therefore, the interaction point along the length of the tool is at the cross-section of adjacent layer fibers that experience a coincident event, as discussed in section 1.1.1. The uncertainty in the position depends on the fiber diameter and the angle at which the fibers cross. The current system has less than a 2 cm uncertainty in determining the position along the plastic fiber. Although an improvement to this uncertainty would be helpful, a gross determination may also play a role in future systems.

If only the length of the system is increased, the crossing angle between fibers would decrease and the position uncertainty would worsen unless the modules were allowed to cross more than once in the length of the tool. For example, in a 2-meter system with two crossing points, any two crossing points will be 1-meter apart with the same crossing angle and position uncertainty as a 1-meter system. In this case, a coincident event in adjacent layer fibers would give an intrinsic ambiguity between crossing locations along the fiber separated by 1-meter. If the WLS fiber signal could reliably resolve this ambiguity, a number of cost effective detector designs could become possible.

There are two potential methods for determining the interaction position along the module using the WLS fiber signal, i.e. the variation in light yield and the difference in pulse arrival time. The timing method was chosen in this work. The variation in light yield method requires a statistically significant light yield to reach both PMTs from all locations along the module. Although this may be achievable with additional WLS fibers, it is not currently a viable option. Also, the non-constant attenuation length complicates the position determination and requires a detailed characterization of the attenuation length. The variation in the pulse

arrival time is based on the speed of light in the WLS fiber polystyrene core and the path length difference as a function of position along the module. These methods will perform poorly or not at all if the OLS light is gradually escaping the tube and incident on the WLS fiber over an extended distance. Therefore, the spatial distribution of the light exiting the side of the fluoropolymer tube is considered first.

5.3.1. Measurement of Light Exiting Wall of Fluoropolymer Tube

Based on the light propagation model and shown in Figure 3.6, the light escaping the tube is expected to be localized near the interaction point. To verify experimentally, the light escaping the side of a small section of EJ-309 filled FEP tubing was measured using eight pixels of the H8500 PMT as shown in Figure 5.9. ^{90}Sr pulse height spectra were collected for each pixel for the five source locations identified. As expected, the majority of the light escapes localized at the source and distributed over a small region of 3 to 4 pixels, 1.8 cm to 2.4 cm. The results from source locations 1, 3, and 5 are summarized in Figure 5.10. With a 1 ns uncertainty equivalent to nearly 19 cm, this spatial distribution is not expected to be a critical factor.

Figure 5.9. A pixelated H8500 PMT was used to measure the distribution of light escaping the side of a FEP tube. The top row of a H8500 PMT consists of eight pixels. ^{90}Sr pulse height spectra are collected from each pixel for the source placed at the five location identified.

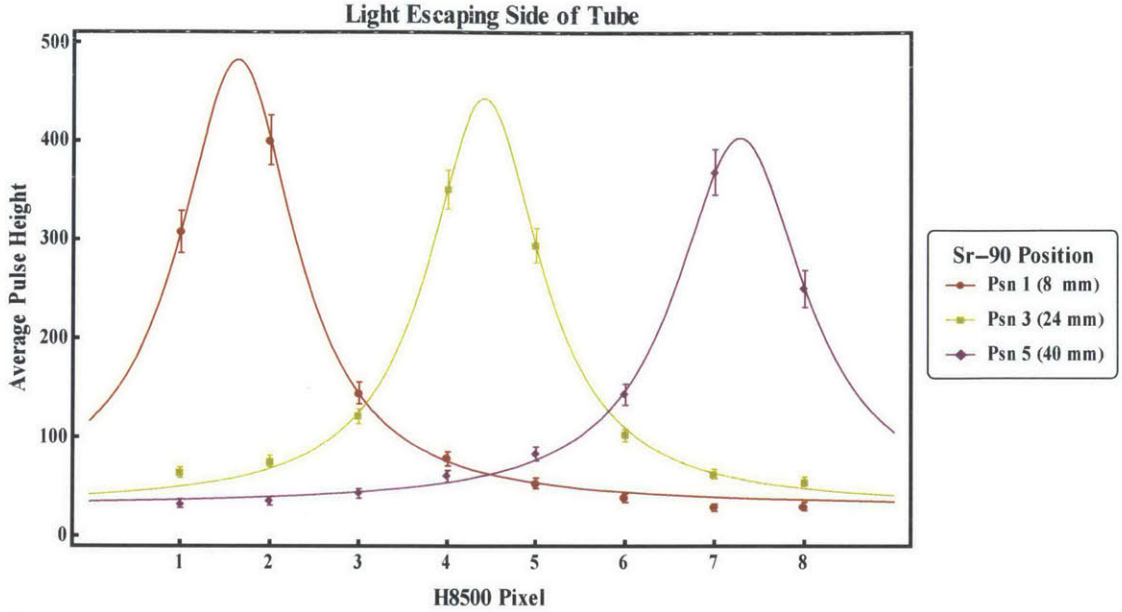

Figure 5.10. Light escaping the side of the side of the fluoropolymer tube is localized around the interaction point. Shown are the average pulse height for each pixel for three different source locations. The maximum pulse height is found facing the source location and rapidly decreases within two pixels. This corresponds to an effective 24 mm region in which light escapes a localized interaction point.

5.3.2. Pulse Timing Method

The portion of light produced in the OLS that exits the fluoropolymer tube, is absorbed in the WLS fiber, and is isotropically re-emitted with a decay time of 12 ns. After re-emitting the light, the WLS fiber acts as a multi-mode light guide resulting in many light paths to the PMT. These longer path lengths cause the travel time to be longer although all path lengths are directly proportional to the distance to the PMT. Assuming the increased travel time can be accounted for with a constant of proportionality of the form $c' = \alpha(c/n)$, the WLS fiber light from a muon event at position x, as shown in Figure 5.11, will arrive at the left and right PMTs at

$$t_{Left} \propto x/c' \quad and \quad t_{Right} \propto (L - x)/c' \tag{5.1}$$

where c is the speed of light in a vacuum, the index of refraction for the polystyrene core is n = 1.6, and L is the length of the WLS. Using the measured difference in pulse arrival time, the position is calculated as

$$x = \left(L - c'\left(t_{Right} - t_{Left}\right)\right)/2. \tag{5.2}$$

Based on the data collected the constant of proportionality is $\alpha = 0.7$. Figure 5.12 shows the measured difference in pulse arrival times for events occurring at 20 cm, 100 cm. and 180 cm from the left PMT.

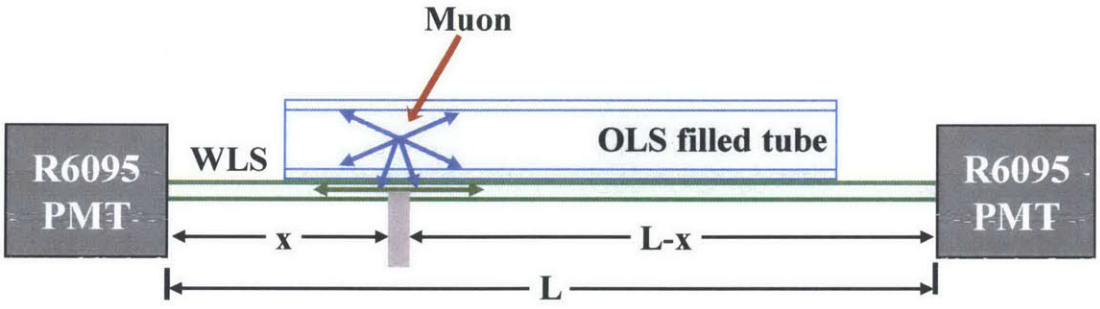

Figure 5.11. Position determination using pulse arrival time at left and right PMTs.

These results use the experimentally determined constant of proportionality to correlate the difference in pulse arrival time to the distance from the left PMT. The datasets have a consistent standard deviation of 4.8 ns or 36 cm and the mean values of the data collected are consistent with the measurement locations. The main contributions to the uncertainty in timing are the digitizer sampling rate (1 ns), the PMT response time (4 ns), and the WLS fiber decay time (12 ns) Some potential experimental changes to improve the uncertainty, but not conducted here, include:

- using a WLS fiber with a faster decay time such as BCF-92 (2.7 ns);
- using the H8500 PMT (0.8 ns rise time compared to the R6095's 4 ns rise time);

- operating the V1751 at 2 GSa/s (0.5 ns); and/or
- using a time to digital converter such as the CAEN V1190A (0.1 ns);

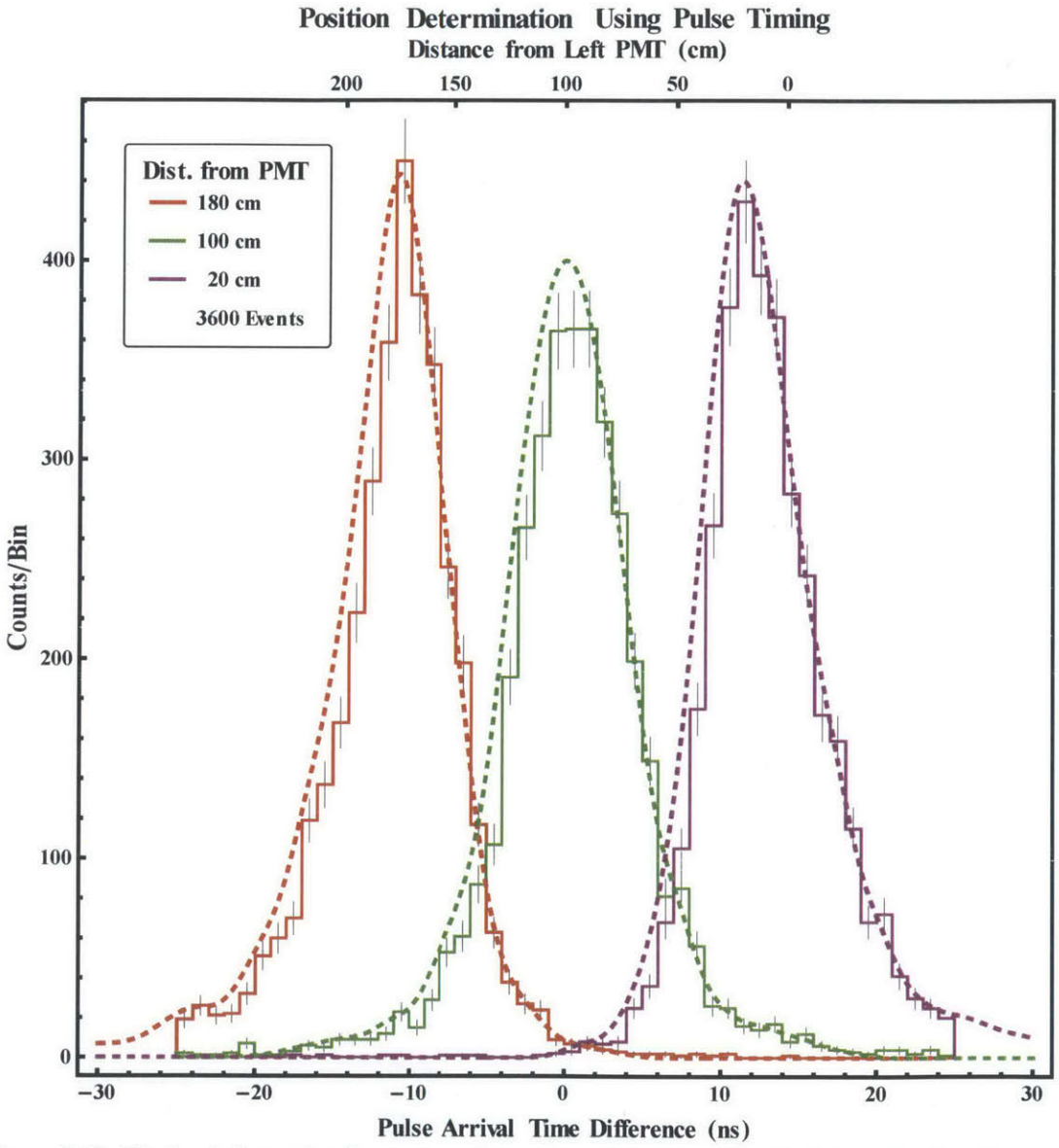

Figure 5.12. Timing information from muon data was used to determine the interaction location.

To evaluate the timing capability to distinguish an event as occurring at one of two possible locations separated by 100 cm, the data taken at 180 cm from the left PMT was shifted 20 cm to represent a measurement at 160 cm and compared to the 60 cm data. As shown in Figure 5.13, less than 5% of these events would have been assigned the incorrect fiber crossing

point. In addition, each coincident event consists of two modules. This provides a second timing measurement, further reducing the probability of misidentifying the crossing point to $5\% \times 5\% = 0.25\%$. Currently the CRI electronics do not collect any timing information and may require significant modifications to implement this timing method.

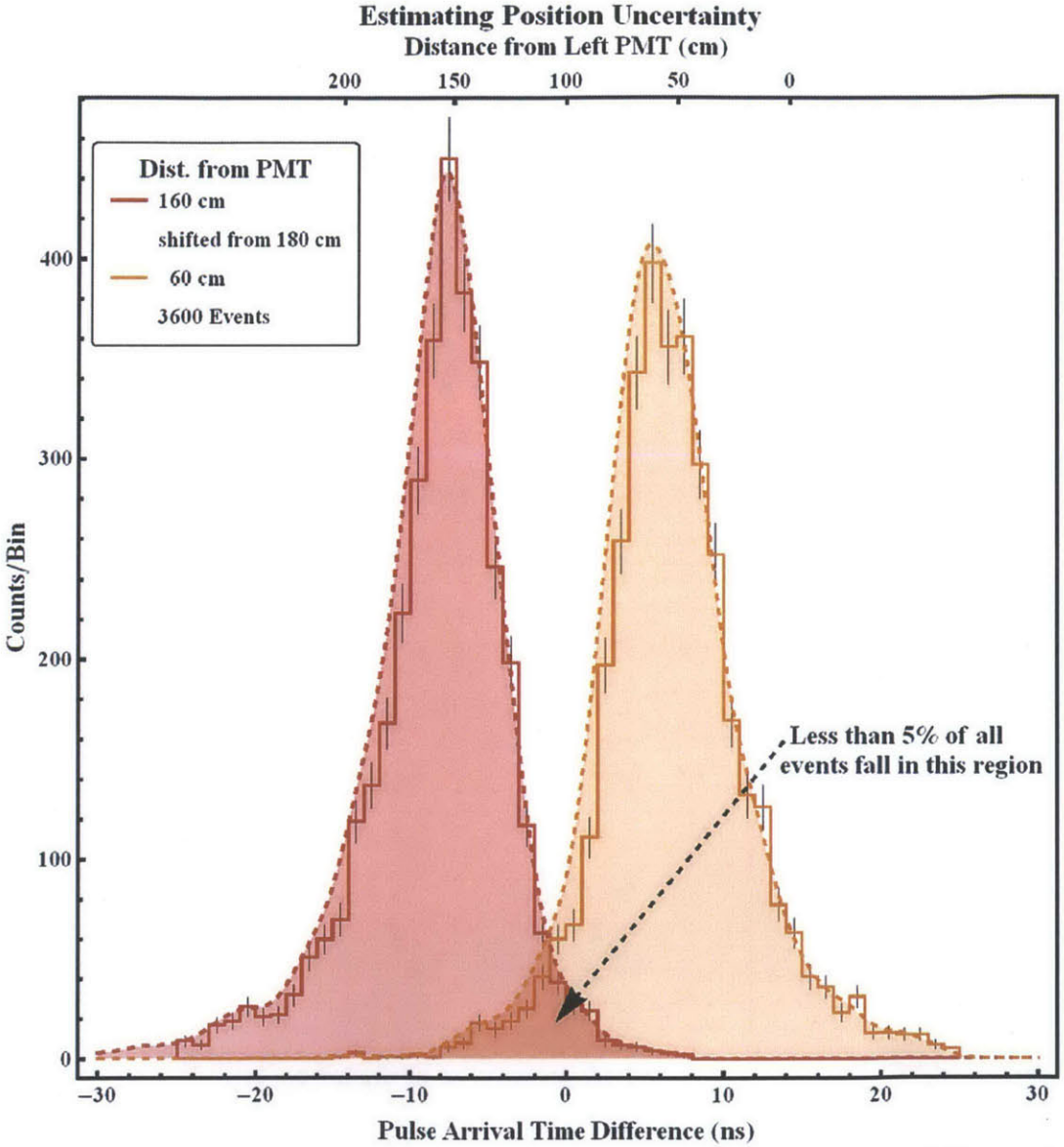

Figure 5.13. Analysis of timing information ability to discriminate between two potential interaction points separated by 100 cm. Less than 0.25% of events occurring 100 cm apart will be misidentified when using timing data from both fibers in coincidence.

6. Detecting Neutrons

In this chapter, preliminary tests to evaluate the proposed detection module as a fast neutron detector for nuclear security applications are conducted. In most of the nuclear security scenarios, a neutron detection system will have to operate in the presence of background gamma radiation either from terrestrial sources or from the unidentified neutron source. Therefore, it is important to have the capability to distinguish neutron from gamma rays events. The detection module uses EJ-309, a relatively new OLS that is well known for its pulse shape discrimination capability [27, 28, 48-50] In the proposed module, the OLS light is first absorbed by the WLS fiber and then re-emitted before being channeled to the PMT. The intent of this research is to determine if the re-emitted WLS fiber light pulses retain the characteristics of the original EJ-309 pulses, i.e., can pulse shape discrimination techniques be successfully applied to the WLS fiber light pulses. Currently, pulse shape discrimination is limited to geometries in which a large fraction of the light pulse is directly captured by a PMT, e.g., small cylindrical geometries. The capability to fill more complicated geometries with flexible OLS modules, read the OLS signal out using WLS fibers, and perform neutron-gamma ray discrimination has the potential to replace ^{3}He in some applications.

6.1. Experimental Setup

The experimental setup was designed to determine if the light pulses in the WLS fiber retain any pulse shape discrimination characteristics and the extent this is affected by the digitizer sampling rate and resolution. In the setup shown in Figure 6.1, four 2 mm WLS fibers were attached to an EJ-309 filled FEP tube and R6095 PMTs were used to measure the WLS fiber signal and the light escaping the side of the tube. The fraction of light escaping the side

of the tube that is measured by the R6095 PMT is expected to have the same characteristics as the light absorbed and subsequently re-emitted by the WLS fiber.

The pulses were digitized using both the V1751 and a DT5720 digitizers. The V1751 has a sampling rate of 1GSa/s and a 10 bit resolution over a 1 volt range while the DT5720 digitizer has a sampling rate of 250MSa/s and a 12 bit resolution over a 2 volt range. Coincident pulses from the OLS tube and the WLS fiber, above a 30mV threshold, triggered the collection of both pulses in both digitizers. The collection windows for the DT5720 and V1751 were set for 256 samples and 1024 sample, respectively. This corresponds to approximately one microsecond.

Various source combinations of a 10mCi AmBe (December 2010), a 1μCi ^{60}Co (February 2006), and a 1μCi ^{137}Cs (February 2008) were measured for thirty minutes each. A lead shield was placed in front of the AmBe to reduce the number of gamma rays reaching the detection module. The detectors were placed inside a lightproof container during the collection. This required the high voltage supplies to be turned off when the sources were changed. The four WLS fiber ends, as shown in Figure 4.5, were coupled to the R6095 PMT with optical grease to improve their optical contact.

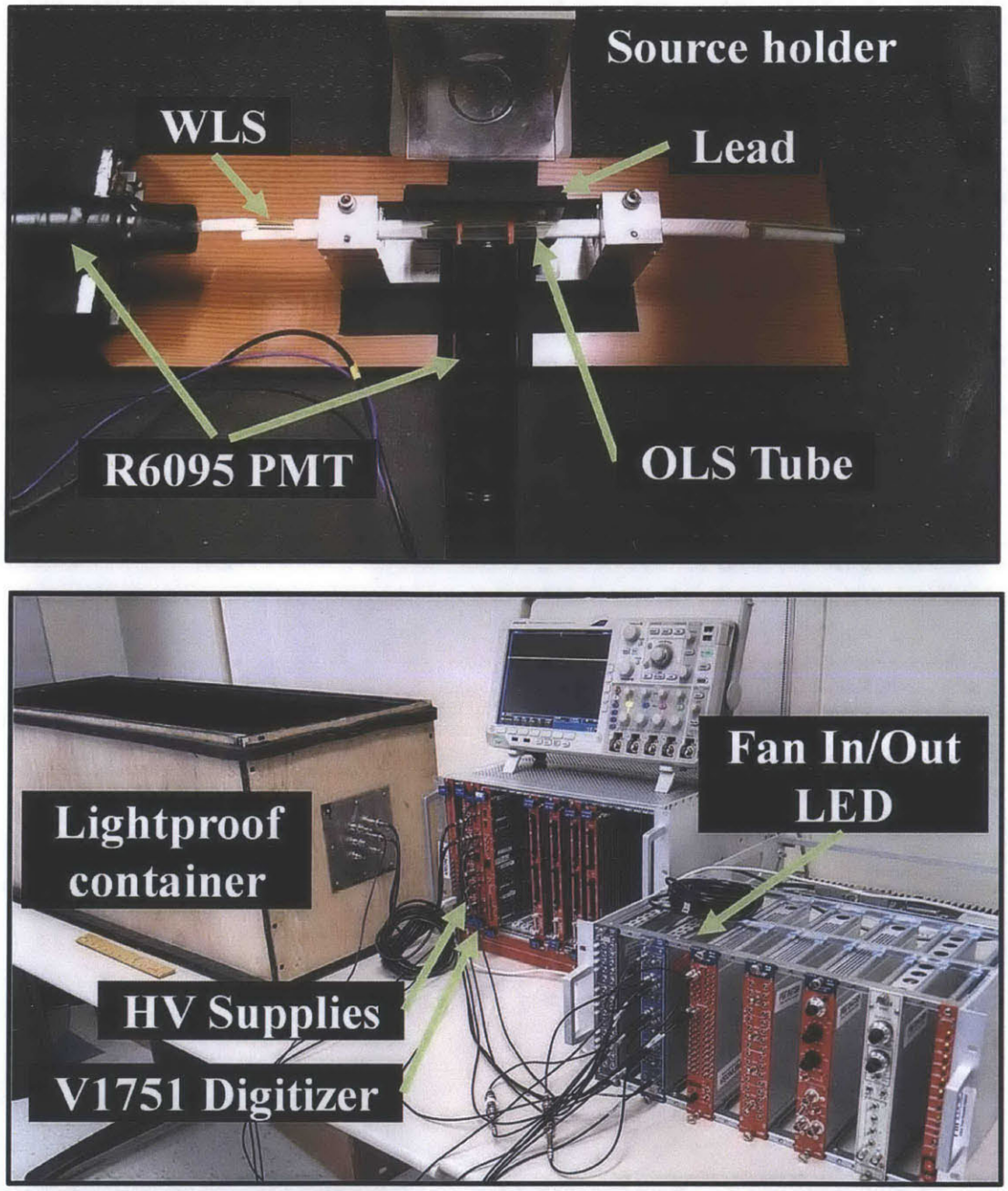

Figure 6.1. Experimental setup for fast neutron detection application. Above: Equipment placed inside lightproof container. One R6095 PMT is used to evaluate the pulse shape discrimination directly in the EJ-309 and the second R6095 PMT is used to measure the WLS fiber signal. A lead shield was used to reduce the AmBe gamma rays reaching the OLS filled tube. Below: The electronics included a V1751 digitizer, a DT5720 digitizer (not shown), and a V6521 high voltage power supply.

6.2. Digital Pulse Shape Discrimination Algorithms

As previously discussed, the ability to distinguish gamma rays from neutrons is an important capability for nuclear security applications. The extended tail of a neutron pulse is the basis for pulse shape discrimination. Sample neutron and gamma ray pulses collected from the OLS filled FEP tube are shown in Figure 6.2. During post-processing, the baseline for each pulse is determined and the pulse is inverted. Each pulse is evaluated for excessive noise before being processed. Depending on the PSD algorithm, the pulses are filtered to reduce fluctuations caused by signal noise and the sampling frequency of the digitizer. The advantage of capturing digital pulses for post processing is the ability to evaluate multiple algorithms on the same set of pulses. Thirty minute measurements of AmBe, ^{137}Cs, and ^{60}Co were conducted capturing the WLS fiber and OLS signals with both digitizers. Three PSD algorithms were applied to the data sets; charge ratio, pulse gradient analysis, and rise time. In all PSD methods, the ^{137}Cs events were plotted inside the same regions as the ^{60}Co events, therefore the ^{137}Cs are omitted for clarity. Where applicable, a line identifying the threshold between neutron and gamma ray events is estimated and a figure of merit (FOM) calculated using

$$FOM = \frac{Peak\ Separation}{FWHM_n + FWHM_\gamma} \tag{6.1}$$

where the peak separation and the full widths at half maximum are identified from normal distributions fitted to the discrimination parameters of neutron and gamma ray events. Each PSD method is briefly introduced and the results summarized in the following sections.

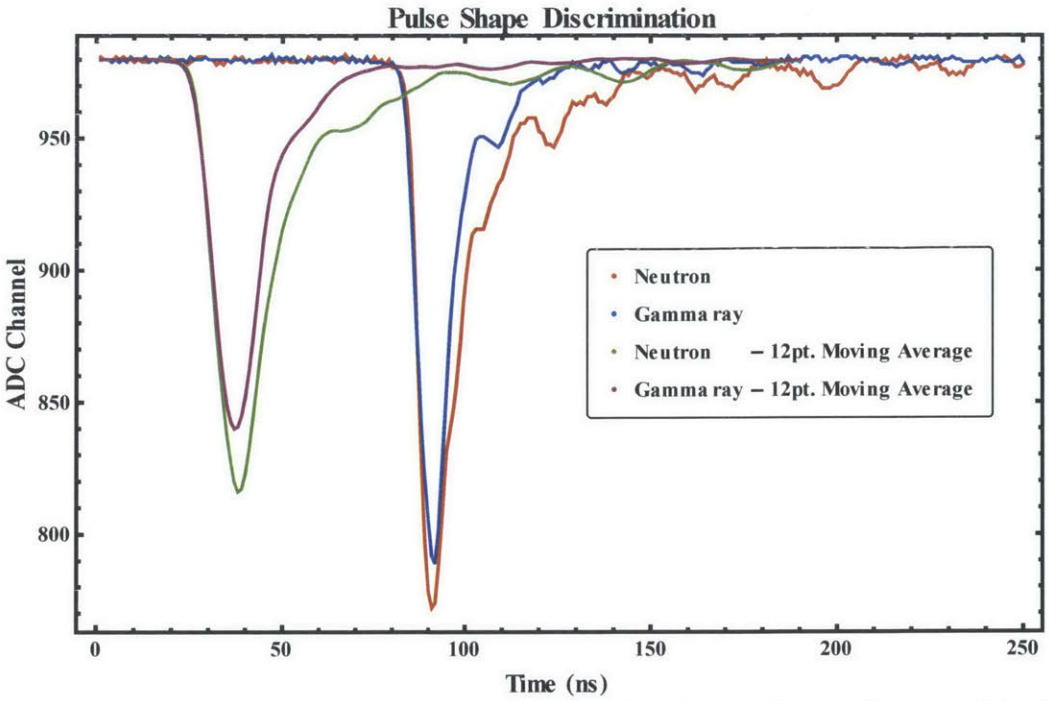

Figure 6.2. Neutron and gamma ray pulses collected from OLS filled FEP tube. The extended tail of the neutron pulse is the basis of pulse shape discrimination. Degradation in the timing or amplitude of the pulses results in degraded pulse shape discrimination capability. Multi-point moving average filters are commonly used to reduce noise before applying PSD algorithms.

6.2.1. Charge Ratio

The charge ratio method compares the integrated pulse in two time windows corresponding to the full pulse and the pulse tail to discriminate between neutrons and gamma rays.[51] The windows are optimized for the specific scintillator and detector geometry. The time window used for the total integral was 500 ns and the tail integral started 16 ns after the peak and stopped at the same time as the total integral. Figure 6.3 and Figure 6.4 show the charge ratio method applied to light escaping the side of the EJ-309 filled tube for an AmBe source compared to a ^{60}Co source using the DT5720 and V1751 digitizers. The gamma rays from the AmBe source are clearly still present and fall in the same region as the ^{60}Co events.

A line was graphically chosen to minimize the number of ^{60}Co events falling above the line and maximize the number of AmBe events falling above the line. The discrimination lines

chosen result in less than 1% of the 5000 ^{60}Co events misidentified as neutrons and approximately 38% of the 5000 AmBe events are identified as neutrons. Because no truly pure neutron data was collected, the 1900 events identified as neutrons are used to evaluate the discrimination capability of the WLS fiber and the remaining PSD methods. The charge ratio method applied to the WLS fiber signal is shown in Figure 6.5 and Figure 6.6. Based on the timing parameters chosen, the WLS fiber signal does not show any PSD capability using the charge ratio method. Although the ^{60}Co events may be slightly shifted below the AmBe neutron events, they cannot be separated. The additional random nature of the WLS fiber light production adds irregularities to the pulse shape. With the fixed time intervals used in this method, the variation from pulse to pulse blurs the neutron and gamma ray events.

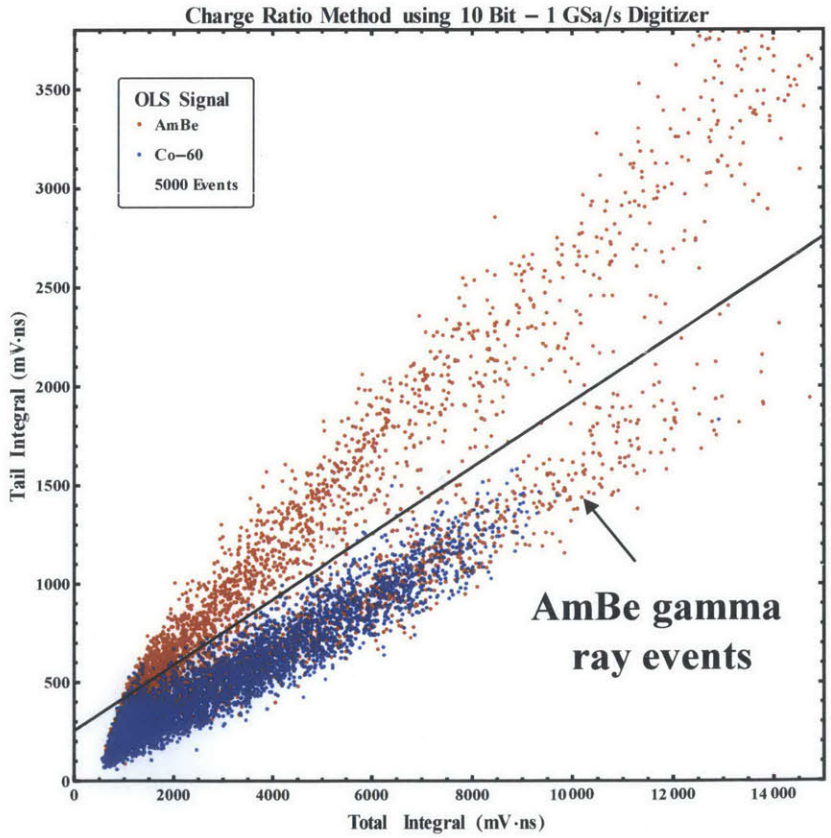

Figure 6.3. The charge ratio method applied to light escaping the side of the EJ-309 filled tube for an AmBe source compared to a ^{60}Co source using the V1751 digitizer. The discrimination line was graphically identified and resulted in a FOM=0.53.

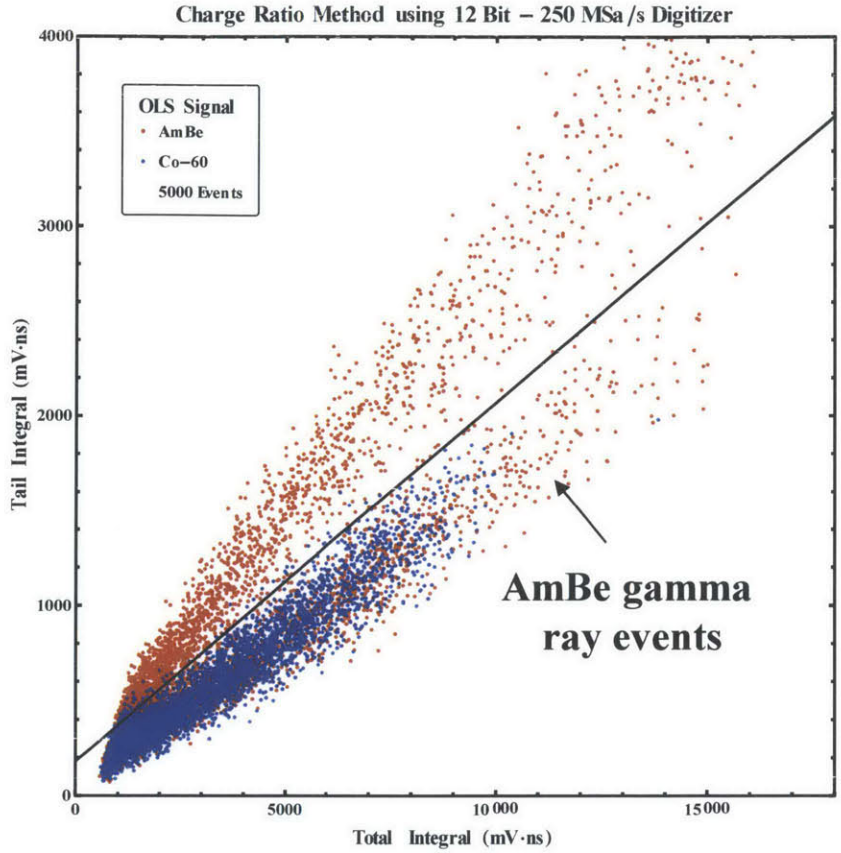

Figure 6.4. The charge ratio method applied to light escaping the side of the EJ-309 filled tube for an AmBe source compared to a ^{60}Co source using the DT5720 digitizer. The discrimination line was graphically identified and resulted in a FOM=0.52.

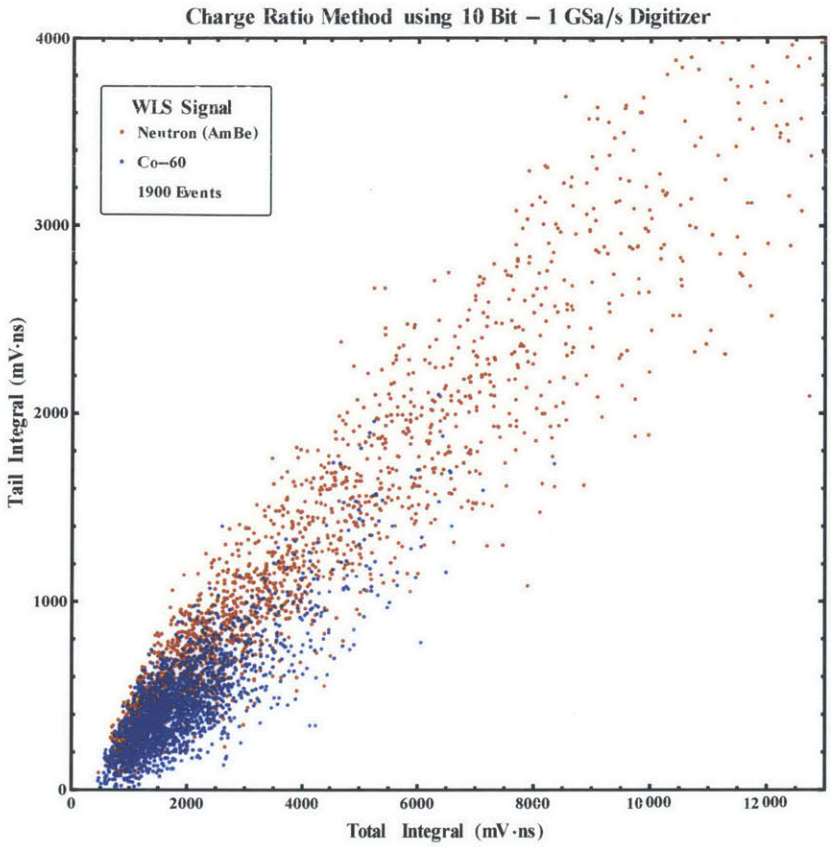

Figure 6.5. The charge ratio method applied to WLS fiber signal for an AmBe source compared to a ^{60}Co source using the V1751 digitizer. The WLS fiber signal shows no clear pulse shape discrimination.

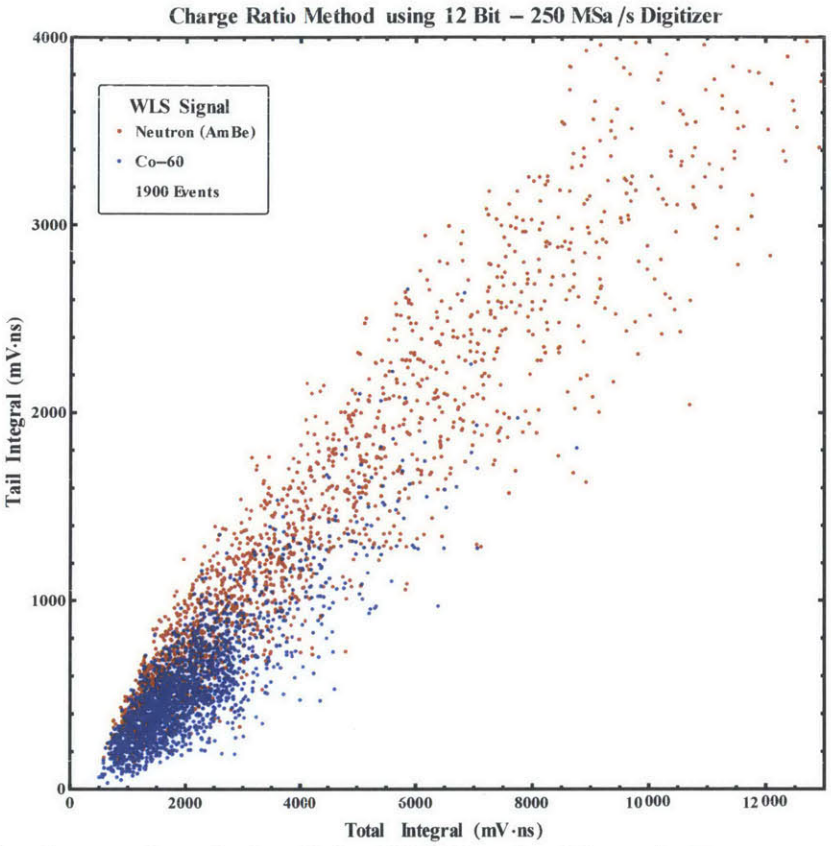

Figure 6.6. The charge ratio method applied to WLS fiber signal for an AmBe source compared to a ^{60}Co source using the DT5720 digitizer. The WLS fiber signal shows no clear pulse shape discrimination.

6.2.2. Pulse Gradient Analysis Method

The light output of organic scintillators are often modeled as the decay of several exponential terms and estimating the actual decay rate from continuous data can be computationally intensive.[52] The pulse gradient analysis (PGA) method simplifies the process by estimating the gradient with the pulse height difference between two points. The first point is the peak of the pulse and the second is chosen at a fixed time following the peak. The pulse height at the second point is called the discrimination amplitude. Neutron pulses with slower gradients will have higher discrimination amplitudes than gamma ray pulses.

Plotting the discrimination value against the peak height provides a graphic assessment of the pulse shape discrimination. Fixed times of 16 ns, 20 ns, and 24 ns were applied to the data sets collected. Figure 6.7 through Figure 6.10 display the results using a fixed time of 24 ns. As seen in the charge ratio method, the WLS fiber signals do not readily display a PSD capability. The EJ-309 PSD capability is still visible but degraded with a FOM of 0.40 compared to 0.52 from the charge ratio method. The discrimination lines chosen for the EJ-309 signals yields similar discrimination for both digitizers with approximately 85% of the AmBe neutrons identified as neutrons and less than 6% of the ^{60}Co gamma rays incorrectly identified as neutrons. Lower energy events are known to be more difficult to discriminate and higher thresholds are typically used.[50] When a 95 mV threshold is applied, 1% of the ^{60}Co gamma rays are incorrectly identified as neutrons with a corresponding reduction in neutron identification to 58%.

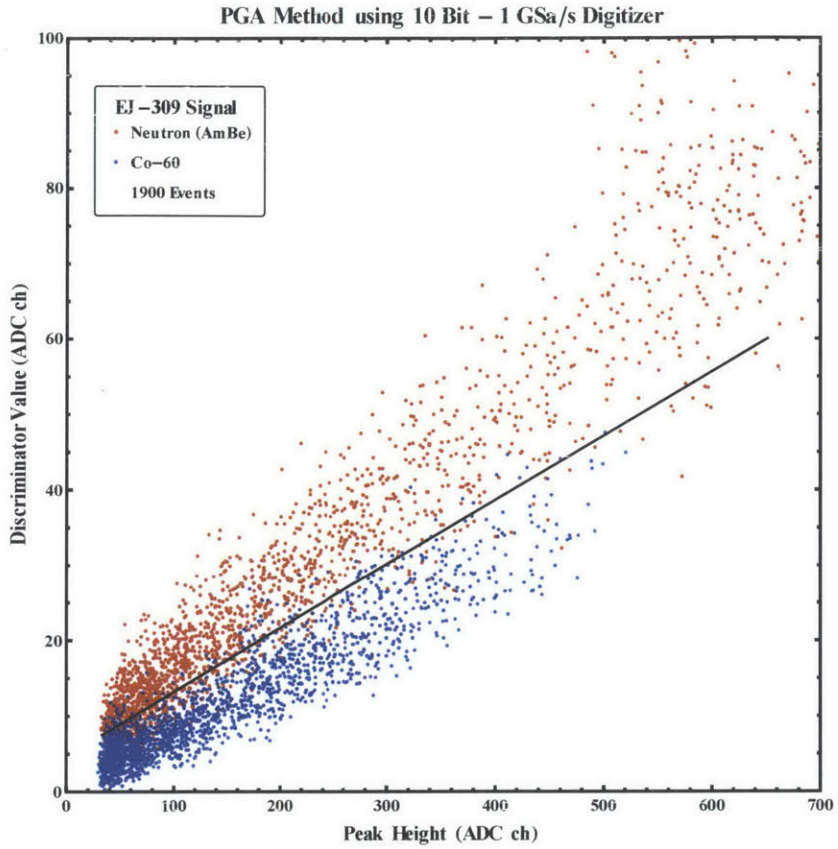

Figure 6.7. The pulse gradient analysis (PGA) method applied to light escaping the side of the EJ-309 filled tube for an AmBe source compared to a ^{60}Co source using the V1751 digitizer. The discrimination line was graphically identified and resulted in a FOM=0.40.

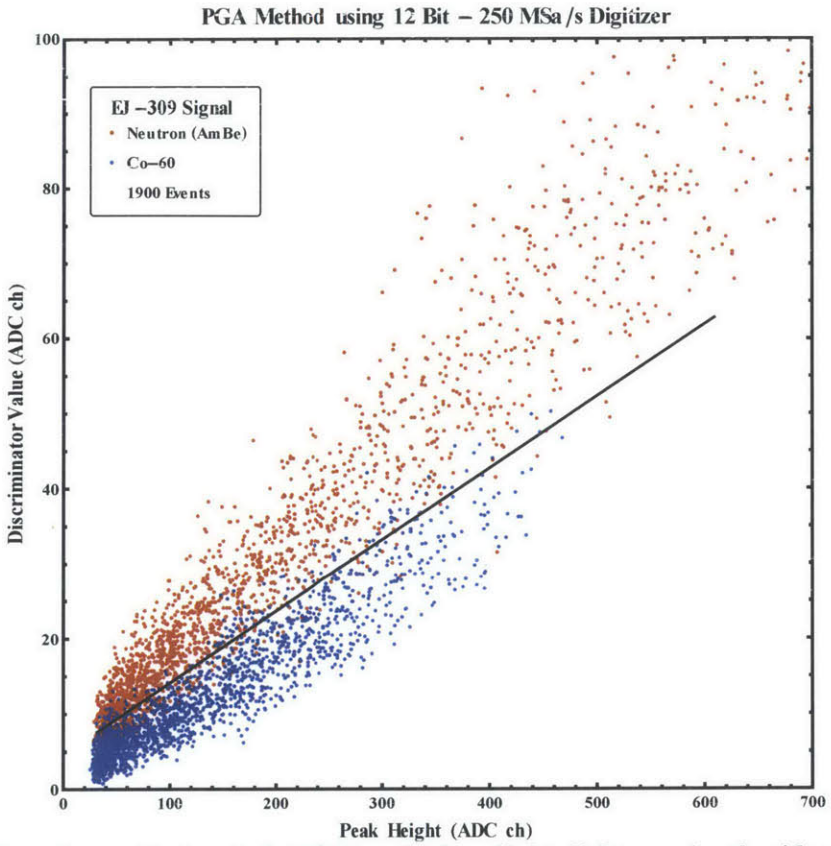

Figure 6.8. The pulse gradient analysis (PGA) method applied to light escaping the side of the EJ-309 filled tube for an AmBe source compared to a ^{60}Co source using the DT5720 digitizer. The discrimination line was graphically identified and resulted in a FOM=0.40.

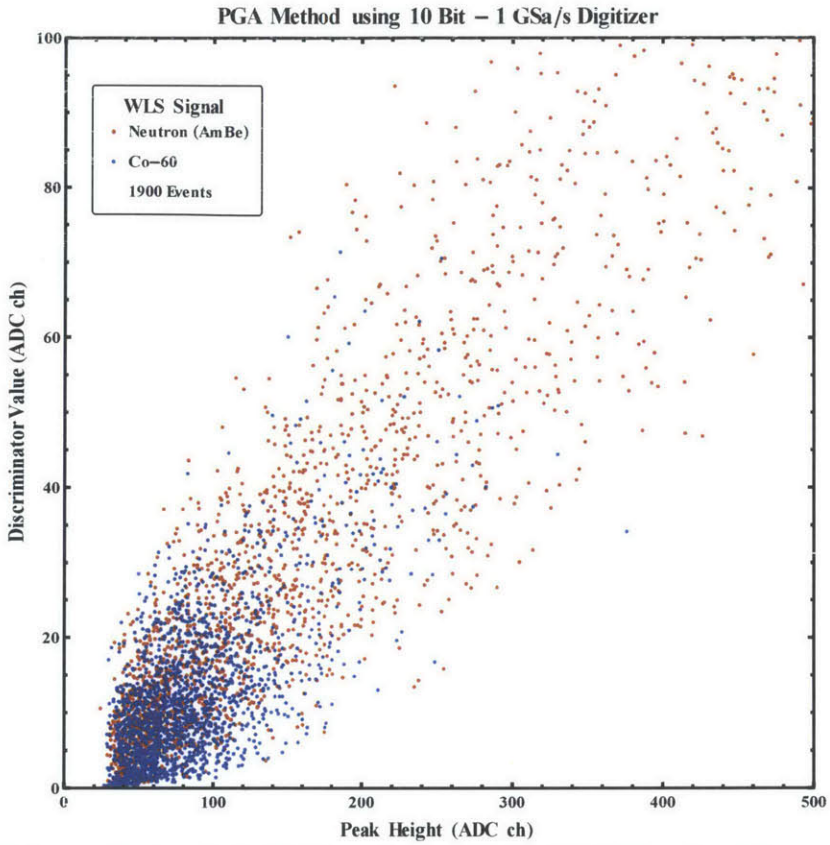

Figure 6.9. Pulse gradient analysis (PGA) method applied to WLS fiber signal for an AmBe source compared to a ^{60}Co source using the V1751 digitizer. The WLS fiber signal shows no clear pulse shape discrimination.

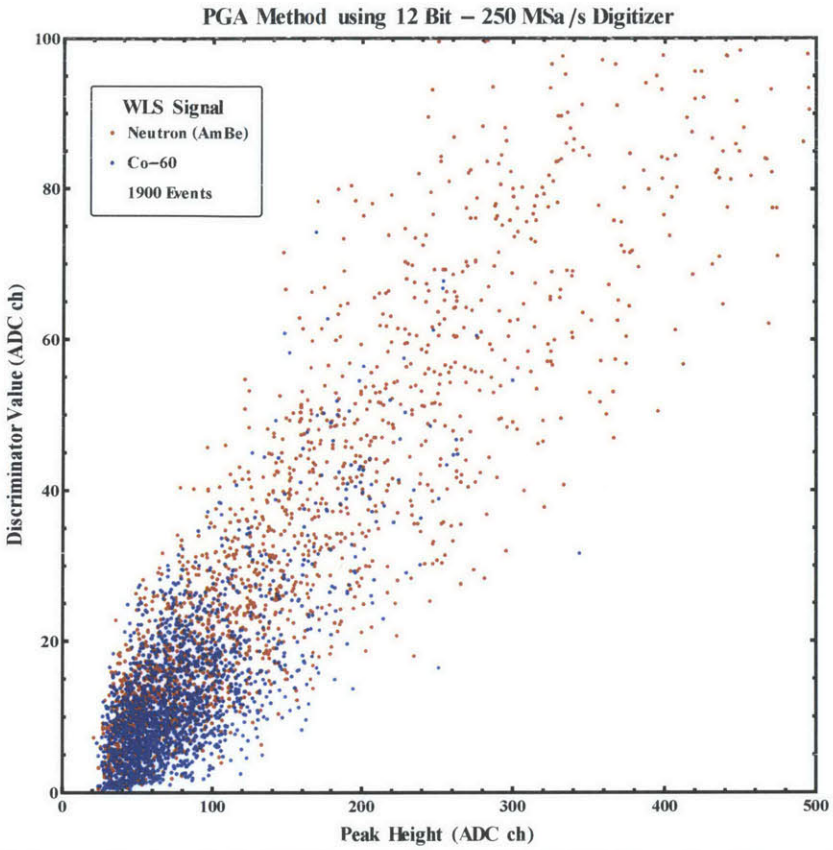

Figure 6.10. Pulse gradient analysis (PGA) method applied to WLS fiber signal for an AmBe source compared to a ^{60}Co source using the DT5720 digitizer. The WLS fiber signal shows no clear pulse shape discrimination.

6.2.3. Rise Time Method

The longer tail of neutron pulses causes its integrated pulse to take longer to reach its maximum, as shown by the sample pulses collected from the EJ-309 filled FEP tube in Figure 6.11. The rise time method analyzes the integrated pulse measuring the time from 10% to 80% of its maximum. Many works have analyzed theses parameters for different scintillators and

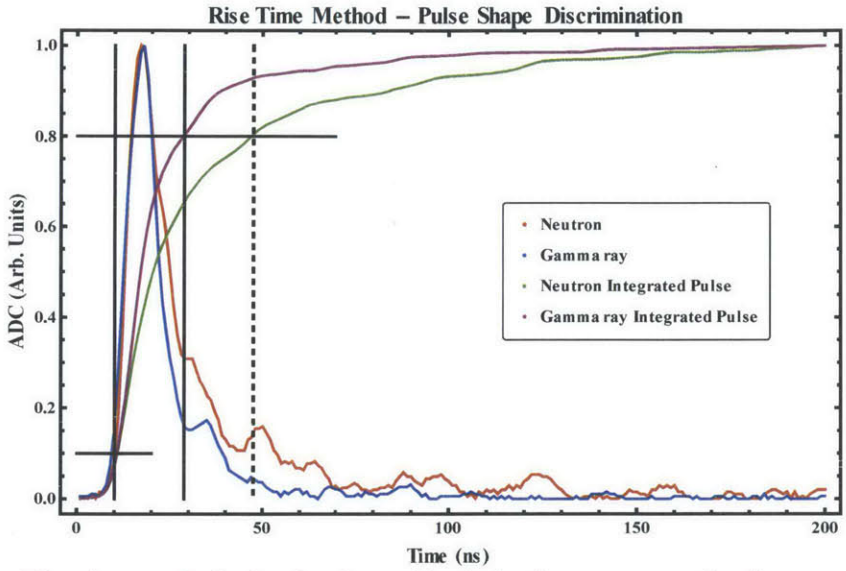

Figure 6.11. Rise time method of pulse shape discrimination measures the time required for an integrated pulse to reach 80% of its maximum.

geometries and generally the optimal values are between 10% and 90%.[51, 53-56] The rise time analysis for the data collected is shown in Figure 6.12 through Figure 6.15. An offset exponential of the form

$$y = a + b\, e^{-(x+c)} \tag{6.2}$$

was used as the discriminator between neutron and gamma ray events. The OLS signal measured with the V1751 fast digitizer identified 88% of the AmBe neutrons as neutrons and 6% of the ^{60}Co gamma rays incorrectly identified as neutrons. The DT5720 achieved similar results with 95% of the AmBe neutrons as neutrons and 4% of the ^{60}Co gamma rays incorrectly

identified as neutrons. The WLS fiber signal also demonstrated a PSD capability with similar results in both the V1751 and DT5720 digitizers. Based on the discrimination lines chosen, 65% of the AmBe neutrons were identified as neutrons and 8% of the ^{60}Co gamma rays incorrectly identified as neutrons. Additional optimization of the discriminator lines would improve the PSD performance. The rise time method, unlike charge ratio and PGA, does not evaluate each pulse at a predetermined times but evaluates the timing characteristics from pulse to pulse. This allows the degraded, but still present, timing characteristics to be extracted.

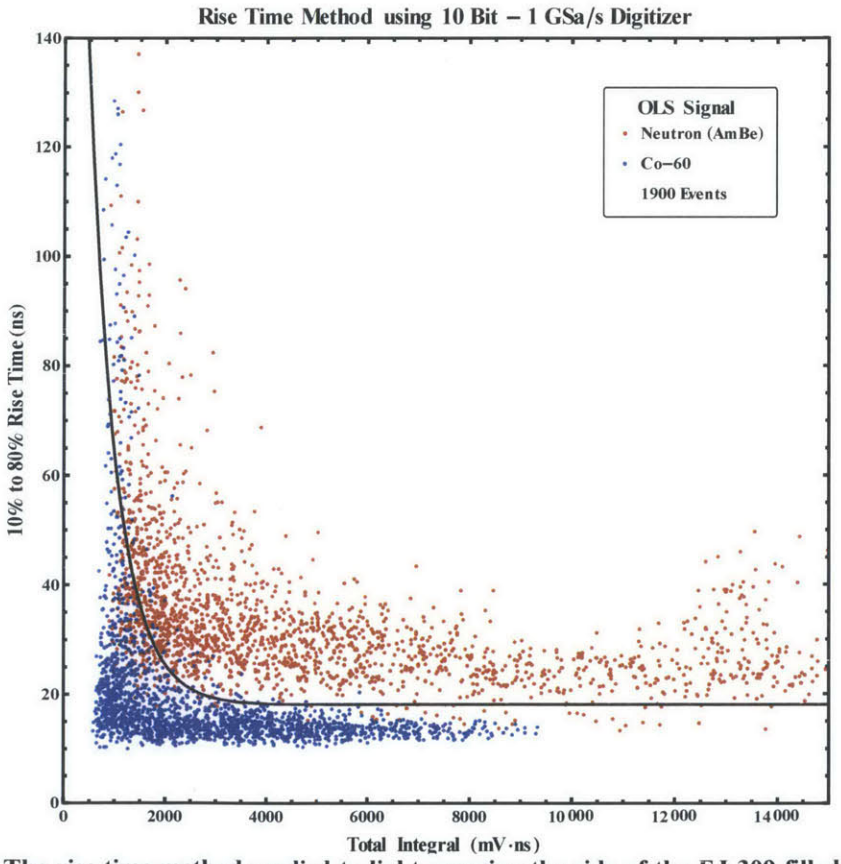

Figure 6.12. The rise time method applied to light escaping the side of the EJ-309 filled tube for an AmBe source compared to a ^{60}Co source using the V1751 digitizer. The discrimination line was graphically identified and resulted in a FOM=0.56.

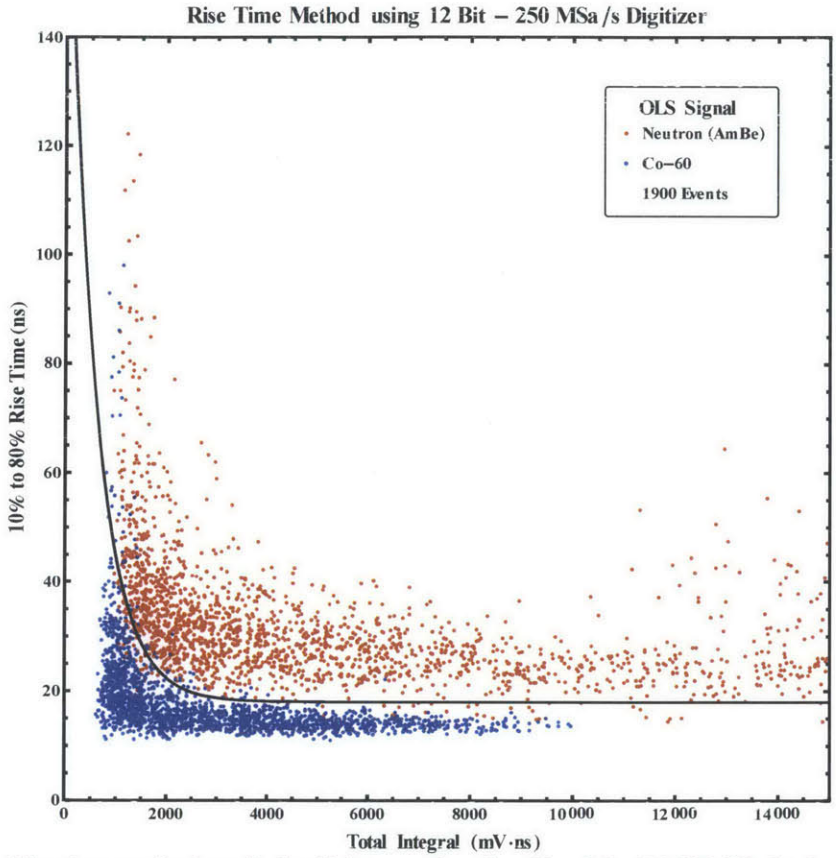

Figure 6.13. Rise time method applied to light escaping the side of the EJ-309 filled tube for an AmBe source compared to a ^{60}Co source using the DT5720 digitizer. The discrimination line was graphically identified and resulted in a FOM=0.58.

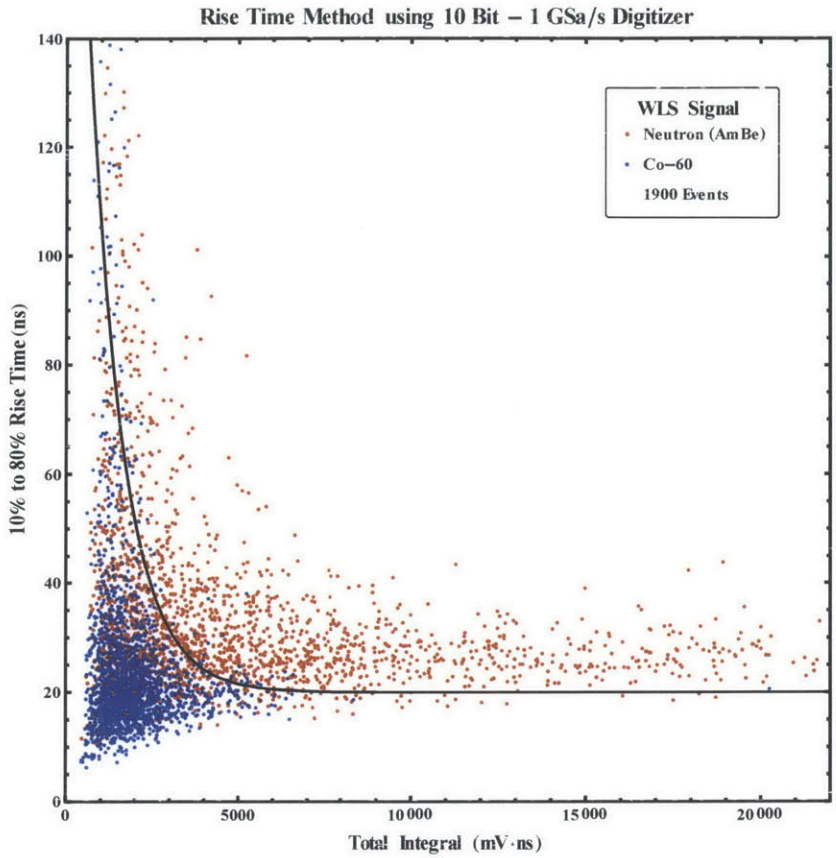

Figure 6.14. The rise time method applied to the WLS fiber signal for an AmBe source compared to a ^{60}Co source using the V1751 digitizer. The discrimination line was graphically identified and resulted in a FOM=0.45.

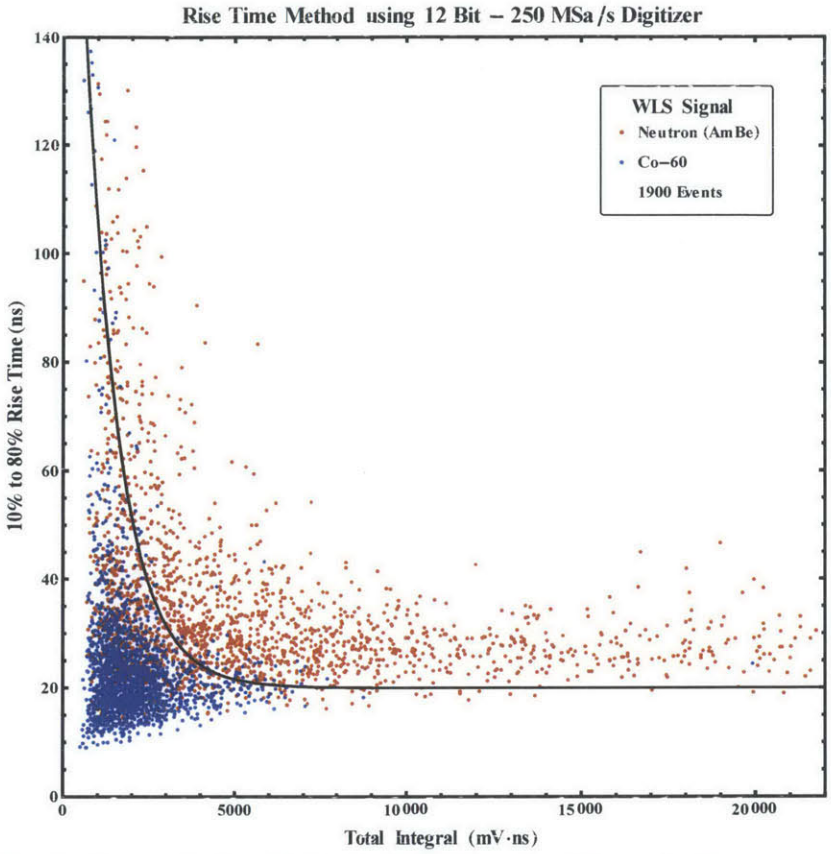

Figure 6.15. The rise time method applied to the WLS fiber signal for an AmBe source compared to a ^{60}Co source using the DT5720 digitizer. The discrimination line was graphically identified and resulted in a FOM=0.43.

6.2.4. Pulse Shape Discrimination Summary

EJ-309's pulse shape discrimination capability and its lower toxicity and flammability has made the relatively new organic scintillator a popular topic of recent research. Many institutions and organizations continue to characterize its light production for a wide range of applications. The intent of this research was to determine if the re-emitted WLS fiber light pulses retain the characteristics of the original EJ-309 pulses. The measurement of the EJ-309 light escaping the side of the tube was not optimized and only a fraction of the light was collected. As expected, poorer PSD capability from the EJ-309 was observed as summarized in Table 6.1.

Table 6.1. Summary of Pulse Shape Discrimination Methods

Method	Digitizer	Signal	Correctly ID Neutron (%)	Incorrectly ID ^{60}Co (%)	FOM
Charge Ratio	V1751	WLS	NA	NA	0
		OLS	*	1	0.53
	DT5720	WLS	NA	NA	0
		OLS	*	1	0.52
Pulse Gradient Analysis	V1751	WLS	NA	NA	0
		OLS	82	6	0.40
	DT5720	WLS	NA	NA	0
		OLS	86	3	0.40
Rise Time Method	V1751	WLS	64	8	0.45
		OLS	88	6	0.56
	DT5720	WLS	66	5	0.43
		OLS	95	4	0.58

***Charge ratio method is used as basis for identifying AmBe neutrons since a purely neutron source was not used.**

No PSD capability was observed using the charge ratio and pulse gradient analysis methods on the WLS fiber signals. Both of these techniques are sensitive to variations in the pulse timing. Pulses not consistent with the neutron or gamma ray timing profile will not be properly discriminated. With BCF-91A's 12 ns decay time, the added absorption and re-emission in the WLS fiber blurs a pulse's timing profile. The long integration window of the

rise time method evaluates each pulse's timing profile separately making it more tolerant to the loss in precise timing. As a result, discriminating gamma ray events, currently at a cost of neutron efficiency, is possible through the WLS fiber signal. There are many aspects of the system that can be optimized to improve its PSD capability.

6.3. Fast Neutron Detection Efficiency

Without achieving a purely neutron source it is difficult to determine the fast neutron detection efficiency without large uncertainties. In a separate test, the shielded AmBe source used in the pulse shape discrimination analysis was placed 6 inches from two 6" EJ-309 filled modules. Each was read-out using two 2mm diameter WLS fibers and the H8500 PMT. The count rate measured after subtracting the background was 7.9 Hz. Based on the charge ratio method, two fifths of the detected events were determined to be neutrons giving a neutron detection rate of 3.2 Hz. The 10 mCi AmBe source emits approximately 22,000 neutron per second isotropically giving 86 neutrons per second incident on the two detections modules. This provides an estimated 3.7% intrinsic fast neutron detection efficiency in a single layer of the detection modules with an estimated 14% for a four-layer system. The plutonium based nuclear weapon discussed in section 2.3.2 emits 1430,000 neutrons per second. A one square meter panel of single layer modules at ~2 meters from the weapon would count 1 million neutrons in 65 minutes and a four-layer system would take less than 15 minutes. At a distance of ~4 meters these times increase to 260 minutes and 60 minutes, respectively. Operational measurements of 15-60 minutes are reasonable and suggests further research is warranted.

7. Conclusions and Future Work

Industrial and nuclear security applications continue to demand innovative radiation detection solutions for complex scenarios. In this work, we explore a common solution to the vastly different applications of oil reservoir saturation monitoring with cosmic ray imaging and the identification of illicit special nuclear material with fast neutron detection. The use of organic liquid scintillators can provide excellent detection efficiencies, flexibility in system designs, and significant cost reductions. However, the efficient light collection in long-thin geometries has always been a challenge and is the common issue when searching for an organic liquid scintillator design for these applications. A solution utilizing wavelength shifting fibers to read-out the optical signals created in transparent fluoropolymer tubes filled with liquid scintillator has been designed and characterized.

7.1. Status of Work Priorities

7.1.1. Cosmic Ray Imager

The selected OLS module design used two 2 mm diameter WLS fibers and a 5.28 mm inside diameter FEP tube filled with EJ-309. In a side-by-side comparison with a standard plastic scintillating fiber, the OLS module detected 1.17 ± 0.1 muons·min^{-1}·cm^{-2} while the plastic fiber detected 0.96 ± 0.07 muons·min^{-1}·cm^{-2}. This demonstrated that no muon events were being lost due to the absorption and re-emission efficiencies of the WLS fibers. In a full 2-meter long test, the module showed a constant detection rate along the module demonstrating event losses of less than 5% along the length of the module due to signal attenuation in the WLS fibers. The data showed a (95.4 ± 0.1)% detection rate of triggered events that increased to (98.4 ± 0.5)% when lower light yield background events were subtracted. Measurements with additional external WLS fibers demonstrate an increased signal that provides the potential

to increase the module's length with minimal increase in complexity or costs. The timing information extracted from the WLS fiber signal provided only coarse determination of the interaction location with uncertainties of ± 40 cm. This could be considerably reduced to less than 10 cm or more when using a faster PMT (H8500) and WLS (BCF-92). The potential for this measurement to resolve ambiguities in module crossing points could make a number of cost effective detector designs possible in future development. The ability to couple the WLS fibers to the outside of the fluoropolymer tube not only reduces the complexity of the system and provides more design options; it also eliminates the concern of long-term degradation of the WLS fiber while submerged in the OLS.

7.1.2. Fast Neutron Detector

Initial experiments were conducted to characterize the capability of the detection module to discriminate between neutrons and gamma rays and estimate its fast neutron detection efficiency. A light pulse from a neutron interaction in the EJ-309 has a longer tail than a light pulse from a gamma ray event due to higher proportion of delayed fluorescence. The experiments verified that the EJ-309 scintillation light escaping the sides of the FEP tube showed varied pulse timing profiles for neutron and gamma ray events. The fraction of the original light captured was not optimized and the figures of merit for charge ratio, pulse gradient analysis, and rise time pulse shape discrimination methods were 0.53, 0.40, and 0.58, respectively. The V1751 and DT5720 digitizers showed small variations in performance based on the pulse shape discrimination method used. As expected, the additional processes of absorption and re-emission in the WLS fibers alter the timing profiles of the original EJ-309 pulses. The degradation in the timing profile resulted in no pulse shape discrimination when using the charge ratio and pulse gradient analysis methods. However, the rise time method clearly demonstrated pulse shape discrimination capability with a FOM of 0.45. We expect

the performance to improve with additional WLS fiber characterization and optimization of the algorithm's parameters. Even with degraded performance, the ability to use wavelength shifting materials for pulse shape discrimination has the potential to expand the use of organic liquid scintillators for fast neutron detection. The fast neutron detection intrinsic efficiency was measured with an AmBe source and estimated to be 3.7% for a single layer of the modules and 14% for four-layers. Since a pure neutron source measurement was not taken, these values are rough estimates and require additional testing to ensure their validity. Based on these rough estimates, a one square meter panel with four-layers of modules positioned 2 meters away from the hypothetical nuclear weapon would have enough counts to identify the presence of special nuclear material in less than 15 minutes.

7.2. Future Work

Now that a viable alternative to plastic scintillating fibers has been identified, additional characterization and optimization of the detection modules are required.

- Test a full 2-meter long, three 1mm diameter WLS fiber module. In small-scale tests, this module had similar light collection efficiency as the two 2 mm diameter WLS module, but attenuation in smaller diameter fibers are generally poorer. The advantage of using 1 mm diameter over 2 mm diameter WLS fiber is an improved packing efficiency, i.e., preventing the loss of active detection area.

- Fluoropolymer tubes can be extruded in a wide range of forms, as shown in Figure 7.1, with many advantages to include improved packing efficiency, increased active area, potential for improve light collection efficiency, and simplification of the manufacturing process. For example, the ability to slide the WLS fiber into pre-made channels after the tube was filled and sealed would greatly simplify the construction of each module with the potential

to minimize intervening wall thickness. Extramural material can also be included during the extrusion process to increase light collection and prevent cross talk between the modules. The only disadvantage would be increased cost mostly associated with the initial design and construction of the extrusion mandrel die.

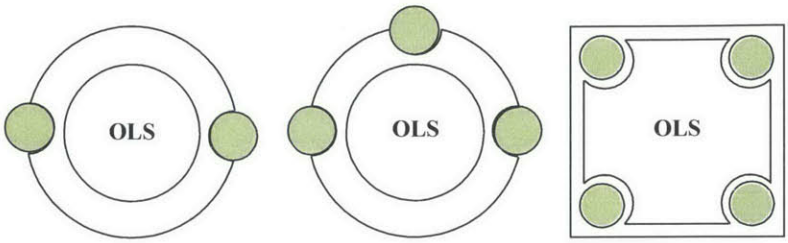

Figure 7.1. Fluoropolymer tubes can be extruded in many forms opening up many configurations to be considered (not to scale). The WLS fibers are placed in pre-made grooves or channels simplifying the manufacturing of the modules.

o Optimization of light collection at the PMT. The WLS fiber shifts the OLS blue light to longer green light. For bialkali photocathode based PMTs like the H8500 and R6095 this reduces the quantum efficiency by 5-10%. This is compensated for by increasing the number of WLS, but an analysis of alternative PMT-WLS fiber combinations may yield an improved solution.

The following characterization and optimization for the nuclear security application of the detection module are also required.

o The optimal dimensions of the OLS filled module for fast neutron detection will be different than those for the CRI system. The tradeoff of neutron detection efficiency with light collection in the WLS fiber should be analyzed.

o The effects of attenuation on the PSD capability should be characterized. Attenuation effects may further degrade the pulse information in the WLS fiber signal although a portable fast neutron detector will most likely be less than 1-meter. An optimal combination of OLS, WLS fiber, and PMT should be investigated.

Bibliography

[1] N. Tsoulfanidis and S. Landsberger, *Measurement and Detection of Radiation*, 3rd ed. Boca Raton, FL: CRC Press, 2011.

[2] D. K. Wehe, "Current Trends in Ionizing Radiation Detection," *Nuclear Engineering and Technology - Journal of the Korean Nuclear Society*, vol. 38, pp. 311-318, June 2006.

[3] E. Acosta, "Achieving Sustainable, Optimal Sagd Operations," *Journal of Petroleum Technology*, vol. 61, pp. 24-28, Nov 2010.

[4] S. Gault, "An in-Depth Look at How in Situ Oil Sands Development Has Evolved," *Alberta Oil: The Business of Energy*, 12 Feb 2014. Available: http://www.albertaoilmagazine.com/2014/02/in-situ-bitumen-recovery/

[5] K. Nagamine, M. Iwasaki, K. Shimomura, and K. Ishida, "Method of Probing Inner-Structure of Geophysical Substance with the Horizontal Cosmic-Ray Muons and Possible Application to Volcanic Eruption Prediction," *Nuclear Instruments and Methods in Physics Research Section A: Accelerators, Spectrometers, Detectors and Associated Equipment*, vol. 356, pp. 585-595, March 1995.

[6] J. Marteau, D. Gibert, N. Lesparre, F. Nicollin, P. Noli, and F. Giacoppo, "Muons Tomography Applied to Geosciences and Volcanology," *Nuclear Instruments and Methods in Physics Research Section A: Accelerators, Spectrometers, Detectors and Associated Equipment*, vol. 695, pp. 23-28, December 2012.

[7] T. Botto, A. Mazur, R. Kats, D. Mccowan, H. Murched, J. Shah, *et al.*, "Resevoir Saturation Monitoring with Cosmic Rays," presented at the World Heavy Oil Congress 2014, New Orleans, 2014.

[8] S. Fetter, V. A. Frolov, M. Miller, R. Mosley, O. F. Prilutsky, S. N. Rodonov, *et al.*, "Detecting Nuclear Warheads," *Science & Global Security*, pp. 225-302, 1990.

[9] S. Stange, D. R. Mayo, R. E. Lakis, and M. W. Johnson, "Development of a Neutron Pod Spectrometer," ed. LANL, 2011.

[10] J. Mattingly, "Polyethylene-Reflected Plutonium Metal Sphere: Subcritical Neutron and Gamma Measurements," DOE, Ed., ed. Albuquerque, NM: Sandia National Laboratories, 2009.

[11] Ortec, "Fission Meter: Portable Neutron Source Identification System," ed. Oak Ridge, TN: AMETEK, 2013.

[12] F. D. Brooks, "Development of Organic Scintillators," *Nuclear Instruments and Methods*, vol. 162, pp. 477-505, 1979.

[13] B. Viren, "Bis-Msb Emission and Absorption Spectra," ed. http://www.phy.bnl.gov/~bviren/lbne/cdr/volume-5/figures/v5ch06-bisMSBemission.pdf, 2011.

[14] G. Laustriat, "The Luminescence Decay of Organic Scintillators," *Molecular Crystals,* vol. 4, pp. 127-145, 1968.

[15] M. J. Berger, J. S. Coursey, M. A. Zucker, and J. Chang. Estar, Pstar, and Astar: Computer Programs for Calculating Stopping-Power and Range Tables for Electrons, Protons, and Helium Ions (Version 1.2.3) [Online]. Available: http://physics.nist.gov/Star

[16] D. E. Groom, N. V. Mokhov, and S. Striganov, "Muon Stopping Power and Range Tables 10 Mev-100 Tev," *Atomic Data and Nuclear Data Tables,* vol. 78, pp. 183-356, 2001.

[17] J. B. Birks, *The Theory and Practice of Scintillation Counting.* Oxford, New York: Pergamon Press, The Macmillan Company, 1964.

[18] R. L. Craun and D. L. Smith, "Analysis of Response Data for Several Organic Scintillators," *Nuclear Instruments and Methods,* vol. 80, pp. 239-244, April 1970.

[19] F. T. Kuchnir and F. J. Lynch, "Time Dependence of Scintillations and the Effect on Pulse-Shape Discrimination," *Nuclear Science, IEEE Transactions on,* vol. 15, pp. 107-113, 1968.

[20] G. F. Knoll, *Radiation Detection and Measurement / Glenn F. Knoll.* New York: John Wiley & Sons, 2000.

[21] "Ej-305 Liquid Scintillator Data Sheet," ed. Sweetwater TX: ELJEN Technologies.

[22] S. Fetter and R. Mosley, "Emission and Absorption of Radiation," *Science & Global Security,* pp. 225-302, 1990.

[23] J. M. Verbecke, C. Hagmann, and D. Wright, "Simulation of Neutron and Gamma Ray Emission from Fission and Photofission," Lawrence Livermore National Laboratory, Livermore UCRL-AR-228518, 2010.

[24] D. Reilly, N. Ensslin, H. Smith, Jr., and S. Kreiner, "Passive Nondestructive Assay of Nuclear Materials," Technical Report 0-16-032724-5, 1991.

[25] M. B. Chadwick, M. Herman, P. Obložinský, M. E. Dunn, Y. Danon, A. C. Kahler, *et al.*, "Endf/B-Vii.1 Nuclear Data for Science and Technology: Cross Sections, Covariances, Fission Product Yields and Decay Data," *Nuclear Data Sheets,* vol. 112, pp. 2887-2996, 2011.

[26] R. Katz, S. C. Sharma, and M. Homayoonfar, "Detection of Energetic Heavy Ions," *Nuclear Instruments and Methods,* vol. 100, pp. 13-32, April 1972.

[27] A. Enqvist, C. C. Lawrence, B. M. Wieger, S. A. Pozzi, and T. N. Massey, "Neutron Light Output Response and Resolution Functions in Ej-309 Liquid Scintillation Detectors," *Nuclear Instruments and Methods in Physics Research Section A: Accelerators, Spectrometers, Detectors and Associated Equipment,* vol. 715, pp. 79-86, 2013.

[28] S. F. Naeem, S. D. Clarke, and S. A. Pozzi, "Validation of Geant4 and Mcnpx-Polimi Simulations of Fast Neutron Detection with the Ej-309 Liquid Scintillator," *Nuclear*

Instruments and Methods in Physics Research Section A: Accelerators, Spectrometers, Detectors and Associated Equipment, vol. 714, pp. 98-104, 2013.

[29] M. J. Berger, J. H. Hubbell, S. M. Seltzer, J. Chang, J. S. Coursey, R. Sukumar, *et al.* Xcom: Photon Cross Sections Database [Online]. Available: http://www.nist.gov/pml/data/xcom/index.cfm

[30] M. Janecek, "Reflectivity Spectra for Commonly Used Reflectors," *Nuclear Science, IEEE Transactions on,* vol. 59, pp. 490-497, 2012.

[31] M. Janecek and W. W. Moses, "Optical Reflectance Measurements for Commonly Used Reflectors," *Nuclear Science, IEEE Transactions on,* vol. 55, pp. 2432-2437, 2008.

[32] M. Janecek and W. W. Moses, "Design of an Instrument to Measure Optical Reflectance of Scintillating Crystal Surfaces," *Nuclear Science, IEEE Transactions on,* vol. 55, pp. 1381-1386, 2008.

[33] M. Janecek and W. W. Moses, "Measuring Light Reflectance of Bgo Crystal Surfaces," *Nuclear Science, IEEE Transactions on,* vol. 55, pp. 2443-2449, 2008.

[34] M. Janecek and W. W. Moses, "Simulating Scintillator Light Collection Using Measured Optical Reflectance," *Nuclear Science, IEEE Transactions on,* vol. 57, pp. 964-970, 2010.

[35] M. Schwartz, "Principles of Electrodynamics," ed. New York: Dover, 1987.

[36] N. A. Amos, A. D. Bross, and M. C. Lundin, "Optical Attenuation Length Measurements of Scintillating Fibers," *Nuclear Instruments and Methods in Physics Research Section A: Accelerators, Spectrometers, Detectors and Associated Equipment,* vol. 297, pp. 396-403, 1990.

[37] P. Rebourgeard, F. Rondeaux, J. P. Baton, G. Besnard, H. Blumenfeld, M. Bourdinaud, *et al.*, "Fabrication and Measurements of Plastic Scintillating Fibers," *Nuclear Instruments and Methods in Physics Research Section A: Accelerators, Spectrometers, Detectors and Associated Equipment,* vol. 427, pp. 543-567, 1999.

[38] "Scintillation Products-Scintillating Optical Fibers," ed. Hiram, OH: Saint-Gobain Chrystals, 2011.

[39] H. Blumenfeld, E. Gaillard, and P. Rebourgeard, "Measurement of the Reflection Coefficient at the Core-Cladding Interface in Plastic Scintillating Fibers," *Nuclear Instruments and Methods in Physics Research Section A: Accelerators, Spectrometers, Detectors and Associated Equipment,* vol. 309, pp. 169-178, 1991.

[40] R. Stroynowski, "Light Propagation and Timing with Scintillating Fibers," *Nuclear Physics B - Proceedings Supplements,* vol. 23, pp. 273-279, 1991.

[41] G. Feldman, M. Messier, J. Cooper, R. Ray, and N. Grossman. (2007, 8 October 2013). Numi Off-Axis Ne Appearance Experiment Technical Design Report. Available: http://www-nova.fnal.gov/nova_cd2_review/tdr_oct_23/tdr.htm

[42] L. Benussi, N. Bruski, N. D'ambrosio, Y. Déclais, J. Dupraz, J. P. Fabre, *et al.*, "Large Liquid-Scintillator Trackers for Neutrino Experiments," *Nuclear Instruments and Methods in Physics Research Section A: Accelerators, Spectrometers, Detectors and Associated Equipment,* vol. 488, p. 503, 2002.

[43] Hamamatsu. (1996, June 2013). Photomultiplier Tubes R6094, R6095. [Online]. Available: http://www.sphere.bc.ca/test/phototubes2/ham/r6095.pdf

[44] Hamamatsu. (2011, June 2013). Flat Panel Type Multianode Pmt Assembly H8500 Series. [Online]. Available: http://www.hamamatsu.com/resources/pdf/etd/H8500_H10966_TPMH1327E02.pdf

[45] Caen, "Technical Information Manual Model V1751 Digitizer," Italy2013.

[46] T. J. Parker, personal communication, 19 July 2013

[47] Zeus. (2005, July 2013). Optical Clarity of Fluoropolymers. [Online]. Available: http://www.zeusinc.com/UserFiles/zeusinc/Documents/Zeus_Optical_Clarity.pdf

[48] M. M. Bourne, S. D. Clarke, E. C. Miller, M. Flaska, and S. A. Pozzi, "Measurement of Detector Resolution for Neutral Particle Detection with Liquid Scintillators," in *Nuclear Science Symposium Conference Record (NSS/MIC), 2010 IEEE*, 2010, pp. 981-985.

[49] A. Enqvist, K. J. Weinfurther, M. Flaska, and S. A. Pozzi, "Characterization of a Mixed Multiplicity Counter Based on Liquid Organic Scintillators," *Nuclear Science, IEEE Transactions on,* vol. 58, pp. 2413-2420, 2011.

[50] S. A. Pozzi, M. M. Bourne, and S. D. Clarke, "Pulse Shape Discrimination in the Plastic Scintillator Ej-299-33," *Nuclear Instruments and Methods in Physics Research Section A: Accelerators, Spectrometers, Detectors and Associated Equipment,* vol. 723, pp. 19-23, 2013.

[51] P. J. Sellin, G. Jaffar, and S. D. Jastaniah, "Performance of Digital Algorithms for N/Gamma Pulse Shape Discrimination Using a Liquid Scintillation Detector," presented at the Nuclear Science Symposium Conference Record, 2003 IEEE, 2004.

[52] B. D'mellow, M. D. Aspinall, R. O. Mackin, M. J. Joyce, and A. J. Peyton, "Digital Discrimination of Neutrons and -Rays in Liquid Scintillators Using Pulse Gradient Analysis," *Nuclear Instruments and Methods in Physics Research Section A: Accelerators, Spectrometers, Detectors and Associated Equipment,* vol. 578, pp. 191-197, 2007.

[53] S. D. Jastaniah and P. J. Sellin, "Digital Pulse Shape Algorithms for Scintillation-Based Neutron Detectors," in *Nuclear Science Symposium Conference Record, 2001 IEEE*, 2001, pp. 816-821 vol.2.

[54] G. Ranucci, "An Analytical Approach to the Evaluation of the Pulse Shape Discrimination Properties of Scintillators," *Nuclear Instruments and Methods in Physics Research Section A: Accelerators, Spectrometers, Detectors and Associated Equipment,* vol. 354, pp. 389-399, 1995.

[55] G. Ranucci, "A Review of the Statistical Foundations of the Classical Pulse Shape Discrimination Techniques in Scintillation Applications," in *Nuclear Science Symposium Conference Record, 2004 IEEE*, 2004, pp. 804-809 Vol. 2.

[56] C. Xiaohui, L. Rong, L. Xinxin, and Z. Tonghua, "Analysis of Three Digital N/Γ Discrimination Algorithms for Liquid Scintillation Neutron Spectrometry," *Radiation Measurements,* vol. 49, pp. 13-18, 2013.